Early Stages of Massive Star Formation

Vlas Sokolov

München 2018

Early Stages of Massive Star Formation

Vlas Sokolov

Dissertation
an der Fakultät fur Physik
der Ludwig–Maximilians–Universität
München

vorgelegt von
Vlas Sokolov
aus Kyjiw, Ukraine

München, den 13 Juli 2018

Erstgutachter: Prof. Dr. Paola Caselli
Zweitgutachter: Prof. Dr. Markus Kissler-Patig
Tag der mündlichen Prüfung: 27 August 2018

Contents

List of Figures

List of Tables

Zusammenfassung

Ein langwährendes Problem der Astrophysik stellt das Verständnis dar, wie Sterne von hoher Masse entstehen. Viele theoretische Modelle und numerische Simulationen, welche versuchen dieses Problem zu behandeln, sind oftmals höchst abhängig von den physikalischen Anfangsbedingungen des Gases, aus welchem massive Sterne geboren werden. Beobachtungen der frühesten Phasen der Entstehung massereicher Sterne sind allerdings oft von großen Volumina verdeckenden Staubes begrenzt und verlangen hoch winkelauflösende Radio- und Submillimeterbeobachtungen. Infrarot dunkle Wolken (eng. "infrared dark clouds"; IRDCs) wurden als die am erfolgversprechendsten Kandidaten für Vorläufer massereicher Sterne und Sternhaufen festgelegt. In dieser Arbeit wird eine Analyse der Beobachtungen der IRDC G035.35–00.33, welche zuvor als ein exzellentes Ziel zum Erforschen der Anfangsbedingungen der Entstehung massereicher Sterne gefunden wurde, im großen sowie kleinen Maßstab präsentiert.

Um auf Parsecskalen das ausgedehnte Wolkenmaterial zu verfolgen, wird die IRDC mit der interstellaren Ammoniakemission, kartiert mit dem Green Bank Teleskop (GBT), untersucht und unter Verwendung der archivierten fern-infrarot Daten werden Temperaturen der IRDC unabhängig von beiden Datensätzen abgeleitet. Durch einen quantitativen Vergleich der beiden Methoden zur Einschätzung der Temperatur stellt sich heraus, dass die konventionelle Methode zur Ableitung der Staubtemperatur systematisch die IRDC Temperatur um $2-3$ K überschätzt. Der Fehler der Temperaturkarte erhalten durch die Staubemission, um für die Emissionsmischung der Sichtlinie beizusteuern, wurde als Ursache der Bias aufgezeigt. Die GBT Beobachtungen offenbaren außerdem einen großräumigen linearen Geschwindigkeitsgradienten der Größe von $\approx$0.2 km s^{-1} pc^{-1} entlang der $\approx$6 parsec Kante der IRDC. Sowohl die Temperatur des Staubs als auch die kinematische Struktur stellen sich als konsistent mit denen der sternenlosen dunklen Filamenten heraus, allerdings erweckt die kinetische Gastemperatur auf kleineren Skalen den Eindruck, dass der kollektive Heizmechanismus mit der Position massiver protostellarer Kerne übereinstimmt.

Auf kleineren Skalen wird die IRDC Struktur durch die kombinierte Beobachtung des GBT und des Very Large Array (VLA) verfolgt, welche die Kinematik des dichten Gases und die Temperatur bis zu einer Skala von 0.07 pc auflöst. Obwohl man annimmt, dass Regionen mit Entstehung massereicher Sterne typischerweise von supersonischen Bewegungen dominiert werden, zeigen in IRDC G035.39 über ein Drittel der gefitteten Ammoniak-Spektren subsonische, nichtthermische Bewegungen mit einem Höchstwert der sonischen Mach-Zahlen im subsonischen Bereich der globalen Verteilung.

Die Ergebnisse suggerieren auch, dass die gröbere spektrale Auflösung, die in den anderen

VLA Studien benutzt wurde, die Detektion subsonischer Turbulenzen in anderen IRDCs gehemmt haben könnte. Diese Entdeckung verlangt nach einer Reevaluation der Rolle turbulenter Dissipation und subsonischer Regionen in der Entstehung von massiven Sternen und Haufen, welche durch ein Stadium ähnlicher, als zuerst angenommen, der der Entstehung massearmer Sterne laufen könnte. Zusätzlich zur Entdeckung der Bereiche subsonischer Turbulenzen werden andere ähnlichkeiten zu Wolken, in denen massearme Sterne entstehen, gefunden. Unter Benutzung des agglomerativen hierarchischen Clusterings entwirren wir die komplexe Kinematik der IRDC und identifizieren in ihr sieben große geschwindigkeitskohärente Regionen. Die typische Geschwindigkeitsgradientengröße, die man in diesen Gebieten findet, ist generell konsistent mit den Werten, die man entlang nahe gelegenen massearmen dichten Wolkenkernen findet. Wenn die beobachteten geordneten Geschwindigkeitsgradienten die Festkörperrotation der Kernhülle repräsentieren, schätzen wir darüber hinaus, dass der spezifische Drehimpuls etwa 2×10^{21} cm^2 s^{-1} ist, ähnlich dem von Kernen in denen massearme Sterne entstehen.

Nichtsdestotrotz gibt es noch viel über die infrarot dunklen Wolken und ihre Beziehung zur Entstehung von massereichen Sternen und Haufen zu lernen. Gegenwärtige und zukünftige Einrichtungen werden zusammen mit modernen Methoden der Computerdatenanalyse dabei helfen, eine bessere Einsicht in die frühen Phasen der Entstehung massiver Sterne zu ermöglichen.

Summary

A long-standing problem of astrophysics is understanding how high-mass stars form. Theoretical models and numerical simulations aiming to address this problem are often highly dependent on the initial physical conditions of the gas out of which massive stars are born. However, the observations of the earliest stages of high-mass star formation are often limited by large volumes of obscuring dust and require high-angular resolution radio and submillimeter observations. Infrared dark clouds (IRDCs) have been established as the most promising candidates for being the progenitors of massive stars and star clusters. In this thesis, an analysis of observations towards IRDC G035.39–00.33, previously found to be an excellent target to probe the initial conditions for high-mass star formation is presented both on large and small scales.

On parsec-scales tracing the extended cloud material, the IRDC is investigated with the interstellar ammonia emission mapped with the Green Bank Telescope (GBT) and using the archival far-infrared data, temperatures of the IRDC are independently derived from both datasets. From a quantitative comparison between the two temperature estimating methods, the conventional method of deriving dust temperature is found to systematically overestimate the IRDC temperatures by $2-3$ K. The failure of the dust emission-derived temperature map to account for the line of sight emission mixing is shown to be the cause for the bias. In addition, the GBT observations reveal a large-scale linear velocity gradient of $\sim$0.2 km s^{-1} pc^{-1} magnitude along the $\sim$6 parsec ridge of the IRDC. Both the dust temperature and the kinematics structure are found to be consistent with that of the starless dark filaments, however, the kinetic gas temperature on smaller scales is suggestive of the collective heating mechanism coincident with the positions of massive protostellar cores.

On smaller scales, the IRDC structure is traced by the combined observations of GBT and the Very Large Array (VLA), resolving the dense gas kinematics and temperature down to scales of 0.07 pc. Despite high-mass star forming regions typically thought to be dominated by supersonic motions, in IRDC G035.39 over a third of the fitted ammonia spectra show subsonic non-thermal motions, with the overall distribution of sonic Mach numbers peaking in the subsonic regime. These results also suggest that the coarser spectral resolution used in the other VLA surveys of IRDCs could have inhibited the detection of subsonic turbulence in other IRDCs. This finding calls for a reevaluation of the role of turbulent dissipation and subsonic regions in massive-star and cluster formation, which may proceed through a stage more similar to the low-mass star formation than previously thought. In addition to the finding of the subsonic turbulence regime, other similarities to low-mass star forming clouds are found. Through the use of agglomerative hierarchical clustering, we disentangle the complex kinematics of the IRDC and identify seven

large velocity-coherent regions in it. The typical magnitude of the velocity gradients in these regions is generally consistent with the values found towards nearby low-mass dense cloud cores. Furthermore, if the observed ordered velocity gradients represent the core envelope solid-body rotation, we estimate the specific angular momentum to be about 2×10^{21} cm^2 s^{-1}, similar to the low-mass star-forming cores.

Nonetheless, there is still much to be learned about infrared dark clouds and their relation to high-mass and cluster formation. Recent and future facilities, together with modern computational data analysis methods, will help to provide further insight into the early stages of massive star formation.

Chapter 1

Introduction

> *"Anyone wishing to study the problem [of how gas forms stars] is aided immeasurably by the fact that star formation is also occurring now, and in regions close enough that the transformation can be examined in some detail."*
>
> - The Formation of Stars, *Stahler & Palla (2005)*

1.1 Overview

Electromagnetic radiation, in the form of visible light, opens our largest sensory window into our surroundings, and the vast majority of it originates from the stars. It also has consistently been (at least until the recent advances in multi-messenger astronomy) the sole medium for shedding light on the physical nature behind astronomical phenomena. Among these phenomena is that of the star formation.

This thesis aims to provide a useful insight into how stars come to be. In particular, it investigates the physical properties of the interstellar gas from which massive stars[1] and clusters of stars are born. The insight into the star formation process is of observational nature, and is gained by analysing the data obtained through far-infrared and radio facilities and comparing it with state-of-the-art predictions from theoretical models and numerical calculations. The process of massive star formation is relatively short on astronomical timescales, and the birth of high-mass stars disrupts the material they were born in. Because of this, observations of initial conditions of the process must focus on the densest and coldest regions of our Galaxy.

Because star formation was a topic of active research over many decades, this thesis opens with a broad introduction to the subject, which constitutes this chapter. First, an overview of the matter in our Galaxy is given, narrowing down to the molecular clouds that have the capacity to form stars (§1.2). Then, a description of the classical picture of star formation is provided in §1.3. Having established the common processes occurring as stars form, the phenomenon of high-mass star formation is described in §1.4, first from the observational point of view (§1.4.1)

[1] throughout this work, massive and high-mass stars refer to stars with eight or more masses of the Sun.

and then from the theoretical one (§1.4.2). Finally, the need for investigating the initial conditions for massive star formation is postulated in §1.4.3 and the observational target of this thesis is described in it. In addition, the common methods used in the following chapters, such as observational techniques and spectral emission models, are described in some depth in §1.5.

1.2 The Interstellar Medium

The formation of stars can be described as a process of hierarchical fragmentation and mass assembly of diffuse gas, and it spans over ten orders of magnitude in both mass and linear scales (Shu et al. 1987). While a more detailed close-up of the process will be presented in the later sections that deal with smaller spatial scales, a global picture of star formation is perhaps better suited to serve as an overview of the topic. As star formation occurs almost exclusively within galaxies, this section will present a summary of star formation on scales up to a few kiloparsecs[2] and down to the size of individual molecular clouds. In addition, the recent breakthroughs in instrumental astronomy used as illustrative aid, supporting the narrative where possible, enabling stunning glimpses at this larger picture by illustrating the large scale view of star formation with recent insights from modern all-sky surveys.

We view our host Galaxy, the Milky Way, edge-on. Located about 8.5 kpc from its centre, the Solar System lies close to the midplane of the Galactic disk (a flat structure about 15 kpc in radius), and rotates around it at a speed of 220 km s^{-1}. The vertical density structure of the disk, much like the Earth's atmosphere, has no clear boundaries, and is found to decrease gradually away from the midplane. One of the defining characteristics of the Galactic disk is its thinness: the height where the density approaches half of that at the midplane is only about 300 pc. Most of the Milky Way visible matter (not accounting for the collisionless dark matter) is contained within stars, yet the empty space spanning between the stars in Milky Way is not pure void, but is filled with diffuse matter called the interstellar medium (ISM). The material in the ISM accounts for the remaining mass budget of the Galaxy, constituting about 10% of the total Galactic baryonic mass. ISM serves as the sole raw material for all the star formation in galaxies, and understanding it is of paramount importance for large-scale view of star formation. The ISM is a dynamic environment, and it can be consumed by star formation, ejected outside its host galaxies, or replenished by accretion from the intergalactic medium, a diffuse medium between galaxies. Moreover, the confinement of matter inside the stars is not eternal, and the ISM can be replenished by stellar winds, and the ejecta from unstable stars and supernovae explosions.

The ISM is mainly composed of a mixture of gas and dust. The gas constituent of the ISM is mainly hydrogen manifested in several forms. The dust refers to interstellar particles composed of silicate and carbon compounds of $0.005 - 1$ μm size (Mathis et al. 1977). Although the dust grains are relatively few with respect to gas (about 1% of the particle number, Hildebrand 1983), they will be shown to be dynamically important cooling agents and important catalysts in chemical reactions. Depending on its density and temperature, the ISM has been found to consist of different phases, spanning approximately six orders of magnitude in temperature: from hot and

[2] 1 pc = 3.086×10^{18} cm

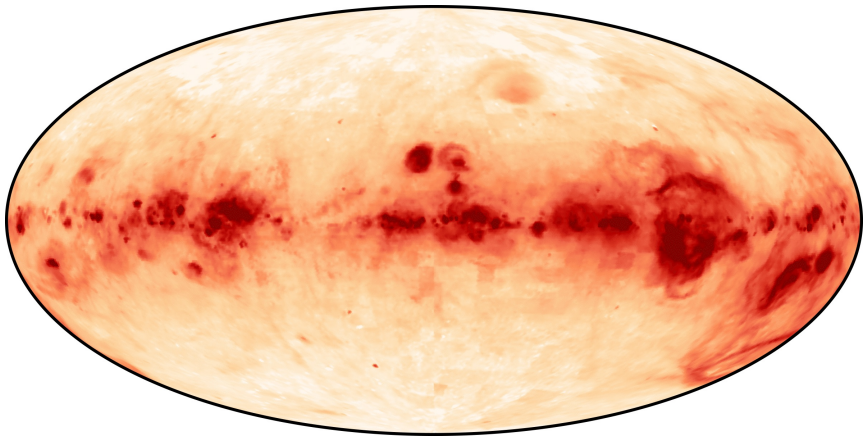

Figure 1.1 A map of ionized hydrogen gas in the Milky Way, taken with the Wisconsin Hα Mapper (Haffner et al. 2003). *Credit: WHAM collaboration, University of Wisconsin-Madison, Space Science Institute & National Science Foundation.*

diffuse gas at $> 10^6$ K down to cold H_2 clumps of about 10 K. These phases are often distinguished, in addition to temperature and density regimes, by the ionization state of the hydrogen gas, which could be found either as fully ionized plasma (H II gas), as neutral atomic state (H I phase), or in molecular form as H_2 gas. These different phases, much like the ISM itself, are not static, and can be locally converted amongst themselves under favorable energy balance considerations. For instance, the hot gas can cool down through adiabatic expansion or by radiating excess energy away, converting to a denser phase; cold molecular gas, in turn, can be dissociated through ionizing radiation emitted by young OB stars. In the following sections, different phases of the ISM are outlined to serve as an overview of density and temperature regimes the gas can reside in, and the star forming potential of the ISM will be discussed.

The *average* density of the material in the ISM, only about one particle per cubic centimeter (Boulares & Cox 1990), is not sufficient for this interstellar gas to become gravitationally bound and form stars. Moreover, densities this low are unlikely to assemble in denser condensations due to the shear forces originating from Galactic disk rotation (e.g., Elmegreen 2012). In fact, gravity is only one of the forces that dominates the ISM dynamics, along with turbulence injections from stellar winds and supernovae (SNe) explosions, density wave perturbations, star-forming feedback, Galactic shear, and radiation pressure from stellar populations. So how, and where does the relatively diffuse gas become dense and cold enough to collapse further, eventually forming stars? Moreover, just what are the conditions that are required for the physics governing star formation to take over?

The largest volume fraction of the interstellar medium is occupied by hot plasma ($T \sim 10^5 - 10^6$ K, number density $n \sim 10^{-4} - 10^{-3}$ cm^{-3}), manifested as an extended coronal gas, not only filling the void between colder ISM phases within the Galactic disc but also surrounding the Galaxy in a form of a halo. The coronal gas has a cooling timescale of about one million years, and its energetic state is sustained mainly by the energetic shock waves driven by supernova explosions from the Galactic disk (McKee & Ostriker 1977). Embedded in this hot diffuse

medium and filling most of the remaining volume of the Milky Way disk is the warm ionized phase of the ISM, consisting mainly of ionized hydrogen gas (denoted as H II gas) heated to $T \sim 10^3 - 10^4$ K by the interstellar radiation field. The warm ionized phase is thought to coincide with the Galactic disk and hovers above the disk at scale heights of about 300 pc, supported mostly by turbulence. While its typical densities ($n \sim 0.4$ cm^{-3}) are still far below densities of star-forming regions, young OB-stars and associations are known to produce denser H II regions, signposts of light from young massive stars piercing through their natal molecular clouds. Figure 1.1 shows a distribution of ionized hydrogen gas in the Milky Way, as measured by the Wisconsin Hα Mapper (Haffner et al. 2003).

The remaining unfilled volume of the Galaxy is filled with largely neutral medium, consisting mostly of atomic (H I) and molecular (H_2) hydrogen gas. The atomic hydrogen gas (making up about 60% of the gas mass in the Galaxy) has been shown to trace the disk and the spiral arms of the Milky Way, and its measurements were, in fact, the first direct observational evidence of the Milky Way being a spiral galaxy. While it was proposed that the Galaxy was of spiral type since as early as mid-nineteenth century (Alexander 1852), the conclusive evidence could not be obtained due to optical light efficiently scattered by small interstellar particles (commonly referred to as dust grains), obscuring line of sight observations towards the Galactic plane. Therefore, while indirect arguments — namely, the flatness of the Galactic disk and content of OB stars typical for spiral galaxies — supported the spiral nature of the Galaxy, the first direct evidence for it came from the measurements of 21-cm line of neutral hydrogen (Oort et al. 1958), showing that the distribution of the neutral hydrogen in the Galaxy follows a spiral pattern. The 21-cm line results from an electron spin flip of the neutral hydrogen atom, and under normal conditions is considered "forbidden" due to its very low spontaneous decay rate. While in higher-density gas de-excitation via emission of radiation is not likely (excited states are mainly de-populated via collisions), in diffuse interstellar medium the 21-cm line is one of the strongest spectral lines emitted by the ISM. The follow-up studies of the neutral atomic hydrogen have led to the idea that the H I gas is comprised of two components, where dense cool gas clouds are surrounded by a hot intercloud medium (Spitzer 1968). Subsequently, the balancing of cooling and heating processes in the ISM was shown to separate the H I gas into two distinct phases: warm ($T = 10^3 \sim 10^4$ K) and cold ($T = 50 \sim 100$ K) neutral media (Field et al. 1969). Together with the hot plasma phase described earlier, the three phases constitute the standard three-component model of diffuse ISM (originally put forward (along with the hot ionized phase itself) by McKee & Ostriker 1977).

The phases outlined above, however, are far too diffuse and hot to directly condense into star-forming material, and in order to identify the gas directly responsible for star formation (in other words, the gas phase where star formation can readily occur), one should look at the gas holding the star-forming capacity on smaller scales. Historically, this has been done through observations of galaxies other than ours. Star formation is intimately tied to the presence of dense gas, and the power-law relation between the two has been first established by Schmidt (1959). In the follow-up studies this relation, known as the Kennicutt-Schmidt Law, has established a power-law correlation (with an index of 1.5) between the star formation rate (SFR, usually extrapolated from the UV flux emitted by young OB stars) and the total gas content (H I and H_2) in the galaxies (Kennicutt 1989, 1998). More recent studies, however, have shown that this correlation is stronger when only the surface density of the H_2 gas (traced by the rotational emission of the

CO molecule) is considered, indicating that in nearby galaxies, star formation occurs exclusively[3] in the *molecular* phase of the interstellar medium. This has been shown from spatially resolved observations of galaxies, demonstrating very close correlation between the surface density of star formation and the spatially resolved molecular gas content (e.g., Kennicutt et al. 2007; Leroy et al. 2008; Bigiel et al. 2008). Having shown that the molecular gas is the raw material for star formation, the next question to ask is how does its distribution in the Milky Way affect the stellar outcome of the process?

1.2.1 Molecular Clouds

Molecular clouds are the densest, coldest regions within the ISM. At densities below 100 cm^{-3}, the atomic gas undergoes a sharp transition to a molecular H_2 stage, with the exact density threshold depending on the strength of the interstellar UV radiation field (governing the dissociation of H_2) and the metallicity (controlling the efficiency of the H I to H_2 conversion process). The conversion occurs over photodissociation regions (PDRs), marking the transition between atomic gas phase, where the H_2 gas is photodissociated/ionized by UV-radiation, and the molecular phase, where the gas becomes dense enough (self-shielded), absorbing most of the dissociative radiation (e.g., Draine 2011). In the absence of UV-photons destroying molecular hydrogen, H_2 molecules become abundant, forming on the surfaces of the dust grains (van Dishoeck & Black 1986). Observationally, molecular clouds were originally identified as regions devoid of stars in the photographs of the sky (Barnard 1919), suggestive of opaque masses blocking the view of the background stars. These masses, called *dark clouds*, are regions of ISM where the interstellar dust grains absorb most of the light from the background stars, re-radiating the absorbed energy in infrared as black-body emission. Contemporary astrophysics commonly uses quantitative obscuration of background stars (extinction[4]) as a proxy for the cumulative molecular cloud density along the line of sight (column density). The molecular clouds possess a broad spectrum of masses, ranging from about a hundred Solar masses (denoting a Solar mass as $M_\odot = 1.0988 \times 10^{33}$ g henceforth) to as much as 10^7 $M_\odot$ contained in massive clouds towards the center of the Milky Way.

Although smaller molecular clouds are also capable of producing stars, most of the molecular cloud mass resides in the giant molecular clouds (GMCs, reviewed in, e.g., Dobbs et al. 2014), and most stars are born in them. Originally discovered in large-scale mapping of the CO emission of the Milky Way as large-scale (up to hundreds of parsec) continuous dense molecular regions in position-position-velocity space (e.g., Dame et al. 1987; Solomon et al. 1987), the GMCs are

[3] An explicit assumption is made here — the formation of stars is only possible from the molecular gas. It is worth noting that some theoretical studies (e.g., Glover & Clark 2012) show that molecular gas is not always a necessary condition for star formation, in agreement with the calculations of Krumholz (2012), who shows that this pathway to star formation could be significant for low-metallicity galaxies. Although the formation of stars from gas that has not achieved a large molecular fraction is possible, this formation pathway is not expected to come into play in nearby galaxies (including our own). This is largely due to the fact that the aforementioned low-metallicity condition is not applicable, with molecular hydrogen forming readily in the presence of dust grains inside self-shielded clouds.

[4] Conventionally measured in magnitudes, where each five steps in magnitude define a brightness difference of a factor of hundred.

responsible for most of the star formation in our Galaxy, and are the star-forming engines of the galaxies in general. They are characterised by large masses ($M > 10^4\ M_\odot$, Williams et al. 2000), and wide range of sizes ranging from dozens to hundreds of parsecs. Similarly to the relation found in the other galaxies, the star formation rate in molecular clouds was found to be linearly proportional to the cloud mass (Lada et al. 2010). This, of course, can be seen as a consequence of the star formation being a direct result of the gravitational collapse — higher density regions have more potential to collapse onto higher-mass stars. With the total mass of the molecular gas in the Milky Way being a few times $10^9\ M_\odot$, the star formation rate corresponding to the global gravitational collapse is $\dot{M}_{\rm ff} = M_{\rm gas}/\tau_{\rm ff}$, where $\tau_{\rm ff} \equiv (3\pi/32G\rho)^{1/2}$ is the free-fall time, the characteristic time for a spherically symmetric mass distribution with density ρ to collapse towards its center. For the densities typical of the molecular gas phase, the corresponding Galactic star formation rate would be $\dot{M}_{\rm ff} \approx 200\ M_\odot\ {\rm yr}^{-1}$ (Draine 2011). However, this comes in sharp conflict with the observed rate of star formation in the Galaxy, which is two orders of magnitude smaller (Robitaille & Whitney 2010). The explanation for the discrepancy is twofold. Firstly, most of the molecular mass in the Galaxy is not collapsing, and is held against the gravitational collapse by means of support such as thermal pressure, turbulence, rotation, and magnetic fields. Secondly, the aforementioned means of support cause the contracting material to collapse slower and in a more fragmented fashion, causing the star formation to convert gas into stars in a less efficient manner. The star-forming capacity of molecular clouds is often expressed through star formation efficiency (SFE), defined as the fraction of the cloud's total mass (gas and stars) transformed into stellar mass. Observations of entire GMCs yield SFEs that are relatively low — for example, Evans et al. (2009) find SFE over five GMCs to be in the $0.03 - 0.06$ range. However, GMCs are harboring complex internal density structure, with higher-density clumps and filaments embedded in the parent cloud (e.g., André et al. 2014). This higher-density gas is more capable of producing stars: in the same study as above, Evans et al. (2009) find that the SFE reaches as high as 0.5 when only the gas above densities of $10^5\ {\rm cm}^{-3}$ is considered. In Chapters 2 – 4, a densest region within a highly filamentary GMC is discussed in remarkable detail. To form stars, these GMC overdensities must convert part of their gravitational energy into heat during the contraction process, and the excess energy must be radiated away. In this context, gravitational stability of the GMCs has to be discussed.

While originally thought to be stabilized against the gravitational collapse, the origin of GMC stability is currently a matter of an ongoing debate: originally, the GMC stability was thought to stem from magnetic field support, but later observations of magnetic fields in them were hard to reconcile with (Dobbs et al. 2014). Supersonic turbulent motions have since been viewed as the primary means of GMC support against the gravitational collapse. This, however, presented a problem of its own, because turbulent motions in viscous fluids are known to decay through self-similar turbulent cascade, dissipating as heat at small scales. The physics of the turbulent structure is known as the Kolmogorov cascade (Kolmogorov 1941), and the dissipation timescales for supersonic turbulence are too short (Mac Low et al. 1998) compared to the typical lifetime of the molecular clouds (Blitz & Shu 1980). In their review of GMCs, McKee & Ostriker (2007) describe two possible solutions for driving (i.e., replenishing) the turbulence in GMCs. In one framework, the GMCs are transient objects arising from the colliding atomic flows. In this picture, the giant molecular clouds are not gravitationally bound and the turbulence is driven by

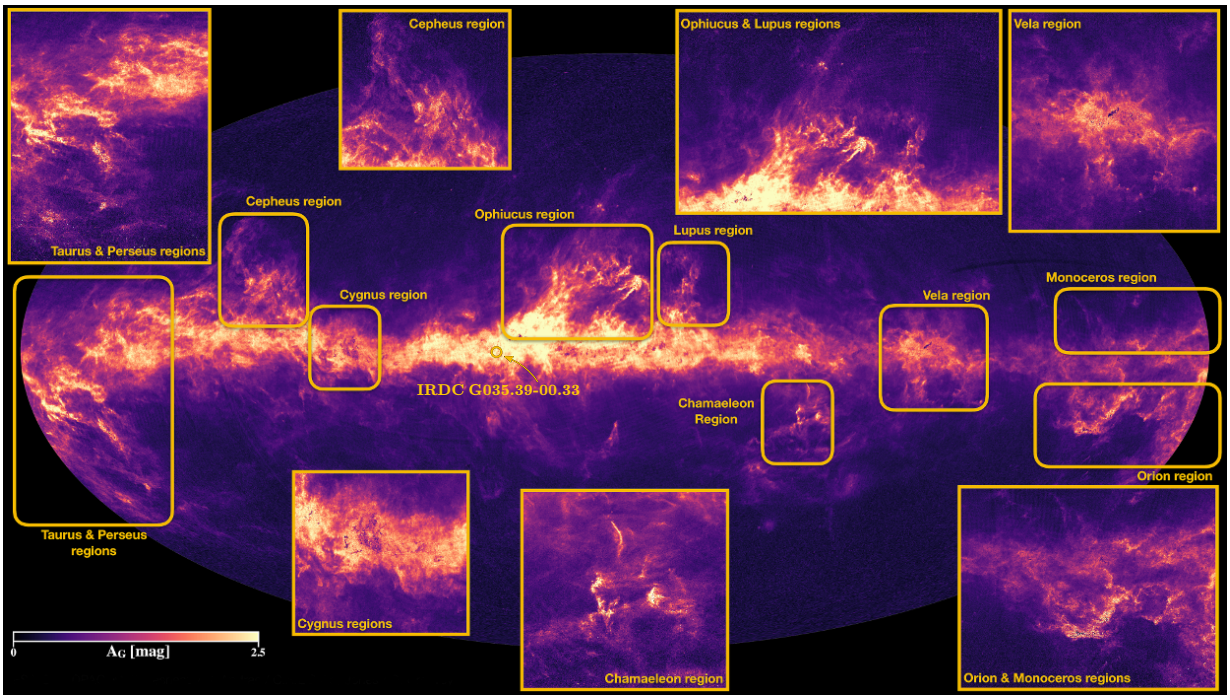

Figure 1.2 Interstellar extinction from the Gaia mission (Andrae et al. 2018). Prominent nearby molecular cloud complexes and GMCs are highlighted in yellow box overlays. While the low-mass star-forming regions like Taurus and Ophiuchus appear large because they are located relatively nearby (125 − 165 pc, Ortiz-León et al. 2017; Galli et al. 2018), the closest GMC and the site of massive star formation is the Orion Molecular Complex (414 ± 7 pc, Menten et al. 2007). Three other massive star-forming regions, the GMCs at Cygnus, Vela, and Monoceros, are also labeled on the figure. The position of the object of interest of subsequent chapters, IRDC G035.39–00.33, has been added to the original figure (the object itself is too small to be seen on the figure). *Credits: ESA/Gaia/DPAC, M. Fouesneau / R. Andrae / C.A.L Bailer-Jones of the Max Planck Institute for Astronomy (Heidelberg, Germany), O. Creevey of the Observatoire de la Cte d'Azur (Nice, France) and the entire CU8 team.*

the atomic flows that form the GMCs. In the other picture, the GMCs are gravitationally bound clouds that are responsible for driving their own turbulence through collapsing motions. In this framework, the typical lifetime of the GMCs is about a few 10^7 years, after which the clouds are dispersed by internal stellar feedback from the OB stars. Despite the overall stability of the GMCs being a matter of debate, it is the dense substructure in the clouds on *smaller* scales that yields star formation, and it is examined for the remainder of the section.

The distribution of the GMCs in the spiral galaxies, including the Milky Way, has been found to be a good tracer of galactic spiral arms (e.g., Dobbs et al. 2014). While most of the GMCs population is located kiloparsecs away from the Sun, the smaller star-forming molecular cloud complexes closest to the Solar system can be examined in closer detail. These nearby cloud complexes have been the observational testbeds for star formation theories, and have been

exhaustively studied over decades with a plethora of ground- and space-based instruments across the electromagnetic spectrum. Figure 1.2 shows the visual extinction map of the sky, constructed from individual extinction measurements of over a billion stars in Milky Way. The extinction magnitude is a measure of the number of obscuring dust grain towards each direction on the plane of sky, and can be seen as a tracer of the overall gas density. Highlighted on the extinction map, nearby molecular cloud complexes (appearing large due to their proximity) as well as the closest prominent GMC complexes are shown. The proximity of these cloud complexes allowed their internal structure to be studied from the sizes of the whole clouds down to the scales of individual star formation. In the nearby low-mass star-forming regions highlighted on Fig. 1.2 like the Taurus Molecular cloud (its mass, 10^4 $M_\odot$, not enough to be considered a GMC Pineda et al. 2010b) or Ophiuchus (harboring a population of young stars as well as embedded protostars) star formation occurs mostly within numerous dense ($\sim 10^4$ cm^{-3}) filaments (André et al. 2010; Molinari et al. 2010) harboring compact (~0.1 pc) cores (e.g., Benson & Myers 1989; Goodman et al. 1993; Caselli et al. 2002a). As a consequence of star formation found exclusively within dense H_2 regions, a minimum density threshold enabling star formation in the molecular clouds was suggested (e.g., a minimum column density corresponding to extinctions of $A_V \approx 2$ mag was suggested in Palla & Stahler 2002)[5], and the SFR in the nearby clouds was shown to be proportional to the mass of dense gas above a density threshold (Lada et al. 2012; Evans et al. 2014), although the exact threshold value is not yet clear and is affected by the environment (cf. Longmore et al. 2013, for clouds in the presence of strong radiation field). Consequently, the formation of more massive stars occurs in denser, more massive clouds, the closest of which, harboring a young OB-cluster, is in the Orion region. As massive star feedback disrupts parent molecular clouds, observing the earliest stages of the high-mass star formation thus requires finding the regions of gas denser than that in the low-mass star-forming regions above, appearing as highly extincted regions of space.

But why must the gas be cold and dense in order to form stars in the first place? As discussed earlier, from an observational perspective astronomers see that all the young stars and their predecessors (protostars) originate from within molecular clouds. However, a more fundamental answer to this question stems from the physics governing the star formation, in particular from the stability considerations of self-gravitating condensations in the molecular gas. Consider a simplistic picture where a spherical gaseous cloud composed of molecular hydrogen gas with uniform number density n_{H_2} is supported by internal thermal pressure, resulting from a uniform temperature T. In this picture, the gradual build-up of the material reaches the tipping point called the hydrostatic equilibrium, beyond which the cloud exceeds its critical mass and begins a runaway contraction. The conditions we are looking for arise from these physical considerations. Called the *Jeans mass*, this critical mass can be shown to be a function of gas temperature and density (taking its numerical form from Stahler & Palla 2005):

$$M_J = 1.0\ M_\odot \left(\frac{T}{10\ \mathrm{K}}\right)^{3/2} \left(\frac{n_{H_2}}{10^4\ \mathrm{cm}^{-3}}\right)^{-1/2}, \tag{1.1}$$

[5]The conversion between the extinctions derived for the G-band of the Gaia mission (A_G, shown on Fig. 1.2; Andrae et al. 2018), and the commonly used V-band extinction A_V is not exactly one-to-one, but they are comparable and positively correlated. See Jordi et al. (2010); Andrae et al. (2018) for a detailed comparison between the two.

where the mass exceeding M_J would overcome the thermal support and begin to collapse. Clearly, the collapse conditions are favored for gas condensations of low temperature and high density. The corresponding *Jeans length*, the critical radius of thermally supported cloud on the verge of gravitational collapse, is

$$R_J = 0.19 \text{ pc} \left(\frac{T}{10 \text{ K}}\right)^{1/2} \left(\frac{n_{\text{H}_2}}{10^4 \text{ cm}^{-3}}\right)^{-1/2}, \tag{1.2}$$

which, together with the numerical form for the Jeans mass, implies that the star-forming cores are dense and compact cold gas condensations, much smaller than the sizes of typical molecular clouds embedded in their natal clouds. Should a cloud undergoing gravitational collapse heat up, the collapse can be stopped by rising internal thermal pressure. This highlights the importance of the cloud being able to efficiently radiate the excess heat away. In the next section, star formation is discussed, on scales of the dense cores, starting from the collapse of the prestellar core and concluding with the dispersal of the cloud envelope and formation of the protoplanetary system around a young star.

1.3 Low-mass Star Formation

Star-forming regions close to the Solar System are predominantly not dense and massive enough to form high-mass stars. Given their proximity, it was then a natural observational outcome that the low-mass star-forming regime — yielding the dominant majority of the stars in the Galaxy — was the first one to be extensively studied. As the physical phenomenon of low-mass star formation is not only simpler than its massive counterpart but is also thought to be understood better after decades of intense studies, it is perhaps better to first give an overview of how we think the majority of stars are born before shifting our attention to the formation of massive stars and clusters.

As outlined in the preceding section, star formation occurs exclusively within dark molecular clouds, and the physical processes of star formation are closely tied with that of the molecular cloud, both at the onset of star formation and at the end of the cloud's life (Fig. 1.3). At the early stages of star formation, compact overdensities of about 0.1 pc size (cores) are forming within a more extended molecular cloud material, fragmenting either through the turbulent motions or via gravitational contraction, becoming self-gravitating dense cores that are supported predominantly by thermal pressure. While some of the cores are not dense and massive enough to form stars (starless cores, cf. Fig. 1.3), some accrete enough material (i.e. $M > M_J$ in Eq. 1.1) from their surroundings to form an accreting protostar at their centers. While the collapse of dense cores is thought to produce either single low-mass stars or binaries, the more massive cores, or larger (~0.5 pc) massive density peaks often referred to as "clumps", have the capacity for forming massive stars or clusters of stars, potentially forming H II regions that would act as a major force in cloud destruction. The cores forming low-mass stars, unlike the GMCs, are mainly supported by thermal motions (Goodman et al. 1998; Caselli et al. 2002a), and the subsonic motions across the cores are found to be uniform and appear in sharp contrast with the turbulent motions of their parent clouds (Goodman et al. 1998; Pineda et al. 2010a, 2011a). The collapse of the

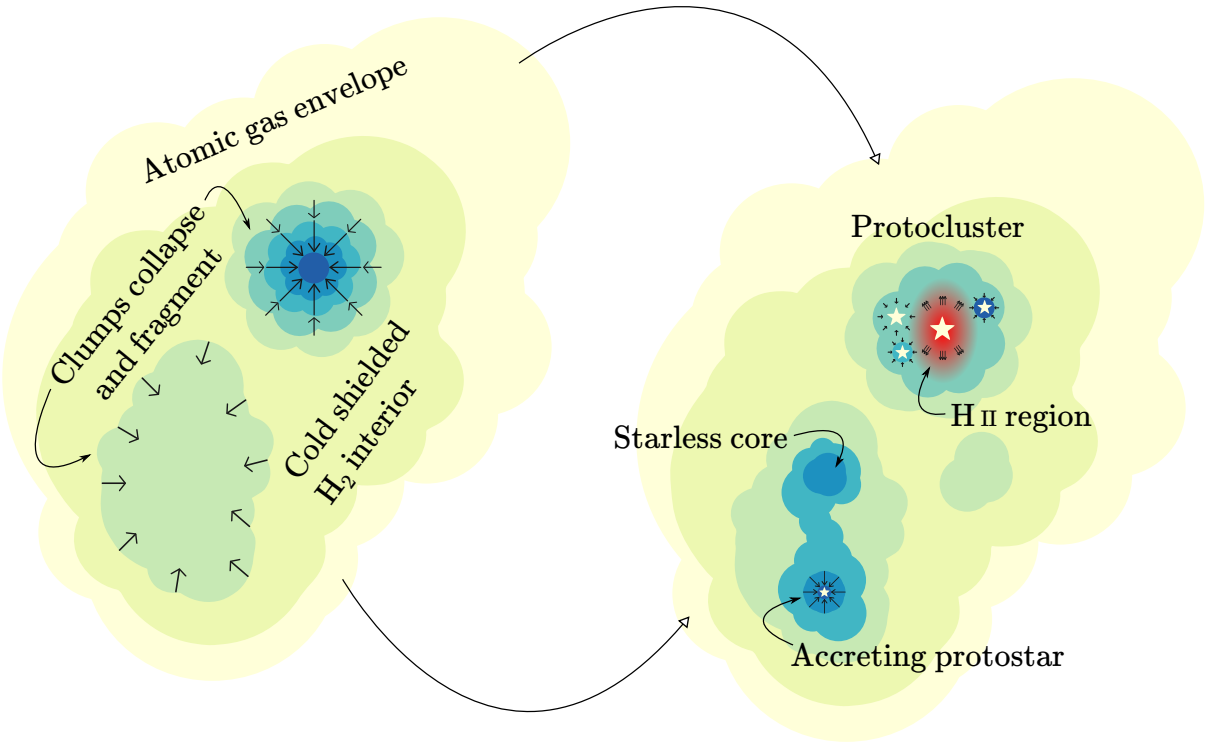

Figure 1.3 A schematic diagram of star formation in molecular clouds, illustrating some of the concepts referred to in the main text. Dense molecular regions are forming within a more extended molecular cloud, fragmenting either through turbulent motions or via gravitational contraction, becoming dense cores. The diagram elements are not to scale. While some of the cores are not dense and massive enough to form stars, some accrete enough material from their surroundings to collapse onto an accreting protostar. More massive cores, often referred to as "clumps", have the capacity for forming massive stars or clusters of stars, potentially forming H II regions that would act as a major force in cloud dissipation.

prestellar dense cores, from the initial transient phase culminating in the formation of central protostar until the late stages, where the stellar feedback strips the surrounding envelope of the star, has been a subject of an active research in the last few decades.

Studies of variable stars in the early 20th century have identified a class of variable stars called T Tauri stars, found in the vicinity of the Taurus molecular cloud (cf. Fig. 1.2). Subsequent studies have found T Tauri stars in other locations in our Galaxy, and have established a close proximity of the T Tauri stars to the dark clouds and young OB stars, suggesting that the T Tauri stars themselves are young stars that still accrete material from their surroundings. Rapid advancement of infrared and radio instrumentation in the second half of the 20th century has revolutionized the star formation field, allowing to peer through the obscuring dust and constrain the emission properties of deeply embedded protostars in dark clouds and filaments. In addition, analytical models and numerical simulations of the protostar evolution progressed hand in hand with the observational studies. As the protostar evolves, its infrared emission properties change. The common features seen in the infrared energy spectra (spectral energy distributions, or SEDs) of the young protostars allowed for an observational classification of the young stellar objects (YSOs) to be established (Lada 1987; André 1995), assigning four classes to the YSOs based on the properties of their infrared emission (summarised in Figure 1.4). This conventional picture of protostar evolution is outlined below, and the YSO classification is mentioned alongside where applicable. The youngest YSOs are associated with dense cores, and the star formation evolution begins there.

At the beginning of the protostellar evolution, the dense core undergoes a free-fall collapse after its self-gravity exceeds the thermal support of the core. The contraction process heats up the gas as the gravitational energy is being released, and the excess energy is radiated away efficiently enough so that the gas can be considered isothermal. As the central density increases (to $\gtrsim 10^{10}$ cm^{-3}, Larson 1969), the dust emission becomes optically thick and the excess energy of the contracting core cannot be radiated away anymore. The central temperature thus begins to rise rapidly, and a short-lived, thermally-supported object (of about 5 AU size and 100 K surface temperature) in the center of the core is formed (called the first hydrostatic core, predicted by Larson 1969, observational candidates include Pineda et al. 2011b, Dunham et al. 2011). The trapped radiation continues to heat up the core, until the H_2 gas is dissociated and another free-fall collapse begins, culminating into a formation of a central protostar. Because the protostar itself is surrounded by opaque envelope, the observed SED appears as a blackbody corresponding to the temperature of the envelope photosphere which re-radiates emission from the protostar, with the luminosity produced by the shocked envelope material infalling on the protostar surface. As the protostellar core evolves, some indirect evidence for an embedded accreting protostar can be detected (e.g., outflow activity or maser emission), but in the infrared wavelengths the collapsing envelope is mainly characterised by the strong thermal submillimetre emission emanating from the protostellar envelope (Fig. 1.4a). In this stage, the embedded YSO is classified as Class 0, and is thought to represent a very young age in protostellar evolution ($\lesssim 10^4 - 10^5$ yr, André 1995; Masunaga & Inutsuka 2000; Hatchell et al. 2007), and is sometimes (e.g., Andre et al. 1993) defined as a protostellar object in which most of the mass is still contained in the envelope. At a more evolved stage, Class I sources represent actively accreting protostars, where the protostellar mass becomes larger than the envelope mass, and the SED has both a strong infrared excess as

well as the black body signatures (Fig. 1.4b). The Class I YSOs are still embedded and carry no optical signatures, but their emission is characterised by the protostellar disk and envelope components. At the end of the Class I phase, most of the stellar material has been accreted, and the circumstellar disk is commonly referred to as protoplanetary in the subsequent stages.

Eventually, the feedback of the embedded YSO clears out the dusty envelope, allowing the protostar emission to be detected in optical wavelength. Moreover, as the envelope is either cleared out or fallen onto the disk and the protostar, the submillimetre component of the SED is almost fully attributed to the protoplanetary disk (Class II, Fig. 1.4c). Finally, Class III YSOs are dominated by the light emanated from their central star, with only a relatively small fraction of infrared flux attributed to the light disk remnant, with disk masses typically below the mass of Jupiter (Fig. 1.4d). Most of the Class II and Class III YSOs are accompanied by visible counterparts with reddened SEDs (e.g., Lada 1987). These visible counterparts, commonly referred to as pre-main-sequence (PMS) stars, are objects that have not yet reached central temperatures hot enough to start fusing hydrogen, and are powered by grabitational contraction and deuterium fusion. The optically visible PMS objects are the aforementioned T Tauri stars (with masses below $M_* < 2\ M_\odot$) and their massive counterparts — Herbig Ae/Be stars ($2 < M_* < 8\ M_\odot$).

The classification above is widely used in observational studies of low-mass YSOs, and it illustrates important and fundamental physical precesses accompanying star formation. However even in the low-mass star regime the observational classification poses some confusion issues, and YSOs are prone to misclassifications due to geometric orientation relative to the line of sight of the protostellar system (Crapsi et al. 2008) and the multiplicity of the protostellar system. Moreover, this classification of low-mass protostar evolution does not directly apply to the formation process of higher-mass stars. The lifetime of a YSO spent in the pre-main-sequence phase gets shorter the more massive the resultant star is. Massive stars, i.e. the stars above $8\ M_\odot$, do not have an observable pre-main-sequence phase at all — they start fusing hydrogen while the outer envelope is still collapsing. This highlights an observational hindrance in observing massive protostars, as they are short-lived and deeply embedded in the obscuring cloud material. Moreover, most stars are born in multiples, either as binary systems or in protoclusters, depending on the initial core mass and the degree of fragmentation the collapsing core undergoes. While classification of protoclusters and the high-mass protostars is made more challenging this way, a large observational effort was made to establish the evolutionary sequence for high-mass star formation.

1.4 High-Mass Star and Cluster Formation

Most massive stars are found in clusters of stars (Roberts 1957). Given this, the processes of cluster formation and massive star formation share a common foundation, and the theories that describe them aim to answer both the questions of how to sustain a high accretion rate needed to support the growth of a high-mass protostar and that of how the mass fragmentation leads to observed stellar mass distributions found in star clusters.

In spite of the apparent complexity of the physical laws governing the outcome of star formation, the distribution of stellar masses at birth is found to be nearly universal. Dedicated

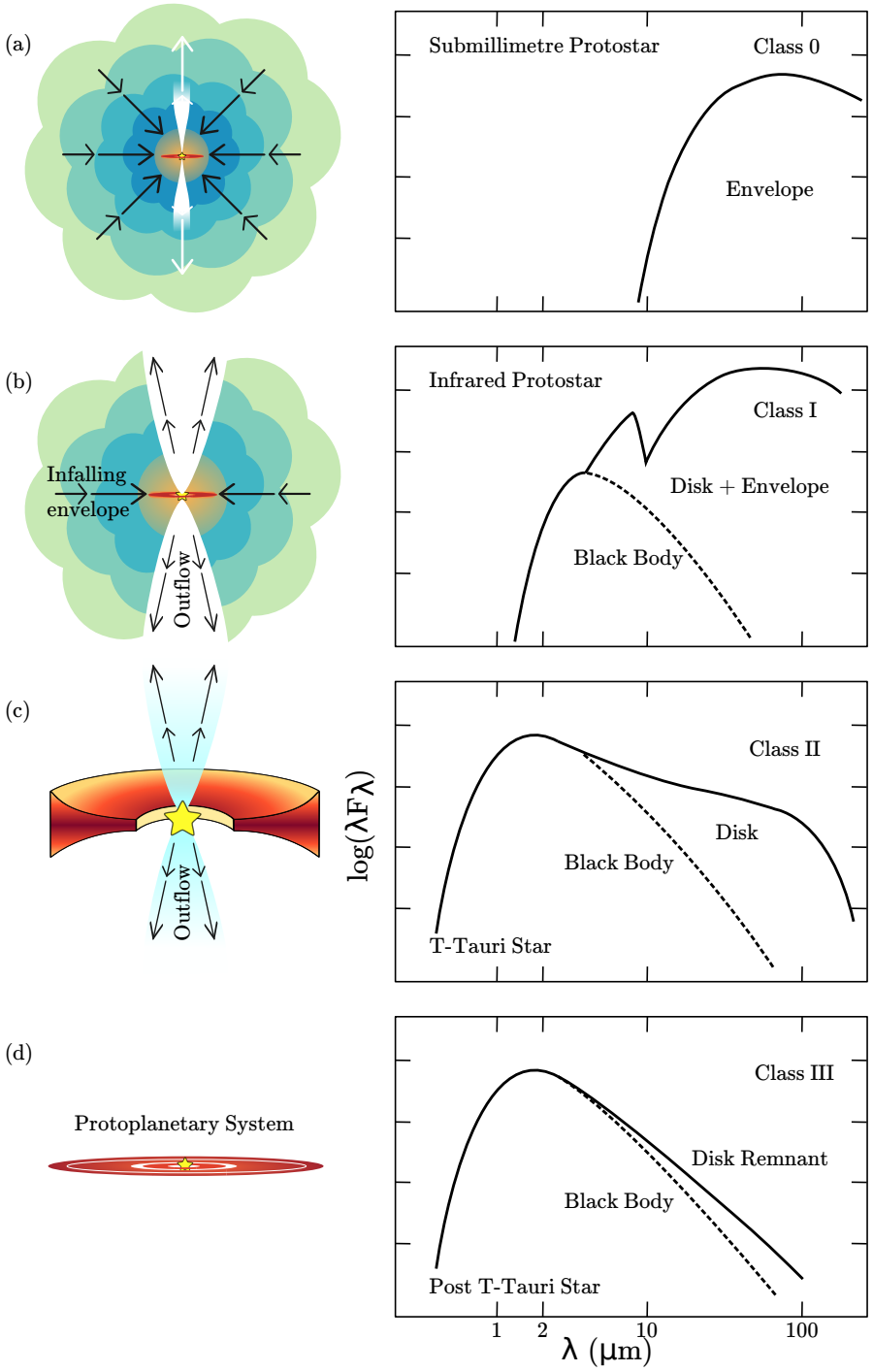

Figure 1.4 A schematic diagram of low-mass protostar evolution. The right-hand side, shows an SED evolution of YSOs from a deeply embedded stage to that of a young stellar system with little trace of disk emission remaining. The SED diagrams for Classes I, II, and III are reproduced from Lada (1987), with an addition of the Class 0 SED.

observational studies of field stars established that the mass distribution of stars at birth follows a quasi-fundamental law called the initial mass function (IMF, reviewed in Chabrier 2003). In particular, massive stars are found to be very rare — only 0.2% are above 10 $M_{\odot}$, and their frequency sharply decreases with mass (power law index of -2.3 ± 0.7, Kroupa 2001).

Despite yielding relatively few OB stars, the high-mass tail of the IMF plays a fundamental role in the evolution of galaxies. Through energetic outflows, copious amount of ionizing flux, and dynamical impact of the SNe explosions they exert a feedback force that dwarfs that of their low-mass counterparts. They thus play a key role not only in reshaping the flow of matter in the ISM, potentially inhibiting or promoting further star formation, but also inject heavy elements into the ISM, ultimately providing building blocks for organic matter in the Universe.

1.4.1 Observational perspective

Given the important role played in the ISM dynamics, it is unfortunate that the origins of massive stars are still poorly understood. The reason for this is that observing the regions of massive star formation is complicated, but can be broken down into several complications in comparison with the formation of low-mass stars. First of all, massive star formation is a relatively rare phenomenon — as mentioned above, among the newborn stars, the high-mass ones account for only a fraction of a percent. Therefore, statistically the regions that are forming massive stars are bound to be rarer and further away than the ones producing Sun-like stars. This can be illustrated by considering the nearby star-forming regions on Fig. 1.2: all the nearby ($d < 200$ pc) star-forming complexes, like Taurus or Ophiuchus, are only capable of forming low-mass stars, while the only relatively nearby ($d \sim 400$ pc) high-mass star-forming complex is the Orion Molecular Cloud (and the typical distances to high-mass star-forming regions are greater than one kiloparsec). Figure 1.5 illustrates the observational scarcity of massive stars, plotting the Hertzsprung-Russel diagram for the nearby ($d < 200$ pc) stars from the Gaia Data Release 2 (Gaia Collaboration et al. 2016, 2018a,b). YSOs from Orion (Kounkel et al. 2018) are overplotted for reference, to illustrate that the more massive stars (upper left corner) have a shorter pre-main-sequence phase. In addition, the massive protostars are obscured by large columns of dust. Typical visual extinctions towards the compact dense cores in nearby low-mass star-forming regions (e.g., $A_{\rm V} = 5 - 20$ mag for cores in the Pipe Nebula, Rathborne et al. 2008) are dozens of magnitudes smaller than the observed extinctions towards the clouds capable of forming high-mass stars (described in detail in §1.4.3). Together with the aforementioned large distances towards high-mass star-forming regions, this restricts the observations of such regions to be conducted with submillimetre and radio interferometers if the scales of individual star formation (i.e., low-mass dense core analogues) are to be resolved. Finally, another observational issue is the timescales of massive star formation. As stated in §1.2, the OB star feedback disperses the parent clouds, a process that occurs within a few million years (e.g., Lada 1987), effectively restricting the observational window into the star formation history of the cloud. Furthermore, as massive star formation does not have a pre-main-sequence phase, the only observational window into the process of mass accretion is the deeply embedded protostellar stage, lasting less than 10^5 years.

How does one find progenitors of the massive stars? Following the observational search for

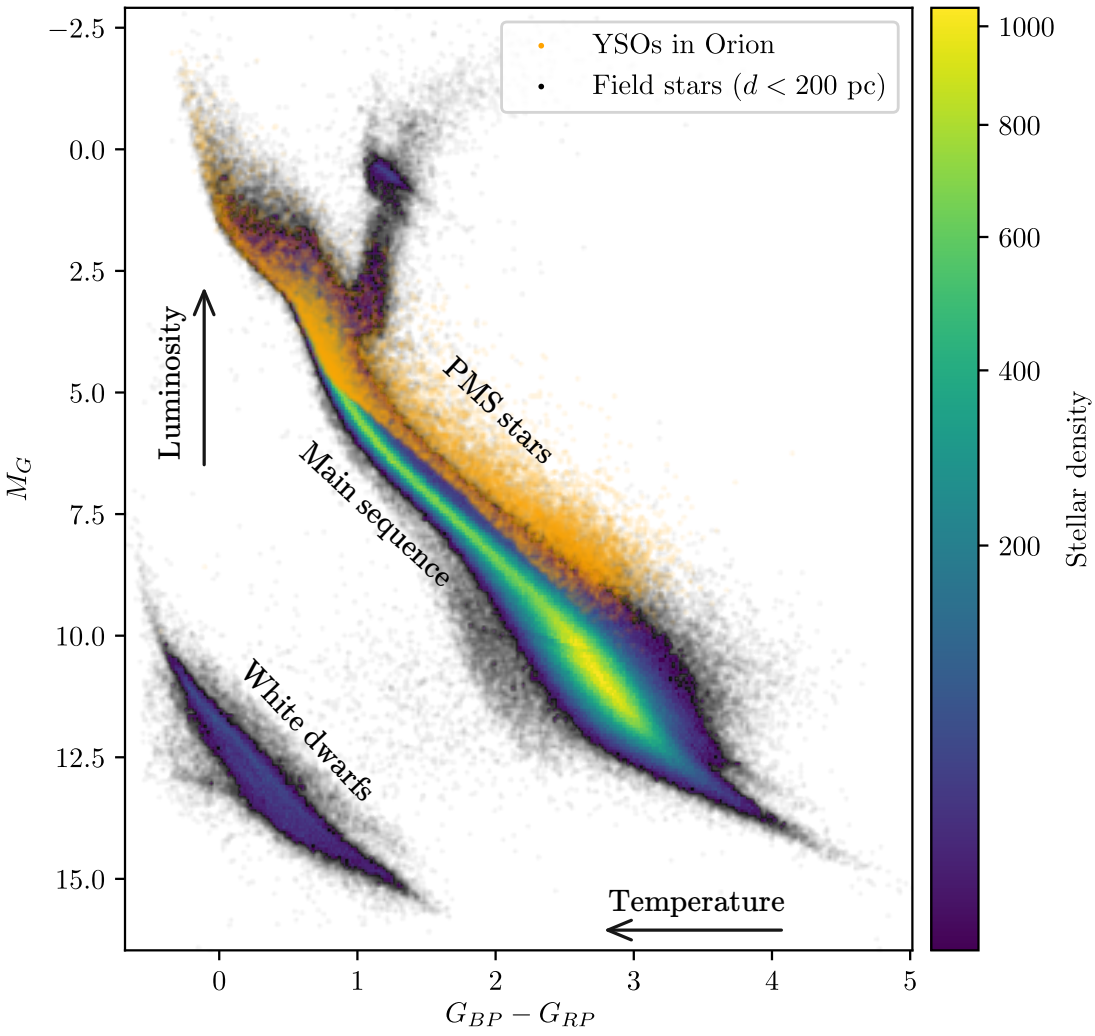

Figure 1.5 A Hertzsprung-Russel diagram of all the stars within the Solar neighborhood ($d < 200$ pc). The Gaia-band absolute magnitude (y-axis) is plotted against the Gaia $G_{BP} - G_{RP}$ color (Gaia is equipped with blue and red color filters). Constructed from publicly available Gaia DR2 data (Gaia Collaboration et al. 2018a) with quality filters taken from Gaia Collaboration et al. (2018b). Regions where the star density is too high (over ten stars per pixels) are visualized with the help of a 2D histogram, as indicated in the color bar. Overlaid on the nearby field star distribution is the population of young stellar objects from the Orion giant molecular complex (following Kounkel et al. 2018).

the early progenitors of massive stars, it is convenient to describe the classification of protostellar stages of massive YSOs while tracing the evolution of massive stars backwards. Historically, the identification of young massive stars begun with detecting compact expanding H II regions — the radio emission of the expanding ionized gas bubble around a young star is one of the first observational tracers of embedded massive stars. Tracing back the process of H II region expansion, the youngest massive stars should be associated with the smallest ionized bubbles around them, and observational search for compact progenitors of H II regions resulted in the discovery of the ultra-compact H II (UC H II) regions (Wood & Churchwell 1989), observationally defined as being of ≤0.1 pc sizes, and $\geq 10^4$ densities (Hoare et al. 2007). Among the hundreds of UC H II objects found, the densest ($\geq 10^6$ cm^{-3}) and most compact (≤0.05 pc) subset became known as hyper-compact H II (HC H II) regions, with sizes and fluxes consistent with being driven by individual or binary massive stars (Beuther et al. 2007). Prior to the appearance of the ionized pocket of gas around a young massive star, warm (≥100 K) temperatures of the protostellar core envelopes cause the ice covering the dust grain surfaces to be evaporated, releasing complex organic molecular species into the gas phase and allowing the core to be spectroscopically detected as a hot molecular core (HMC, reviewed in Kurtz et al. 2000). Before the protostellar core manifests itself as an HMC, however, the complex organic molecules are depleted on the ice mantles of the dust grains. The protostellar signature is still detectable, both as a temperature enhancement in an otherwise cold extended cloud exterior (powered mainly by the accretion luminosity), or through the detection of the massive molecular outflows, commonplace in massive star formation (e.g., Shepherd & Churchwell 1996; Beuther et al. 2002b). This stage, sometimes referred to as high-mass protostellar objects (HMPOs), is thought to harbor a compact unresolved heated gas region at its center, and was found to contain masses of a few hundred to a few thousand Solar masses within ~0.25 – 0.5 pc (Beuther et al. 2007).

While observations of high-mass star formation in relatively evolved stages are abundant, the earliest stages have proven to be more elusive. In these, the dense seeds that are yet to become sites of active star formation are also some of the coldest regions in their parent clouds, and are thus invisible to mid-infrared point source surveys. Observations of GMCs show that high-mass star formation occurs in turbulent dense clumps with surface densities of 500 – 5000 $M_\odot$ pc^{-2} (Tan et al. 2014), yet the theoretical models vary in their predictions as to what processes lead to a formation of a massive protostar. In light of this, predictions from the theoretical models have to be discussed before the observational search for initial conditions of massive star formation is presented.

1.4.2 Theoretical models

As mentioned before, the large energetic output of massive stars is what makes their relatively small numbers stand out in terms of dynamical importance within their host galaxies. The strength of the feedback from massive stars also poses unique challenges to the theories of their formation. The main difference between low- and high-mass star formation is that the massive protostars start fusing hydrogen while still actively accreting material (Kahn 1974), with theoretical models estimating only about 10^5 yr needed to reach the main sequence (e.g., McKee & Tan 2002). Following the rapid development of the high-mass protostars, a newly-formed star

begins to exert a strong radiative feedback onto its immediate surroundings, exerting radiation pressure on the dust grains and hampering the subsequent mass accretion. This poses a challenge to theories describing how massive stars form, because while the classical theoretical models of spherical accretion predict the mass infall to be halted for stars above 7 $M_\odot$ (Shu et al. 1987), high-mass stars are in fact found to exist in abundance (e.g., Garmany et al. 1982). Therefore, a considerable effort went into development of theoretical models in which high accretion rates onto the high-mass protostars can be sustained. The three main classes of theories describing the formation of massive stars can be put into the *core accretion*, *competitive accretion*, and the *coalescence* classes.

To overcome the radiative feedback problem above, the core accretion theories vary the properties of low-mass star formation, proposing a "scaled-up" version of standard model of the low-mass core accretion. Several ideas were proposed to allow the massive stars to grow inside the cores. One of the solutions proposes that massive stars form only in the regions that are relatively dust-free, reducing the radiative feedback and allowing the accretion to continue (Wolfire & Cassinelli 1987). A different approach suggests that the radiation pressure around a young massive star is reshaped by dense circumstellar matter, and the radiation field is reshaped (beamed), relaxing the radiation pressure on the accreting matter. In this picture, the mass infall is not spherical, as in the classical accretion theories, and the material can be funneled onto a protostar either through turbulent instabilities (Krumholz et al. 2005), or through accreting disks (Nakano et al. 1995; Jijina & Adams 1996; Yorke & Sonnhalter 2002). Distancing from the idea that massive stars form in a relatively short time, Keto (2003) propose that accretion can continue through the ionized (HC H II) regions over long periods of time. Finally, large accretion rates were proposed as way of forming high-mass stars in the *Turbulent Core Model*, where the initial massive core is built-up supported mainly by turbulence and magnetic fields, following the collapse onto a massive protostar that provides high accretion rates approaching 10^{-3} $M_\odot$ yr^{-1} (McKee & Tan 2003). While generally massive star-forming regions are thought to be highly turbulent, a specific case a relatively low level of turbulence in a massive star-forming cloud might warrant increased support from the mangetic field is examined in detail in Chapter 3.

An alternative model for high-mass star formation proposes that the material for building a massive star is not initially bound to a star, but is rather funneled onto it by a collective gravitational pull of a star cluster (competitive accretion, Bonnell et al. 2004). The formation of massive stars is therefore a natural extension of cluster formation, where each of the initial thermal Jeans mass seeds compete for their share of mass accreted from the cluster environment, with larger shares going into more massive stars. In this framework, the universal nature of the stellar masses are not probabilistically sampled from the IMF, but rather the IMF is a natural consequence of the competitive nature of protostar feeding (Bonnell et al. 2007). Despite the advantages competitive accretion offers in tying the cluster formation to formation of massive stars, it has its shortcomings, namely, as its relies on spherical accretion that is more prone to be disrupted by stellar feedback (e.g., Tan et al. 2014).

Finally, a different approach altogether was proposed by Bonnell et al. (1998), who, based on the observational evidence that massive stars tend to be found in the centers of star clusters, suggested that high-mass stars form though physical collisions and subsequent merging (coalescence). The issue of overcoming the radiation pressure is thus avoided altogether. However,

the observed densities at the centers of star clusters are much lower than the ones required by the coalescence scenario ($\sim 10^8$ pc^{-3}). While follow-up studies focused on reducing the stellar density threshold (e.g., $\sim 10^6$ pc^{-3} for binary systems Bonnell & Bate 2005), the coalescence scenario might play a role in the formation of very massive ($> 50\ M_\odot$) stars in clusters with extreme central stellar densities (Moeckel & Clarke 2011).

The extent to which the above theories manifest in high-mass star formation is currently under debate, and their relative importance in different mass regimes has been revised over the years. For instance, the initial lack of numerical capacities prevented the 2D- and 3D-models of massive star formation to be investigated, yet by mid-2000's non-spherical accretion simulations were shown to yield higher-than-before stellar masses, thereby extending the core accretion models into regime previously occupied by the coalescence scenario. The wealth of the theoretical studies can be seen as a consequence of limitations of observational capabilities, as only with recent advances in interferometric instrumentation the initial conditions for high-mass star formation could be directly probed, providing much-needed constraints on theoretical models.

1.4.3 IRDCs as the initial conditions of massive star formation

The observational search for the earliest progenitors of the high-mass stars has culminated in the detection of a class of objects known as infrared dark clouds (IRDCs). The IRDCs were first found in the late 1990's, when the advances in space-borne mid-infrared telescopes allowed for large-scale photometric surveys to be conducted. The large-scale surveys of the Galactic plane, such as the *Midcourse Space Experiment* (MSX, Egan et al. 1998; Carey et al. 1998, 2000), the *Infrared Space Observatory* (ISO, Perault et al. 1996), and follow-up *Spitzer* GLIMPSE (Churchwell et al. 2009) observations have discovered a large number of compact dark features, seen in extinction against the bright diffuse galactic background (Simon et al. 2006a,b; Rathborne et al. 2006; Peretto & Fuller 2009). The IRDCs were subsequently widely recognized as best candidates for harboring the long-sought initial stages for massive star and cluster formation (e.g., Rathborne et al. 2006). Follow-up studies in far-infrared, submillimetre, and radio wavelengths have established a high degree of fragmentation in these clouds, revealing high-mass dense cores residing in some IRDCs. The cores were found to be in various evolutionary stages, ranging from dark, cold, and quiescent cores to sites of active high-mass star formation, with infrared-bright and chemically complex sources driving massive molecular outflows and H II regions (e.g., Beuther et al. 2002a, 2005; Pillai et al. 2006; Chambers et al. 2009; Sanhueza et al. 2012; Wang et al. 2011, 2014). Although the IRDCs do not represent a single evolutionary stage of star formation overall and not all of the IRDCs are massive enough to form high-mass stars (Kauffmann & Pillai 2010), the most massive and coldest regions within them do, as the clumps within IRDCs were found to be cold ($10 - 15$ K), filamentary, and high-column-density ($10^{23} - 10^{25}$ cm^{-2}) and of high masses ($10^{3-5}\ M_\odot$, Kainulainen & Tan 2013).

To narrow down the search for clouds capable of hosting high-mass star progenitors, Rathborne et al. (2006) have selected 38 clouds with the highest extinction and known kinematic distance from the Simon et al. (2006b) sample containing over ten thousand IRDCs, and have studied their continuum emission, finding embedded high-mass cores with a median mass of 120 $M_\odot$. Among the Rathborne et al. (2006) sample, Butler & Tan (2009) have analyzed the mid-infrared

extinction of ten IRDCs, selecting the clouds that were nearby, massive, had high contrast with their background, and exhibited relatively simple diffuse emission. Subsequently, Butler & Tan (2012) have studied a number of compact ($R \sim 0.1 - 0.2$ pc) dense cores in the Butler & Tan (2009) clouds, embedded in these ten IRDCs from the extinction maps. Kainulainen & Tan (2013) have improved on the Butler & Tan (2009, 2012) extinction mapping, developing an improved near-infrared and mid-infrared extinction technique that better captures the surface density of extended molecular cloud envelopes.

The IRDCs are often put in context of star formation within GMCs. The GMC density is found to be highly structured, and the densest regions of the GMCs often appear as filamentary networks. The densest parts of the GMCs, when aligned in front of the Galactic plane, would appear as extinction ridges. For ten IRDCs, Kainulainen et al. (2011) found them to be density enhancements within their parental giant molecular clouds, with the IRDCs only accounting for a small fraction ($10 - 15$ %) of the total mass reservoir. Using the archival ^{13}CO Galactic Ring Survey data (GRS, Jackson et al. 2006), Hernandez & Tan (2015) have found that all 10 IRDCs from the Butler & Tan sample correspond to their GMC counterparts, in agreement with similar results by (Schneider et al. 2015).

The target of this work is IRDC G035.39–00.33 (hereafter referred to G035.39), denoted as Cloud H in the (Butler & Tan 2009, 2012) cloud sample. IRDC G035.39 is a massive ($\sim 1.7 \times 10^4$ M$_\odot$, Kainulainen & Tan 2013) and highly filamentary IRDC located at 2.9 kpc distance in the W48 molecular complex (Simon et al. 2006b). Its high column density (3×10^{23} to 8×10^{23} cm^{-2} Henshaw et al. 2016a) causes it to appear as an extinction feature at wavelengths as far as 70 μm. The IRDC has been a subject of extensive studies over the last ten years. The previous observational work has established that the cloud's extended gas structure is highly reminiscent to that of the cold starless gas: on pc-scales, the cloud appears dark in mid-infrared wavelengths, and the derived temperature structure is not only relatively smooth, showing no indications of embedded star formation, but also cold (15 - 17 K, Nguyen Luong et al. 2011). Furthermore, the quiescent cold chemistry of G035.39 is also confirmed by observations showing the CO molecules to be frozen out on the dust grains (Hernandez et al. 2011, 2012; Jiménez-Serra et al. 2014), and the relatively high abundances of deuterated species, suggesting early stage of chemical development (Barnes et al. 2016). The IRDC exhibits a kinematically complex structure. In the northern part of the cloud, multicomponent kinematics was found via dense molecular gas tracers, with the velocity components appearing to dynamically interact with the massive cores in the cloud (Henshaw et al. 2013, 2014; Jiménez-Serra et al. 2014). Despite the cloud not showing signs of star formation feedback on large, pc-scales, the IRDC is not devoid of star formation. Nguyen Luong et al. (2011) find 70 μm *Herschel* sources in 13 massive dense cores ($20 - 50\ M_\odot$) in the cloud, and argue that these cores have the capacity to form intermediate- and high-mass stars.

Given its quiescent state on cloud-scales (> 1 pc), high mass surface density, complex kinematics, and the presence of protostellar sources capable of massive star formation on small scales (< 0.2 pc), IRDC G035.39 is a good target for investigating the initial conditions of massive star and cluster formation.

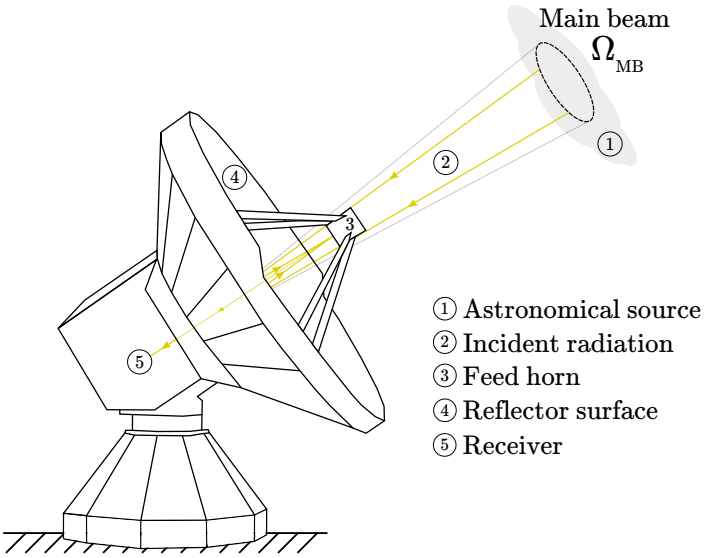

Figure 1.6 Basic components of a single dish telescope. The intensity of an astronomical source is observed in the main beam of the antenna with a solid angle Ω_{MB}. The incoming radio waves are focused by the reflector surface into the feed horn, and the output voltage is measured and amplified at the receiver.

1.5 Methods

1.5.1 Radio Instrumentation

Most of the perceivable information about the Universe is detected through the means of electromagnetic radiation. Historically, astronomical measurement of electromagnetic radiation has been limited to the visible wavelengths, but rapid advances in 20th century instrumentation expanded past this boundary. Earth's atmosphere allows for unhindered transmission of radio signals with wavelengths ranging roughly from one centimeter to eleven meters, and beginning from early 1930's, radio emission was shown to emanate from extraterrestrial sources. Subsequent decades, fueled partially by improvements in military radar technology, have shown a great progress in mapping the sky in radio diapason, establishing radio astronomy as an indispensable tool in understanding the cosmos.

A typical radio telescope, like the world's largest steerable Robert C. Byrd Green Bank Telescope (GBT), used in Chapter 2 of this thesis to trace the large-scale emission from G035.39, is composed of an antenna and a receiver (basic telescope components illustrated on Fig. 1.6). The antenna is designed to focus and collect the incident electromagnetic radiation. For parabolic antennae, the focused radiation is collected at the feed horn and is transformed into output voltage which is channeled into receiver. The process of correcting for atmospheric and instrumental losses, as well as subtracting any background noise components is called calibration, a process which transforms the output voltage into the physical units describing the incident radiation from

an astrophysical source. Because the astronomical sources tend to be extremely weak, radio telescopes tend to have antennae with large collecting areas connected to very sensitive receivers.

An antenna receives different amounts of power in different directions. The main component of the power pattern of an antenna is the main beam — the better the power pattern is concentrated in the main beam, the less signal loss is suffered. The signal loss occurs primarily through the sidelobes, axisymmetric features in the power pattern away from the main beam. The main beam is related to the wavelength-dependent angular resolution of the telescope θ_λ, which is typically described by the beam half-width, i.e., the angle between the maximum power and the point when it decreases by a factor of two. Because the angular resolution at wavelength λ and telescope diameter D is approximately $\theta_\lambda \approx \frac{\lambda}{D}$ radians, radio observations, already limited by long wavelength, require large telescope sizes to achieve high angular resolutions. Building a radio telescope large enough to match the resolution of optical telescopes is an engineering near-impossibility. Although the largest steerable antennae built have diameters of about a hundred meters, at the wavelength of 1 cm that translates in angular resolution about $20''$ only, while the state-of-the-art optical observatories can easily achieve sub-arcsecond resolution.

The resolution of a radio telescope, however, can be improved if two telescopes separated by distance s (baseline) are used simultaneously as an interferometer. Unlike the single-dish telescopes, the angular resolution of a two-dish interferometer is approximately equal to $\theta_\lambda \approx \frac{\lambda}{s'}$, where s' is the projected distance between the two antennae on the plane of sky (Fig. 1.7). In a simplified picture of radio interferometry, the incoming radio wave from a far-away source is measured at both receivers with a phase delay corresponding to the extra time (geometric time delay) taken by the wave to reach the farthest antenna, $\tau = \frac{\sqrt{s^2 - s'^2}}{c}$, and the two signals are multiplied and averaged at the correlator, yielding an interferometer response function that depends only on the brightness of the source, its location on the sky, and the baseline geometry. The two-antenna setup above is only sensitive to one Fourier component of the sky intensity distribution corresponding to its instantaneous baseline, and the information about other spatial scales is lost.

In a more realistic case where the full intensity distribution on the sky is to be reconstructed, an aperture synthesis technique is commonly used. In aperture synthesis, the response of the interferometer is described by a complex visibility function $V(u, v)$ in the uv-plane[6], related to the observed image intensity $I(x, y)$ in sky coordinates through the Fourier transformation. The inverse transformation, which reconstructs the intensity of the image observed from the interferometric data, is hindered by the incompleteness of the visibility sampling in the uv-plane. To overcome the sampling issue, collections of antennae are commonly used to operate together, with a large number of baselines between each pair of antennae, which, together with Earth rotation, provides sufficient spatial information to recover the image at high resolution. For example, one of the largest radio interferometers, the The Karl G. Jansky Very Large Array (JVLA), used in Chapters 3 & 4 in combination with GBT, is composed of 27 antennae arranged in a Y-shape array, with 351 baselines each having a unique instantaneous resolution. Its longer baselines are more sensitive to small-scale details of the image recovered, while the shorter baselines provide information on more extended emission from the radio source, allowing to efficiently map ra-

[6] defined as a rectangular coordinate system aligning with the plane wave of the incident signal

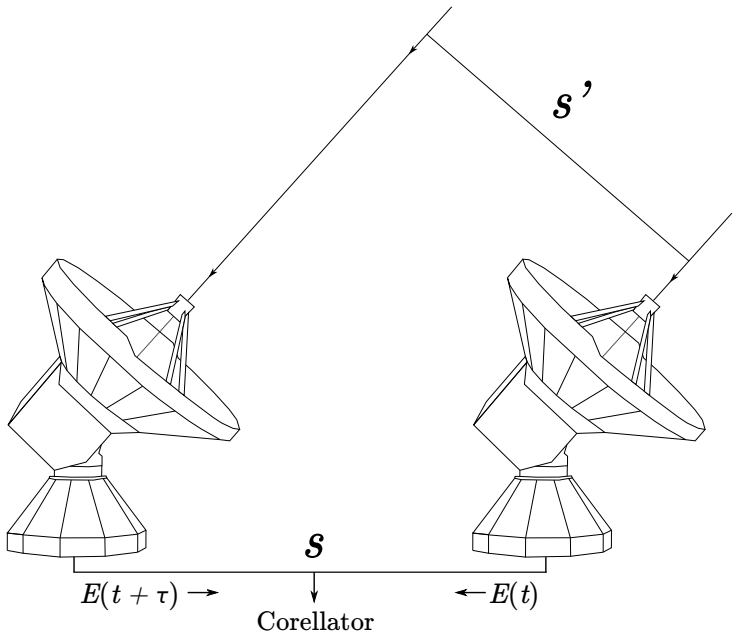

Figure 1.7 A schematic diagram of a two-component radio interferometer. An incoming radio wave is measured at both antennae with a phase shift, and the two signals are processed together at the correlator.

dio emission from astronomical sources. Even at its most compact D-configuration, JVLA can achieve angular resolutions below the angular sizes of dense cores (~0.1 pc) in the nearby (< 3 kpc) IRDCs.

1.5.2 Radiative Processes in the Dark Clouds

As the introduction to the observational techniques outlined above intends to put the methods in the following chapters into a more general context, the nature of the emission sources used has to be explained as well. As the early stages of star formation occur exclusively in dense and cold moleclular clouds, what are the best methods to trace cold and dense molecular interior of the dark clouds, and what is the emission mechanism behind them?

Before this question is answered, another one has to be posed. If molecular hydrogen is the most abundant molecule in the dark clouds, *why can't H_2 be observed directly?* In cold molecular clouds, the radiative emission from diatomic molecules like H_2 occurs through rotational transitions (rotational states are conventionally denoted by J, a quantum number describing the quantization of the total angular momentum). However, molecular hydrogen is not an efficient rotator (it has no electric dipole), and its lowest rotational energy levels are widely separated. In fact, the lowest-energy transition allowed, from the $J = 2$ energy state to the ground level of $J = 0$, is extremely unlikely to occur in cold molecular environment because the excitation temperature of the $J = 2$ state is 510 K. At typical temperatures in cold molecular clouds (10 – 20 K),

the fraction of H_2 molecules in the $J = 2$ state is negligible. As such, tracers of H_2 are observed instead of direct observations of H_2 emission. The CO molecule is generally considered to be a good proxy for H_2 (recall that CO is the main probe of the GMCs; §1.2.1), but in the dense and cold environments of infrared dark clouds CO depletes onto the surfaces of dust grains, and higher-density tracers are typically used. Two of such tracers, namely, the continuum emission from dust grains (used in Chapter 2 to derive the density of G035.39) and the inversion emission from ammonia molecules (used in Chapters 2 – 4), are described below.

1.5.3 Blackbody Dust Emission

As described in §1.2, molecular clouds have high column densities of dust, causing most of the visible light passing through the clouds to be absorbed or scattered. For molecular clouds with $A_V = 5$ mag[7], only 1% of the visible light is able to pass through the cloud, while for the densest regions of the infrared dark clouds ($A_V \approx 100$ mag, Kainulainen & Tan 2013) the prospects for a photon in the visible spectrum are much more dim — only 1 in 1^{40} photons will reach an external observer! In these dense conditions, the photons that are not scattered by the dust are absorbed by the dust grains, heating up the molecular cloud material. The excess heat from the dust grains is radiated away as a blackbody radiation, observable through infrared observations. This thermal emission from the dust grains peaks in far-infrared for cold (10 – 30 K) dust can be detected with instruments operating in infrared spectrum, and is a commonly used observational window into cold dust composition both in and beyond Milky Way.

The thermal emission from dust grains can be understood within a simple physical model of radiation travelling through a slab of material, illustrated on Figure 1.8. If the specific intensity entering the slab of thickness ds is I_ν, then the interaction with the dust grains along the propagation path will cause part of the radiation to be absorbed and scatted away from the line of sight. However, the scattering from other directions into the one along the line of sight (i.e. towards the observer), as well as the emission of thermal radiation from the dust grains, can act against the reduction in I_ν. If the total change in specific intensity along the path ds is denoted by dI_ν, the change is described in the *radiative transfer equation*:

$$dI_\nu = -\rho\kappa_\nu I_\nu ds + j_\nu ds, \tag{1.3}$$

where the two terms $-\rho\kappa_\nu I_\nu ds$ and $j_\nu ds$ are composite terms for absorbing and emitting photons, respectively. In the first one, it is clear that the absorption of incoming emission is proportional both to the total density ρ of the medium containing obscuring dust particles, and the strength of the incoming radiation itself. The remaining coefficient κ_ν, called the *opacity*, describes how efficient the given density of dust grains is in absorbing or scattering the radiation of certain frequency. The second term, responsible for both the thermal emission and the scattering contributions to I_ν depends on the *emissivity* j_ν.

The equation of the radiative transfer (Eq. 1.3) is often reparametrized by defining a *source function* as $S_\nu \equiv j_\nu/\kappa_\nu$. This introduces another useful quantity, *optical depth* $\tau_\nu = \int \kappa_\nu ds$, which

[7] Visual extinction can be converted to gas column density as N_H (cm^{-2}) = 1.9×10^{-21} A_V (mag) (e.g., Kainulainen & Tan 2013)

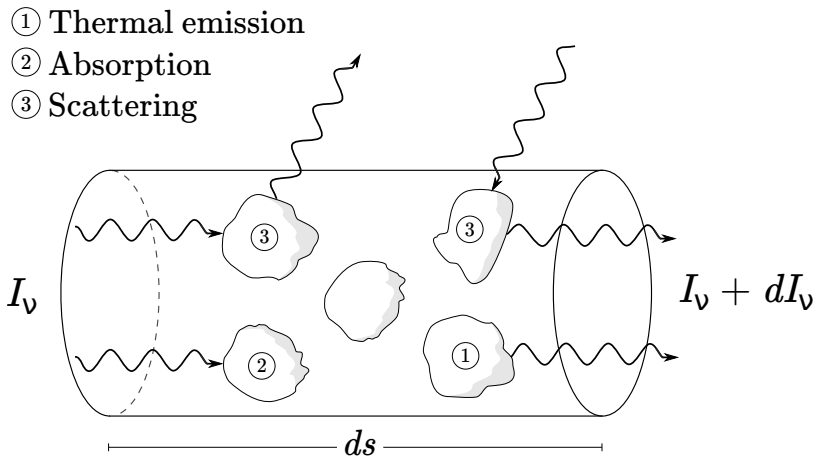

Figure 1.8 An illustration of radiation passing through a portion of molecular cloud of thickness ds. The initial specific intensity I_ν entering the slab is affected by absorption, scattering, and emission of radiation, resulting in a total change of dI_ν in specific intensity. Each of the processes contributing to dI_ν is marked on the diagram. The diagram was heavily influenced by Figure 2.9 in Stahler & Palla (2005).

describes the opacity of the medium: a medium is said to be optically thick if $\tau_\nu \gg 1$, meaning that a photon can not pass though it without being absorbed; similarly, a medium with $\tau \ll 1$ is considered optically thin. Rewritten in terms of source function and optical depth, the radiative transfer equation becomes

$$\frac{dI_\nu}{d\tau_\nu} = -I_\nu + S_\nu, \tag{1.4}$$

and, assuming that the source function is uniform along the line of sight, can be solved for the emergent intensity:

$$I_\nu = I_0 e^{-\tau_\nu} + (1 - e^{-\tau_\nu}) S_\nu, \tag{1.5}$$

where I_0 is the intensity at the optical depth $\tau_\nu = 0$.

In a general case, the equation above dictates that the specific intensity as measured by an observer at frequency ν is a sum of the background source contribution, partially absorbed by the optical depth of the intervening cloud. In a simpler case when there is no background source, the only emission measured by an observer is that of the cloud itself. Assuming the cloud is in thermal equilibrium, the source function S_ν equals to the blackbody radiation according to Kirchhoff's Law: $S_\nu = B_\nu$, where the blackbody radiation is described by Planck's Law:

$$B_\nu(T) = \frac{2h\nu^3}{c^2} \frac{1}{e^{\frac{h\nu}{kT}} - 1} \tag{1.6}$$

The intensity of thermal dust emission from an optically thin source of temperature T can thus be approximated as (cf. Rybicki & Lightman 1979)

$$I_\nu = B_\nu(T) \times (1 - e^{-\tau_\nu}) \approx B_\nu(T)\tau_\nu, \tag{1.7}$$

where $B_\nu(T)$ is a Planck blackbody function. In the expression above, the opacity τ_ν is related to gas column density $N_{\mathrm{H_2}}$ in the following way:

$$\tau_\nu = \int \kappa_\nu \rho \mathrm{d}s = N_{\mathrm{H_2}} \mu_{\mathrm{H_2}} m_{\mathrm{H}} \kappa_\nu, \tag{1.8}$$

where $\mu_{\mathrm{H_2}} = 2.8$ is the molecular weight per hydrogen molecule (assuming the elemental fraction of helium atoms to be 10%) and m_{H} is an atomic mass of hydrogen. The optically thin approximation in Eq. 1.7 holds well for the column densities of 10^{23} cm^{-2} and lower.

As seen from Eq. 1.7 & 1.8, the observed radiation depends on the total column depth of the dust particles, the Planck function for a blackbody of the temperature the same as the dust grains, and the opacity and its spectral variations. This approximation of the dust emission profile allows (given measurements of intensity in several frequencies) to estimate both the dust temperature and its column density. Cold dust, found to be mixed with the molecular gas, emits optically thin radiation in far-infrared regime (the approximation holding well for the typical column density ranges in molecular clouds and dense cores). With the advent of infrared instrumentation, and in particular with the launch of the high-angular resolution, large field of view *Herschel* instrument, thermal emission from the cold dust could be time-efficiently measured across the Galactic plane, and its thermal properties could be reliably constrained.

Despite the efficiency of the method described above, its applications to constraining the temperature and density of the earliest stages of massive star formation, and infrared dark clouds in particular, are limited both in terms of reliability as well as angular resolution. For the latter one, the typical approach of using photometric mapping capabilities of the *Herschel* Space Observatory results in temperature measurements with an angular resolution of about 36″ (diffraction limited by the largest wavelength measured by *Herschel*), which, for typical distances of nearby IRDCs, corresponds to the physical scales of ∼0.5 pc. Therefore, while this method might reliably constrain temperatures of extended cloud material, the resolution is not enough to probe the typical sizes of the embedded cores that are more representative of the initial conditions for massive star formation. Another issue that stands in the way of the temperature and density estimation is line of sight mixing of emission unrelated to the cloud. IRDCs are, as their very definition requires, aligned with the bright Galactic background emission. Recalling that the dust is expected to be optically thin, the thermal dust emission observed will be contaminated by emission from the warmer, more diffuse dust located either behind, or in front of the cloud. This will introduce a systematic bias in estimating the physical properties of the IRDC interior, and is discussed more in depth in Chapter 2 (published as Sokolov et al. 2017). While there are ways to correct for this systematic effect, this brings the discussion to a different approach based on molecular emission, which is invariant to the dust optical properties and the line of sight mixing. In addition to the aforementioned advantages, using molecular emission as a tracer of dense gas provides another advantage: knowledge of the gas kinematics. Because the molecular emission

frequency is systematically modified due to the motion of the radiation source, relative motions in the molecular cloud can be measured. Additionally, the line emission is broadened relative to the Doppler-shifted rest frequency, and the resulting line width serves as in indicator of gas dynamics.

It has to be noted that while the physical model above was introduced specifically for the dust grain emission, the equation of radiative transfer is a general model for propagation of radiation in the interstellar medium, and can be applied for the molecular emission, as will be seen in the following section.

1.5.4 Ammonia inversion transitions

An alternative to measuring thermal dust emission as a proxy for gas density and temperature is to observe the emission from ammonia molecules, found in abundance (about 2×10^{-8} with respect to H_2 in, e.g., IRDC G035.39, Sokolov et al. 2017) in cold molecular gas. The ammonia molecule is a pyramidally-shaped compound with a Nitrogen atom bound to three Hydrogen atoms, and was one of the first molecules discovered in the interstellar medium (Cheung et al. 1968). Since its discovery towards the Galactic center, it has been detected towards a multitude of cosmic environments, and in particular has proven to be an invaluable tool in probing physical conditions of moderately dense molecular regions (e.g., Myers & Benson 1983; Rosolowsky et al. 2008a; Pillai et al. 2006; Pineda et al. 2010a; Wang et al. 2012, 2014).

The main routes of ammonia formation and destruction are as follows. The formation routes can occur through gas or dust grain surface routes. In the gas phase, the principal pathway for ammonia formation occurs via consequent abstraction reactions of N^+ with H_2 (Herbst & Klemperer 1973):

$N^+ + H_2 \longrightarrow NH^+ + H,$

$NH^+ + H_2 \longrightarrow {NH_2}^+ + H,$

${NH_2}^+ + H_2 \longrightarrow {NH_3}^+ + H,$

${NH_3}^+ + H_2 \longrightarrow {NH_4}^+ + H,$

followed by a dissociative recombination resulting in the formation of an ammonia molecule:

${NH_4}^+ + e^- \longrightarrow NH_3 + H.$

An alternative formation route is for an ammonia molecule to be formed on the surface of dust grains, where the consequent hydrogenation of the N atom results in the NH_3 molecule. In dense gas, NH_3 is removed from the gas phase in dense gas through freeze-out on the dust grains and is photodissociated in lower-density regions.

The symmetric top NH_3 molecule undergoes rotational motions, rotating around its symmetry axis (A-axis on Fig. 1.9a) with the associated angular momentum of $\boldsymbol{J_A}$. Additionally, the symmetry axis itself precesses around vector $\boldsymbol{J}$ which denotes the total angular momentum. The rotation energy levels of ammonia can be described with two quantum numbers: J, relating to its total angular momentum; and K, and its projection along the symmetry axis. The energy states with $J > K$, called non-metastable states, decay rapidly through infrared emission to metastable $J = K$ states. The metastable states, in turn, are populated mainly through collisional reactions with the gas particles, making ammonia a good probe of the gas temperature.

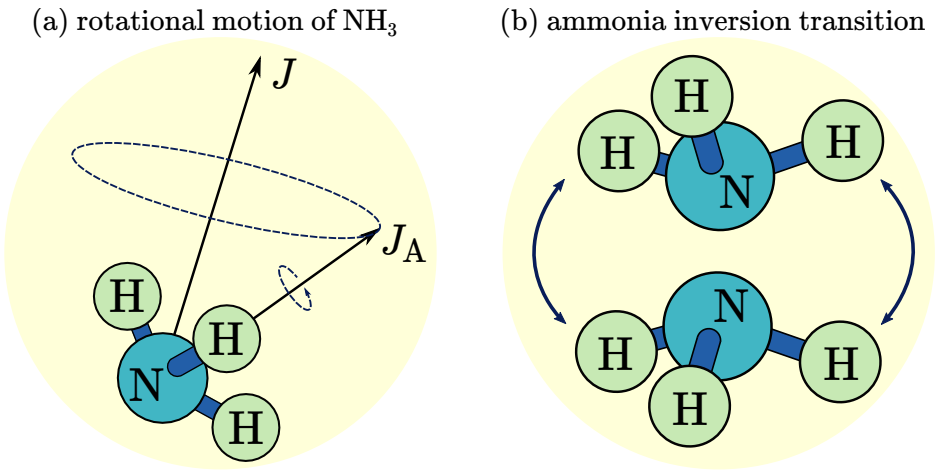

Figure 1.9 (a) Rotational degrees of freedom of the NH_3 molecule, along with the axes of rotation labelled (adapted from Figure 5.11 in Stahler & Palla 2005); (b) a schematic diagram of the inversion transition of the ammonia molecule.

The NH_3 molecule also exhibits vibrational motions in addition to the rotational ones described above. In particular, the Nitrogen atom can tunnel through the plane defined by the three H atoms (Figure 1.9b), producing a splitting of (J,K) rotational levels into inversion doublets with opposite parity. The energy separation of the doublets places the resulting electromagnetic emission into the microwave K-band regime. The inversion doublets are further split by hyperfine interactions. The interaction between the nitrogen nucleus' electric quadrupole moment and the molecular rotation splits the inversion doublets into a main hyperfine line component with two satellite pairs; the energy levels are split even further by weaker magnetic interactions between atomic spins (cf. Fig. 2 within Ho & Townes 1983), resulting in a total of 18 and 21 hyperfine components for (J,K) = (1,1) and (2,2), respectively.

The population ratio of the given upper (J_u, K_u) and lower (J_l, K_l) inversion states is related through the Boltzmann's law:

$$\frac{N_{(J_u,K_u)}}{N_{(J_l,K_l)}} = \frac{2J_u + 1}{2J_l + 1} \exp\left(-\frac{\Delta E_{ul}}{k_B T_{\rm rot}^{ul}}\right). \tag{1.9}$$

As the metastable $J = K$ states are populated mainly though collisions, the population ratio of the $(J, K) = (1, 1)$ and $(2, 2)$ inversion states is often used as an approximation for the rotational gas temperature (Ho & Townes 1983):

$$T_{\rm rot}^{21} = -T_0 \,/\, \ln\frac{5N_{(2,2)}}{3N_{(1,1)}}, \tag{1.10}$$

where $T_0 = 41.5$ K corresponds to the energy difference between the (1,1) and (2,2) levels. This temperature is commonly used as a proxy value for the actual temperature of the medium, derived through balancing the rates of radiative and collisional transitions (Walmsley & Ungerechts 1983; Tafalla et al. 2004; Swift et al. 2005). The widely adopted practice to derive the rotational gas

temperature is to calculate the ratio of the (1,1) and (2,2) populations from the observed line transitions and then scale the rotational temperature to the kinetic one via the relation below (Swift et al. 2005):

$$T_{\rm rot} = T_K \left\{ 1 + \frac{T_K}{T_0} \ln \left[1 + \frac{3}{5} \exp\left(\frac{-15.7\ {\rm K}}{T_K} \right) \right] \right\}. \tag{1.11}$$

In the Rayleigh-Jeans approximation, an observed spectral profile of inversion lines along with its hyperfine components can be described as a sum over its hyperfine components, assuming uniform excitation conditions for all the hyperfine components of the line and a unity beam filling factor:

$$T_{\rm MB}(v) = \sum_i \left\{ 1 - \exp\left[-r_i\ \tau_0\ \exp(-\frac{(v_{\rm off} - v_i)^2}{2\sigma_v^2}) \right] \right\} (T_{\rm ex} - T_{\rm bg}), \tag{1.12}$$

where $T_{\rm ex}$ describes the population ratios of the inversion transition parity levels, the background radiation temperature $T_{\rm bg}$ is taken to be that of the cosmic microwave background (2.7312 K), the values for r_i are normalized relative intensities of the hyperfine components representing absorptive properties of each component, and are calculated from the theoretical modelling, v_i is the velocity centroids of the hyperfine components, σ_v is the line width of the line, and τ_0 the main group opacity of the corresponding inversion line. The latter can be used to derive the column density of the (1,1) rotational state, $N_{(1,1)} = N_l + N_u$, (Rosolowsky et al. 2008a):

$$N(1,1) = \frac{8\pi k \nu_0^2}{hc^3} \frac{1}{A_{1,1}} \sqrt{2\pi}\sigma_\nu (T_{\rm ex} - T_{\rm bg})\tau_0, \tag{1.13}$$

which can then be used to derive a total ammonia column density $N_{\rm tot}$ by scaling it with a partition function $Z(T_{rot}, J = K)$, assuming that only the metastable population levels are populated (Rosolowsky et al. 2008a):

$$N_{\rm tot} = N(1,1) \frac{\sum_i Z(T_{\rm rot}, J_i)}{Z(T_{\rm rot}, J = 1)}. \tag{1.14}$$

1.6 This Thesis

Following the introduction to the subject, the next chapters go into detail of IRDC G035.39, its physical and dynamical state. The following list gives a summary of each chapter that follows.

- Chapter 2 describes the large-scale temperature structure and the dynamical state of a G035.39 in early stages of its evolution. It also provides a direct comparison between dust- and ammonia-derived temperature structure, and argues that the latter provides better constraints on the temperature of the dense gas, while the former must account for line-of-sight contamination prevalent for infrared dark clouds.

- Chapter 3 zooms into the smaller scales of the G035.39, using interferometric observations of ammonia inversion emission to assess the turbulent structure of the region, finding it to be unexpectedly devoid of large turbulent motions.

- In Chapter 4, the complicated multicomponent structure of cloud's kinematics is shown for the whole G035.39. A detailed comparison between the region's kinematics and temperature with the classical picture of star formation is provided.
- Chapter 5 concludes this thesis, providing a summary and future outlook.

Chapter 2

Temperature structure and kinematics of the IRDC G035.39–00.33

The contents of this chapter were published in *Astronomy & Astrophysics* Journal.
Credit: Sokolov et al., A&A, 606, A133, 2017, reproduced with permission © ESO.

2.1 Abstract

Aims. Infrared dark clouds represent the earliest stages of high-mass star formation. Detailed observations of their physical conditions on all physical scales are required to improve our understanding of their role in fueling star formation.

Methods. We investigate the large-scale structure of the IRDC G035.39–00.33, probing the dense gas with the classical ammonia thermometer. This allows us to put reliable constraints on the temperature of the extended, pc-scale dense gas reservoir and to probe the magnitude of its non-thermal motions. Available far-infrared observations can be used in tandem with the observed ammonia emission to estimate the total gas mass contained in G035.39–00.33.

Results. We identify a main velocity component as a prominent filament, manifested as an ammonia emission intensity ridge spanning more than 6 pc, consistent with the previous studies on the Northern part of the cloud. A number of additional line-of-sight components are found, and a large-scale linear velocity gradient of ~0.2 km s^{-1} pc^{-1} is found along the ridge of the IRDC. In contrast to the dust temperature map, an ammonia-derived kinetic temperature map, presented for the entirety of the cloud, reveals local temperature enhancements towards the massive protostellar cores. We show that without properly accounting for the line of sight contamination, the dust temperature is 2-3 K larger than the gas temperature measured with NH_3.

Conclusions. While both the large-scale kinematics and temperature structure are consistent with that of starless dark filaments, the kinetic gas temperature profile on smaller scales is suggestive of tracing the heating mechanism coincident with the locations of massive protostellar cores.

2.2 Introduction

Massive ($M_\star > 8\ M_\odot$) stars dominate their environments through powerful stellar winds, ionizing radiation, and their decisive role in driving the turbulence and enriching the chemical complexity of the interstellar medium. Despite the importance massive stars play in their host galaxies, understanding the earliest phases of their formation is still an ongoing effort (e.g., Tan et al. 2014, for a review of the subject).

The majority of massive stars are not formed in isolation. A large fraction of all stars are born within giant molecular clouds (GMCs) (McKee & Ostriker 2007), massive ($> 10^4\ M_\odot$), often filamentary molecular structures that span dozens of parsecs and are thought to be responsible for the bulk of Galactic star formation. GMCs have been found to be highly sub-structured, and with the advance of mid- and far-infrared imaging instruments, the ubiquity of filamentary structure in star-forming molecular clouds became apparent (Molinari et al. 2010; André et al. 2010). As the filaments assemble their mass, the densest filaments in star-forming clouds are thought to become gravitationally unstable, fragmenting further into protostellar cores.

Often tracing the highest-density regions of GMCs (e.g., Schneider et al. 2015), infrared dark clouds (IRDCs) have been used as testing grounds for the earliest stages of massive star and cluster formation theories since the late 1990's. First identified as dark features obscuring the bright Galactic background (Perault et al. 1996; Egan et al. 1998), IRDCs soon became recognized as the most promising candidates for harboring the long-sought initial conditions of high-mass star forming regions (e.g., Rathborne et al. 2006). Subsequent far-infrared, submillimetre, and radio-band observations revealed a high degree of fragmentation in these clouds, with dense and massive cores exhibiting a variety of star formation stages: from prestellar, dark, cold, and quiescent cores to active, infrared-bright and chemically rich substructures with embedded sources driving outflows and H II regions (e.g., Beuther et al. 2005; Pillai et al. 2006; Chambers et al. 2009; Sanhueza et al. 2012; Wang et al. 2011, 2014).

G035.39–00.33 (hereafter G035.39) is a cold (15 – 17 K, Nguyen Luong et al. 2011), massive (~16700 $M_\odot$, Kainulainen & Tan 2013) IRDC located 2.9 kpc away in the W48 molecular complex (Simon et al. 2006b). Its highly filamentary structure appears as an extinction feature up to 70 μm, and the cloud harbors a number of dense cores (Butler & Tan 2012).

Previous single-dish radio and far-infrared studies of G035.39 describing the large, pc-scale gas reservoir suggest that the bulk of the cloud material in the IRDC represents the typical chemical properties of cold and dense gas, namely high CO depletion (Hernandez et al. 2011, 2012; Jiménez-Serra et al. 2014) and high values of deuteration (Barnes et al. 2016). Furthermore, the dust temperature maps in Nguyen Luong et al. (2011), derived from *Herschel* photometric maps, show a monotonic decrease in dust temperatures from the edges of the IRDC to its innermost regions, where most of the massive protostellar cores are, with no apparent heating signatures of the embedded protostars in G035.39.

Jiménez-Serra et al. (2010) observed a widespread, pc-scale SiO emission as a mixture of broad and narrow components, finding it consistent with being a remnant of a large-scale shock, possibly associated with the IRDC formation process. Follow up observations revealed that the northern part of the cloud possesses complex, multicomponent kinematics, with the velocity components interacting dynamically with the massive cores (Henshaw et al. 2013, 2014;

Jiménez-Serra et al. 2014). Alternatively, the origin of the SiO emission across the cloud could be attributed to outflow activities of undetected embedded protostars (Jiménez-Serra et al. 2010). Indeed, Nguyen Luong et al. (2011) find 70 μm *Herschel* sources in 13 massive dense cores (20-50 $M_\odot$, MDCs) in G035.39, which indicates that these cores are potentially forming high-mass stars (white diamonds on Figure 2.1). While the *Herschel* sources are likely to be responsible for the observed broad component SiO emission in G035.39, attributing its narrow component to embedded protostars would require the existence of an undetected population of low-mass protostars across the cloud.

By comparing the $C^{18}O$ line emission with the mass surface density map obtained from extinction mapping, Hernandez et al. (2012) concluded that the denser part of the cloud is consistent with being in virial equilibrium. Follow-up observations of G035.39 with the Plateau de Bure interferometer (PdBI) have resolved the kinematics of the cloud into distinct sub-virial, velocity coherent structures that hint at their dynamical interaction with an embedded protocluster (Henshaw et al. 2014, 2016a). The cores in the continuum substructure appear to be intertwined in a network of independent filamentary structures (Henshaw et al. 2017) and are likely to collapse without additional support from magnetic fields (Henshaw et al. 2016a, see also Tan et al. 2013).

Despite the wealth of observations collected for this IRDC, its gas temperature structure has never been mapped before. This paper intends to establish a coherent picture of the physical conditions of dense gas across the whole extent of the IRDC using observations of two ammonia inversion lines obtained with a high spectral resolution. Figure 2.1 shows the infrared extinction morphology of G035.39 and marks the portion of the cloud studied by Henshaw et al. (2013, 2014). The overall field of view of the Figure shows the extent of observations that are presented in this study. For comparison to the previous body of work, we refer to the region north of δ(J2000) = +2°08′45″, approximately corresponding to the extent of previous IRAM 30m and PdBI studies, as G035.39-N.

We discuss observations conducted and available data used in §2.3. Dust temperature, gas column density, cloud kinematics, and ammonia abundance are presented in §2.4. We compare the gas and dust temperatures, and discuss the stability of the cloud, in §2.5. We summarize our findings in §2.6.

2.3 Observations

2.3.1 GBT observations

Robert C. Byrd Green Bank Telescope (GBT) observations of G035.39 were carried out on 2010 Feb 27 and 28 (project GBT/10A-067, PI: Ke Wang). G035.39 was covered in Nyquist sampled on-the-fly (OTF) maps scanning along RA and Dec. The K-band receiver was equipped with two beams (B3 and B4) separated by 178.8 arcsec in azimuth. We used the frequency switching mode, with ±2.5 MHz switch for the two signal states, in a 12.5 MHz band with a channel width of 3.05 kHz in dual polarization mode. The band covered NH_3 (1,1) and (2,2) inversion lines, CCS (2-1) rotational transition, and NH_2D (4_{14}-4_{04}); the latter being undetected. The weather conditions at the GBT site were stable during the observing run, with pointing accuracy resulting

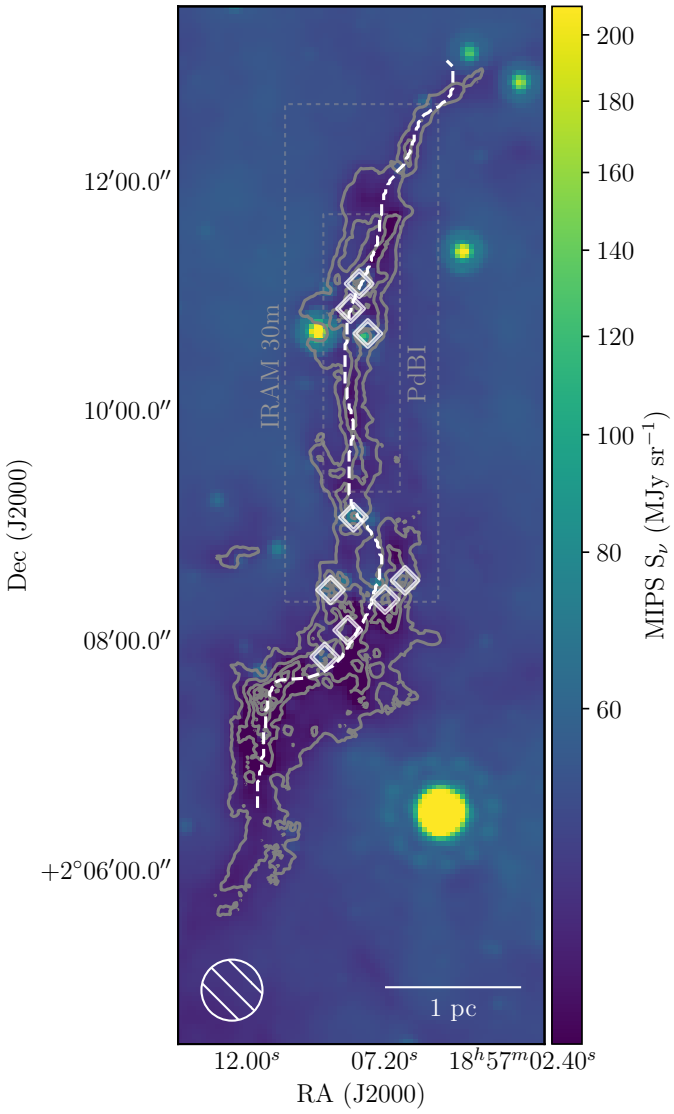

Figure 2.1 MIPS 24 μm emission overlaid with infrared extinction contours (Kainulainen & Tan 2013) starting from A_V = 25 mag and progressing inwards in steps of 20 mag. Massive dense *Herschel* cores from Nguyen Luong et al. (2011) are marked with white diamonds. The white dashed line indicates the peak intensity ridge of NH_3 (1, 1) emission (see §2.3.1). The dashed gray rectangles illustrate the extent of IRAM 30m (outer box) and PdBI (inner box) N_2H^+ maps (Henshaw et al. 2013, 2014), while the extent of the whole figure corresponds to the area mapped with the GBT.

from winds alone estimated to be below 3″. The system temperatures were at 38-45 K during the first day and between 58 and 78 K during the second day.

To estimate the absolute flux of the observed emission, we performed nodding observations of the quasar 3C48. For each beam, polarization, and spectral window states, the data were then reduced in GBTIDL v2.10.1 to yield main beam temperatures for each state. Using a spectral flux density model from Ott et al. (1994), we derived the predicted flux for 3C48. When compared to reduced nodding observations, the model is consistent within 10% for ammonia spectral windows. The off-source beam B4, however, was found to be mismatched by 50-90% in integrated intensity when compared to the on-source beam, and was consequently removed from the following discussion. As the area mapped by B4 was mainly off the bulk of G035.39, the decision to drop the beam from a subsequent discussion does not affect the results of this study.

The OTF observations of G035.39 were calibrated via the GBT pipeline[1] (Masters et al. 2011) into main beam temperature units and imaged with the GBT Ammonia Survey (GAS, Friesen, Pineda et al. 2017) pipeline[2], modified to address spectral setup differences. The full width at half maximum of the GBT beam at NH_3 (1,1) line frequency (32″) was used to set the pixel size for all spectral line cubes, at three pixels per beam. The final spectral resolution of the data is 38.6 m s^{-1}.

2.3.2 Herschel public data

As mentioned in §2.2, the entire extent of G035.39 has been studied before with the *Herschel* Space Observatory (Pilbratt et al. 2010) by Nguyen Luong et al. (2011). To quantify the difference in gas- and dust-derived properties, we use the available G035.39 data from the *Herschel* infrared Galactic Plane Survey (Hi-GAL, Molinari et al. 2010).

The data products used in this study, photometric maps from PACS (Poglitsch et al. 2010) and SPIRE (Griffin et al. 2010) cameras, were downloaded from the image server of the first public Hi-GAL data release (DR1, Molinari et al. 2016), observation IDs 1342219631 and 1342219630. The DR1 data underwent processing by the ROMAGAL pipeline (Traficante et al. 2011), and in particular, had its absolute levels of emission calibrated. This allows us to directly put constraints on the properties of dust emission.

2.4 Results

2.4.1 Overview of the data

The integrated intensity maps for ammonia and CCS transitions observed with the GBT are presented in Figure 2.2. Not accounting for the bright NH_3 satellite lines, the majority of the molecular emission detected from the cloud is situated between 43 and 46 km s^{-1}. A prominent secondary component is present in the southern region of the cloud and, furthermore, strong

[1] http://gbt-pipeline.readthedocs.io/en/latest/
[2] http://gas.readthedocs.io/en/latest/

line asymmetries indicate the presence of additional line-of-sight components (see Figure 2.3 for example spectra).

Given the low signal-to-noise ratio of the CCS (2-1) line, its kinematics cannot be easily constrained, and the transition is not discussed throughout this work. We note that the southern peak of the integrated intensity of the CCS coincides with a peak of the mid-infrared extinction map (Figure 2.2c), and has no associated 24- and 70 μm point sources. As the carbon-chain molecules are known to trace regions of early-stage chemistry (Suzuki et al. 1992), the CCS peak may be indicative of dense gas in an earlier evolutionary stage than the rest of the cores in the IRDC. More dedicated studies will be carried out toward this region in the future.

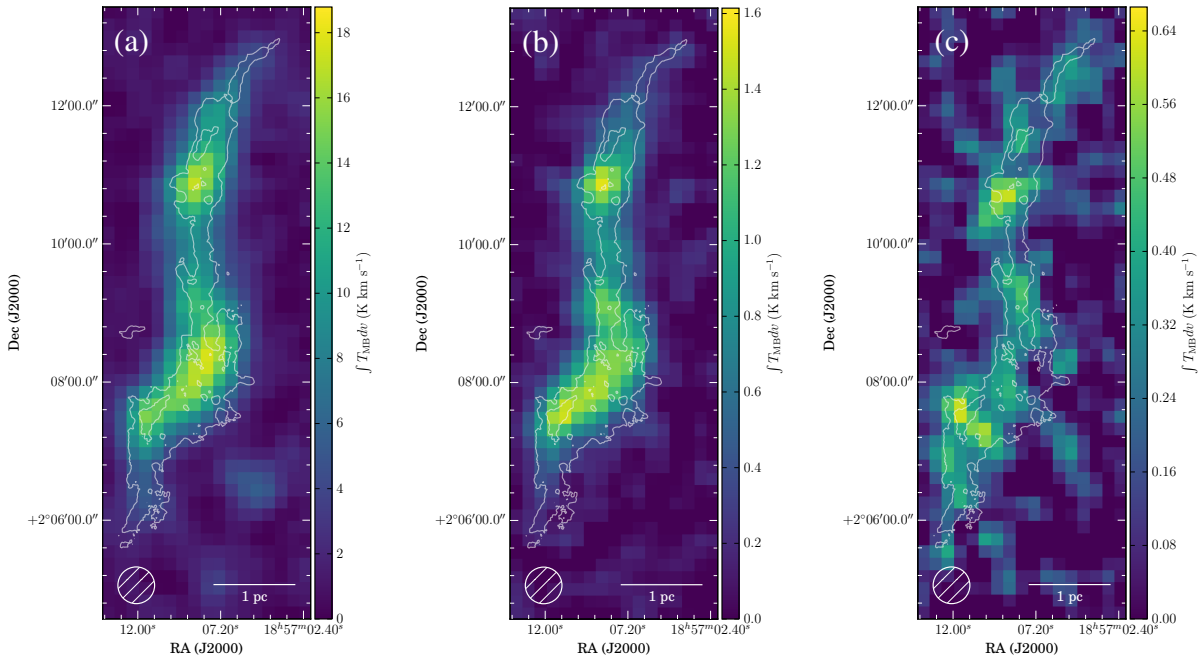

Figure 2.2 Data products from GBT observations of G035.39. Integrated intensities of NH_3 inversion transitions (1, 1) and (2, 2), *(a)* and *(b)*, respectively; and integrated intensity of the rotational CCS (2-1) line *(c)*. NH_3 (2, 2) and CCS lines were integrated between 43 and 47 km s^{-1} to highlight the emission features, while the NH_3 (1, 1) line was integrated between 20 and 70 km s^{-1}. Extinction contours from Kainulainen & Tan (2013) at A_V = 25 and 65 mag are shown in white.

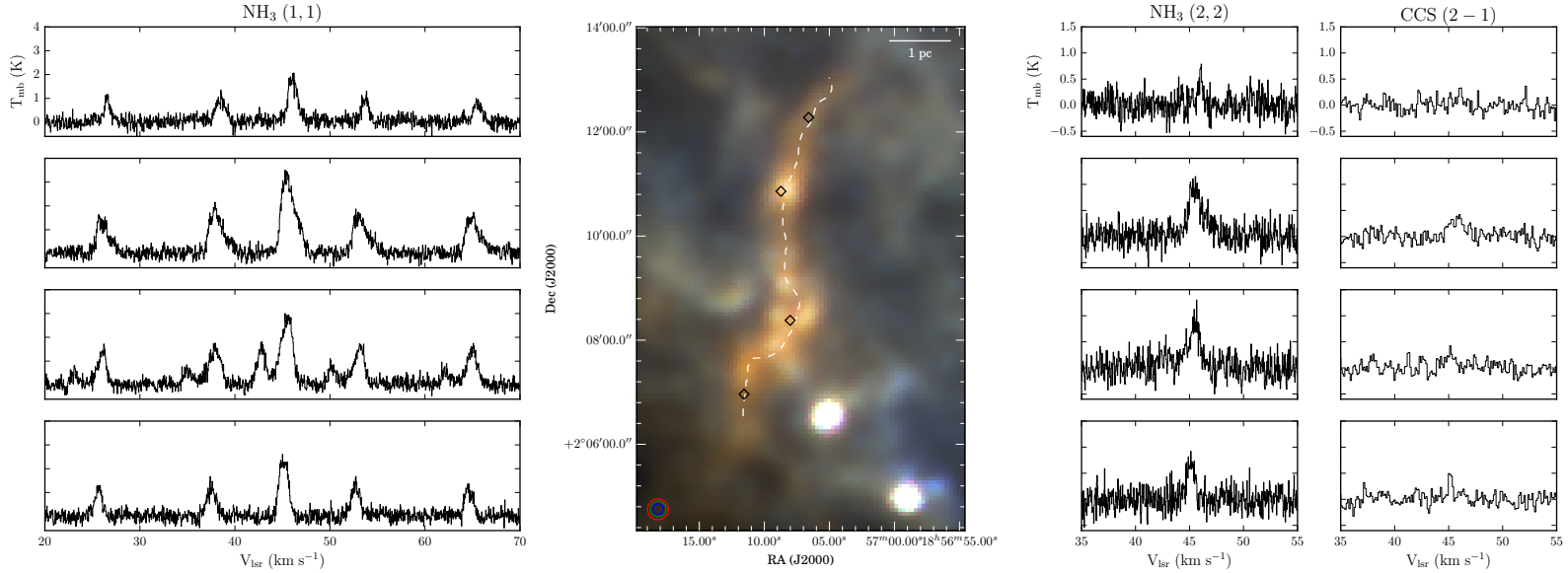

Figure 2.3 A composite Hi-GAL color image of the infrared dark cloud. Red, green, and blue channels correspond to 350, 250, and 160 μm, respectively. To the left of the *Herschel* map, four NH_3 (1, 1) spectra are shown, and four selected NH_3 (2, 2) and CCS (2-1) lines are displayed on the right side of the central figure. The CCS spectra are smoothed to 0.12 km s^{-1}. Each row of spectra is arranged to match the black diamond markers shown on the FIR map, selected to represent typical spectra along the filament. The filament ridge, as defined in §2.3.1, is marked with a dashed white line.

As the large-scale structure of the cloud's main velocity component manifests itself as a prominent, continuous filament, we can probe how its physical properties vary along its length. We set the line segment defining the filament from the ammonia intensity profile. The maximal value of the NH_3 (1,1) integrated intensity along right ascension is calculated for each value of declination. The longest continuous segment is then taken from the obtained set of coordinate points, with a continuity condition that the neighboring points must be in the same GBT beam. This approach, adequately simplistic for our task of probing pc-scale structure, recovers the intensity ridge of G035.39 without the need to resort to more sophisticated ridge-detection methods. The resulting filament profile is marked on Figure 2.1.

In the far-infrared *Herschel* photometric maps, G035.39 manifests itself as a typical infrared dark cloud, characterized by its emission at longer wavelengths. It appears as an extinction feature in the 70 μm band of PACS, and as an emission feature from 160 μm onwards. The central panel on Figure 2.3 displays a color-composite image of the IRDC, with 350, 250, and 160 μm emission used for red, green, and blue channels, respectively. As both ammonia and dust continuum trace the dense gas that constitutes the bulk of the cloud, the far-infrared morphology does not show any significant deviations from the NH_3-defined filament ridge. A clearly visible substructure in PACS 160 μm and SPIRE 250 μm maps can be attributed to those *Herschel* bands having angular resolutions (12″ and 18″, respectively) different from our NH_3 observations (32″). The properties derived from the *Herschel* maps were then regridded onto the grid given by our GBT observations.

2.4.2 Ammonia line fitting

The ammonia molecule has been proven to be an invaluable tool in probing physical conditions of moderately dense molecular regions (e.g., Myers & Benson 1983; Rosolowsky et al. 2008a; Pillai et al. 2006; Pineda et al. 2010a; Wang et al. 2012, 2014), and the ratio of its collisionally populated metastable $(J, K) = (1, 1)$ and $(2, 2)$ inversion states can be used to derive the rotational gas temperature $T_{\rm rot}$ (Ho & Townes 1983). This temperature is commonly used as a proxy value for the kinetic temperature of the medium, derived through balancing the rates of radiative and collisional transitions (Walmsley & Ungerechts 1983; Tafalla et al. 2004; Swift et al. 2005).

In the Rayleigh-Jeans approximation, an observed spectral profile of the two inversion lines along with their hyperfine components can be described as a sum over their hyperfines, assuming uniform excitation conditions for all the hyperfine components of the lines and a unity beam filling factor (e.g., Stahler & Palla 2005):

$$T_{\rm MB}(v) = \sum_i \left\{ 1 - \exp\left[-r_i\, \tau_0\ \exp\left(-\frac{(v_{\rm off} - v_i)^2}{2\sigma_v^2}\right)\right]\right\} (T_{\rm ex} - T_{\rm bg}), \tag{2.1}$$

where $T_{\rm ex}$ describes the population ratios of the inversion transition parity levels, the background radiation temperature $T_{\rm bg}$ is taken to be that of the cosmic microwave background (2.7312 K), r_i are normalized relative intensities of the hyperfine components, v_i is the velocity centroids of the hyperfine components, σ_v is the velocity dispersion, and τ_0 the main group opacity of the corresponding inversion line. The latter can be used to derive the column density of the (1,1)

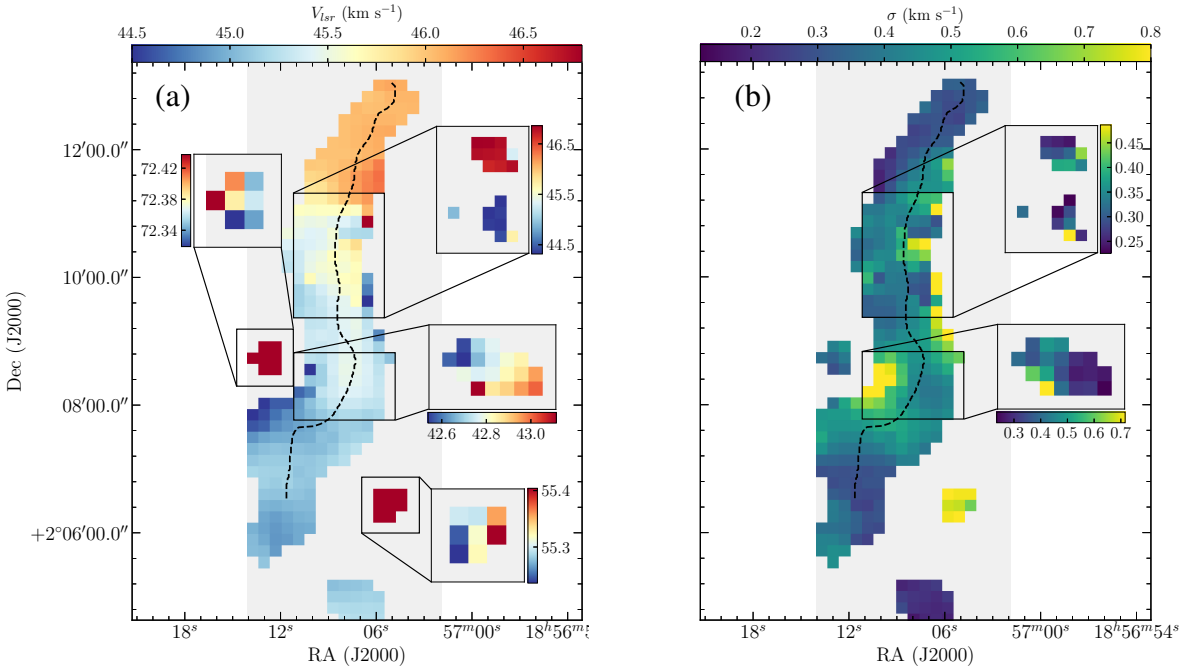

Figure 2.4 a) Fitted velocities relative to line rest frequency. Overlaid on the main velocity component, additional components, enclosed in the black contours, are shown in the cut-outs. The ridge of G035.39, as defined in §2.3.1, is marked as a dashed black line. b) Same as (a), but for the fitted velocity dispersions.

rotational state $N_{(1,1)}$ (Rosolowsky et al. 2008a):

$$N(1,1) = \frac{8\pi k \nu_0^2}{hc^3} \frac{1}{A_{1,1}} \sqrt{2\pi}\sigma_\nu (T_{\rm ex} - T_{\rm bg})\tau_0, \tag{2.2}$$

and can then be scaled to a total ammonia column density $N_{\rm tot}$ via a partition function, assuming that only the metastable population levels are populated (Rosolowsky et al. 2008a). The spectral profile modelling and line fitting are done following the method presented in Friesen, Pineda et al. (2017), where the NH_3 (1,1) and (2,2) spectra are simultaneously modelled using Eq. 2.1 within the `pyspeckit` (Ginsburg & Mirocha 2011) Python package. The spectral profile of both inversion lines are fitted considering the following free parameters: kinetic temperature $T_{\rm kin}$, excitation temperature $T_{\rm ex}$, ammonia column density $N_{\rm tot}$, velocity offset with respect to line rest frequency $v_{\rm off}$, and velocity dispersion σ.

As mentioned in §2.4.1, multiple line-of-sight components are present in the ammonia spectra. Their interchangeable strength and unknown a priori locations make conventional line-fitting techniques difficult to apply. In particular, the iterative nonlinear least-squares algorithm (Levenberg 1944; Marquardt 1963) used in `pyspeckit` is prone to failures to reach global convergence in the presence of multiple local minima. To ensure convergence of the algorithm on the global minima, we perform parameter space gridding to select initial guesses for the fitting routine. As the parameters that vary the most among our spectra are the line centroids and their peak amplitudes, we search for the optimal starting conditions by varying $T_{\rm ex}$ and $v_{\rm off}$.

By inspecting the NH_3 (1,1) spectra for line peaks and line asymmetries, we have set the velocity intervals at which the line centroids could reside. The six intervals selected are centered at 42.9, 44.6, 45.5, 47.0, 55.2, and 72.2 km s^{-1}. The velocity components that were found to overlap spatially were each split into ten values, corresponding to velocity steps of ≤ 0.1 km s^{-1}. Additionally, we consider a range of 10 $T_{\rm ex}$ values set up to cover the amplitude range of our NH_3 (1, 1) data. The resulting velocity and line brightness ranges for component pairs that were found to overlap were then permuted together to yield over 50k modeled spectra. Each modeled spectral profile was subsequently checked against all the pixels in our data, and the models with the lowest total squared residuals were used as a starting point for the nonlinear least squares routine. The source code for the initial guess selection method described above is freely available online[3].

For every pixel of the spectral cube obtained from §2.3.1, we perform a multiple component nonlinear least-squares fit for one and two velocity components. To decide on a number of components present in a spectrum, one needs to rule out overfitting. As a direct minimization of the square of residuals would always prefer a more complex model, we limit the multiple component fits, requiring the best-fit solution to have a signal-to-noise ratio of at least three in all components and for those components to have a peak separation larger than the line widths of the two components. Should any of these criteria not be met, a simpler model is preferred - one velocity component for a failed double peak fit, or a spectrum is masked altogether if a single peak fit fails.

[3] https://github.com/vlas-sokolov/multicube

2.4.3 Parsec-scale kinematics of the IRDC

The structure of G035.39 can be seen as a combination of a main velocity component and additional velocity components along the line of sight. We refer to the coherent structure at 44-47 km s^{-1} as the main velocity component. For spectra with two identified line components, components that are brighter than their counterparts are considered to belong to the main group. In G035.39, this choice results in a spatially coherent velocity field traced by the main component.

Figure 2.4 illustrates the kinematics of the main velocity component, overlaid with additional identified velocity components. Of these additional components, the ones found in G035.39-N (the 44 and 46 km s^{-1} components) coincide with the network of filaments from Henshaw et al. (2014). Two more velocity components are identified in both ammonia transitions from the spectral cube inspection, but at 55 km s^{-1} and 72 km s^{-1} are unlikely to be related to the main body of the IRDC. Additionally, a strong (up to peak $T_{\rm MB}$ = 1.5 K) velocity component, well-separated from the main cloud component by ∼2 km s^{-1}, is present at the location of the active star formation in the southern part of the IRDC. This is consistent with the location and $v_{\rm lsr}$ of Filament 1 from Jiménez-Serra et al. (2014) at its southernmost point.

The velocity of the main ammonia component gradually changes from red- to blue-shifted in the southward direction. Figure 2.5 illustrates this change, showing the velocity centroid and velocity dispersion profiles along the IRDC intensity ridge. The non-thermal velocity dispersions of ammonia (Myers 1983) have a large dynamic range, sometimes going as high as 1.2 km s^{-1} at the edges of the map, but generally staying within the interquartile range between 0.38 and 0.52 km s^{-1} (Figure 2.5b). These high values, implying non-thermal motions dominating the line width, are above those found in low-mass cores and are in the upper range of typical non-thermal components of massive cores (Caselli & Myers 1995). For the H_2 sound speed derived from the fitted ammonia kinetic temperatures and assuming a mean mass per particle of 2.33 u, the average Mach number across the IRDC is $\mathcal{M}$ = 2.14, consistent with previous studies of G035.39 that find gas motions in the cloud to be supersonic (Henshaw et al. 2014; Jiménez-Serra et al. 2014).

The gradual change of the line centroid towards the southern portion of the IRDC can be quantified in terms of a velocity gradient. Previous studies of G035.39 have discussed the global gas motions on various scales. Henshaw et al. (2014) attribute radial velocity irregularity towards the northern part of G035.39-N found by Henshaw et al. (2013) to the unresolved substructure, and find the global gradients in identified filaments to be smaller than 0.7 km s^{-1} pc^{-1}. Jiménez-Serra et al. (2014) find global, north-south velocity gradients of ∼0.4 – 0.8 km s^{-1} pc^{-1} along three CO filaments in G035.39. As our GBT data covers the full extent of the cloud, we are able to constrain the global velocity gradient along the whole IRDC. A least squares fit to the ridge velocity profile, weighted by uncertainties in centroid velocities, results in a line-of-sight velocity gradient of $\nabla v \sim 0.2$ km s^{-1} pc^{-1} along the filament's 6 pc length (Figure 2.5a). This value is in good agreement with the average velocity gradients reported for larger-scale filament and GMC structures (e.g., Hernandez & Tan 2015; Wang et al. 2016).

While the global velocity gradient following the ridge of G035.39 is well described on scales larger than one parsec, smaller-scale, oscillatory-like deviations from the fitted linear relation are present. Additionally, hints of a localized third component towards the southern 42.6 km s^{-1}

feature are manifested as a broader velocity dispersion at the edge of G035.39 (see Figure 2.6 for an example fit with irregular residual); as it is mostly blended with the main component, constraining its properties is difficult due to the limited angular resolution of the GBT data. Ammonia emission is often highly substructured in star-forming regions, and can manifest itself as filamentary emission down to ~5000 AU scales (Pineda et al. 2011a, 2015). The exact nature of the velocity substructure in the southern part of G035.39 can be seen as either stemming from the coherent gas motions around the dense cores (e.g., Hacar & Tafalla 2011; Zhang et al. 2015; Gritschneder et al. 2017), or as a picture reminiscent of the nearby low-mass star forming Taurus complex, where previously unresolved velocity-coherent filaments are found to be bundled together in a larger structure (Hacar et al. 2013; Tafalla & Hacar 2015). The velocity irregularities along the cloud may result from the sub-pc substructure emission (similar to the already resolved one in the G035.39-N region by Henshaw et al. (2014)), being smoothed by the GBT beam. The higher angular resolution analysis of the gas kinematics along the entire IRDC will be addressed in a future study.

2.4.4 Gas temperature

While the profile of the NH_3 (1, 1) line can be constrained accurately in the pixels with significant emission, the (2, 2) line is considerably weaker in the low-temperature regime. Because of this, we impose a more stringent constraint on the physical parameters that depend primarily on the (2, 2) inversion transition - namely, kinetic temperature and total ammonia column density. For these, we only select spectra that have $> 3\sigma_I$ detection in the integrated intensity. We take the expression for integrated intensity uncertainty, $\sigma_I = \sqrt{N}\sigma_{T_{\rm MB}}\Delta v_c$, from Mangum & Shirley (2015), where N is the number of channels with nonzero emission in a modeled spectrum (arbitrarily taken to be 10^{-5} K), $\sigma_{T_{\rm MB}}$ is the corresponding $T_{\rm MB}$ uncertainty, and Δv_c is the channel width in the GBT spectra.

The gas kinetic temperature of the main component of G035.39 is presented in Figure 2.7. The derived values vary across the body of the dark cloud from about 11 K to 15 K. The cold gas temperature range is typical of other IRDCs (Pillai et al. 2006; Ragan et al. 2012; Chira et al. 2013; Wang et al. 2012, 2014) as well as of relatively nearby low-mass starless cores (Rosolowsky et al. 2008a; Friesen et al. 2009; Forbrich et al. 2014).

Due to a more stringent masking of the temperatures derived from our multi-component fit, only a handful of spectra have their kinetic temperature constrained for weaker secondary components. As most of the derived values of the gas kinetic temperature belong to the main component, the discussion on the temperature of the weaker components is thus effectively restricted to those few detections. In the star-forming part of G035.39-N, towards the northern group of the star-forming cores, we successfully measure the gas temperature for two components along the line of sight to be between 12.9 and 13.3 K.

The region coincident with a bright infrared source south-east of the main filament (55 km s^{-1} cut-out on Figure 2.4) is consistently hotter than the bulk of the IRDC. The derived temperatures for the gas associated with the source range from 17.5 to 20.9 K, suggesting that the gas is internally heated. Nguyen Luong et al. (2011) identify the source as an infrared-bright protostellar MDC, and derive its dust temperature to be 26 ± 6 K. As the ammonia emission for this com-

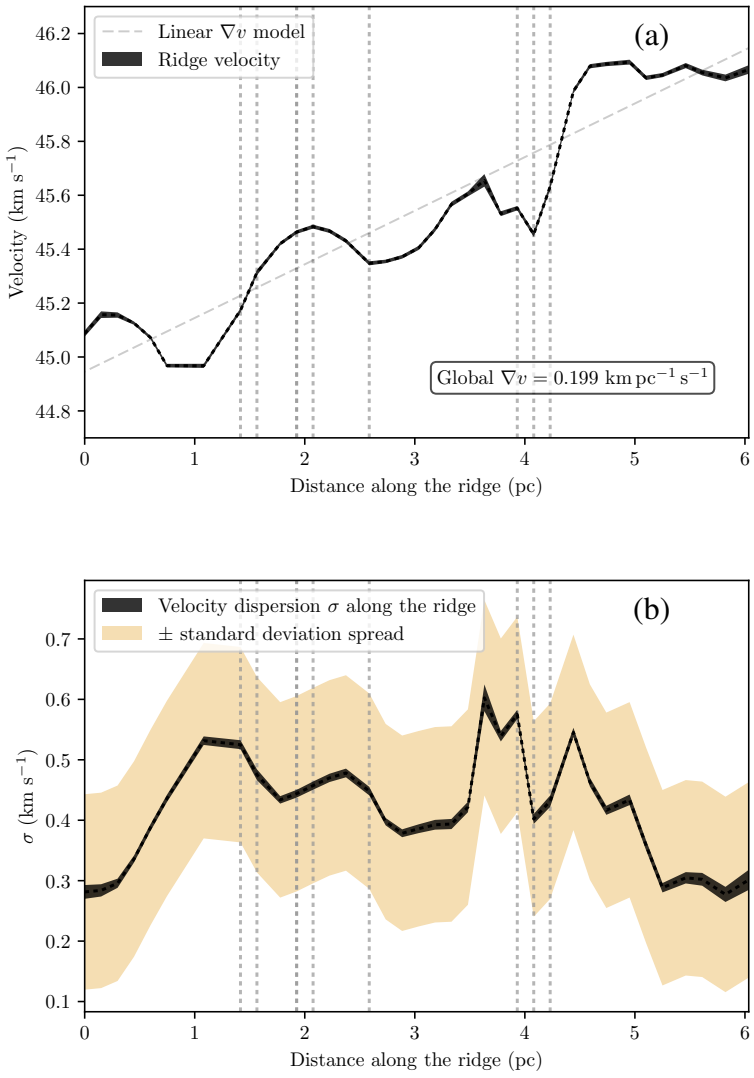

Figure 2.5 (a): The radial velocity profile of the main component along the G035.39 filament, starting at its southernmost point. The solid black line shows the radial velocities fit at the intensity ridge of the IRDC. The width of the solid black line represents the fitting uncertainty at each point. The vertical dotted lines mark the projected locations of the massive protostellar cores from Nguyen Luong et al. (2011). (b): Same as (a), but for the velocity dispersion profile along the IRDC ridge. The yellow shaded region denotes the spread area given by two standard deviations of all σ values in the main velocity component.

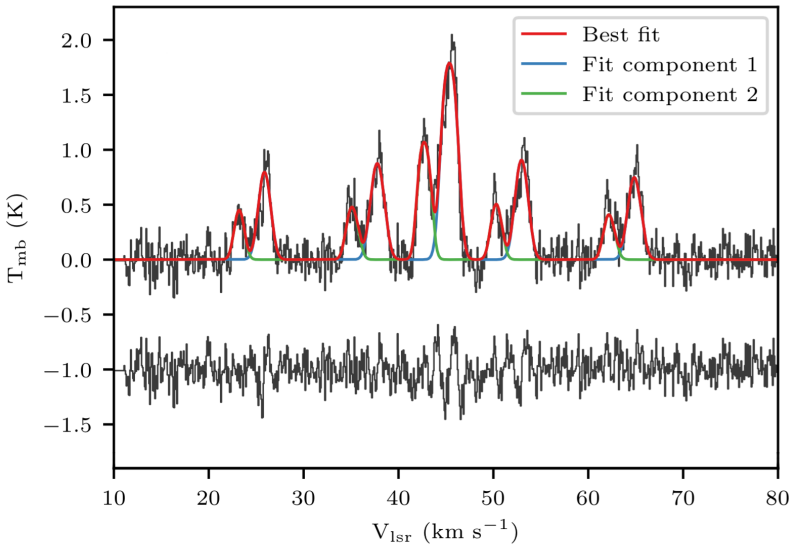

Figure 2.6 NH_3 (1,1) spectrum towards α(J2000) = 18h57m10.1s and δ(J2000) = +2°08′23″, overlaid with the best two-component fit model. A significant residual, revealing the presence of the unconstrained third component, is plotted alongside the spectrum, offset by 1 K. The spectrum was smoothed to 0.08 km s^{-1} for visual clarity.

ponent is peaked at 55 km s^{-1}, it appears to be physically unrelated to G035.39. Similarly, for a spectral line detected at 72 km s^{-1} (Figure 2.4), which appears as a starless infrared extinction feature east of the filament, we report a kinetic temperature of 16.5 ± 1.3 K. Although defined as part of the IRDC extent in Nguyen Luong et al. (2011) based on the common column density contour, we suggest that the feature does not form a coherent structure with G035.39.

2.4.5 Dust temperature

The intensity of an optically thin source of temperature T is given by the radiative transfer equation (e.g., Rybicki & Lightman 1979), which can be approximated by

$$I_\nu = B_\nu(T) \times (1 - e^{-\tau_\nu}) \approx B_\nu(T)\tau_\nu, \tag{2.3}$$

where $B_\nu(T)$ is the Planck blackbody function. In the expression above, a frequency dependent opacity τ_ν can be shown to be related to the gas column density N_{H_2} in the following way:

$$\tau_\nu = \int \kappa_\nu \rho \mathrm{d}s = N_{H_2} \mu_{H_2} m_H \kappa_\nu, \tag{2.4}$$

where $\mu_{H_2} = 2.8$ is the molecular weight per hydrogen molecule (Kauffmann et al. 2008), κ_ν is the dust opacity, and m_H is the mass of a hydrogen atom. For consistency with Nguyen Luong et al. (2011), we have adopted the dust opacity law of $\kappa_\nu \propto \nu^\beta$, assuming a gas-to-dust mass ratio of 100 from Hildebrand (1983). As the optically thin approximation in Eq. 2.3 does not necessarily

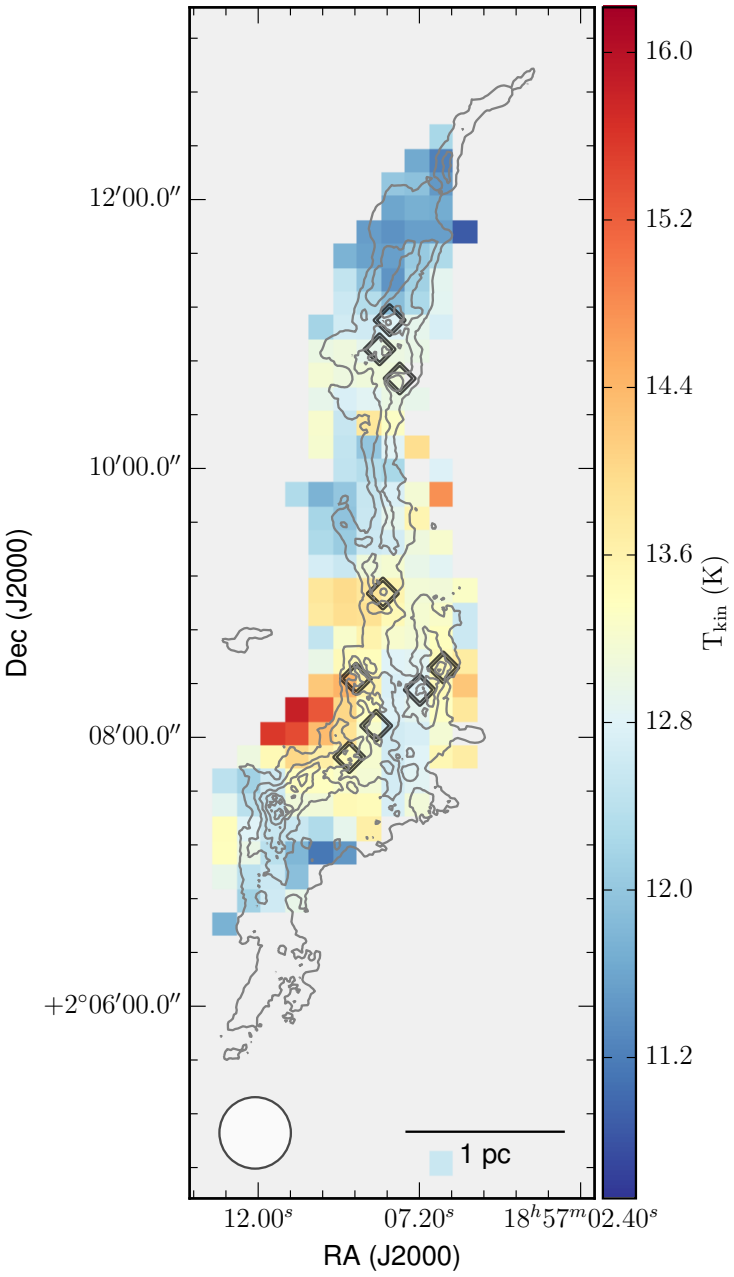

Figure 2.7 Kinetic temperature map derived from the main velocity component of NH_3. The contour lines and diamond markers are the same as on Figure 2.1.

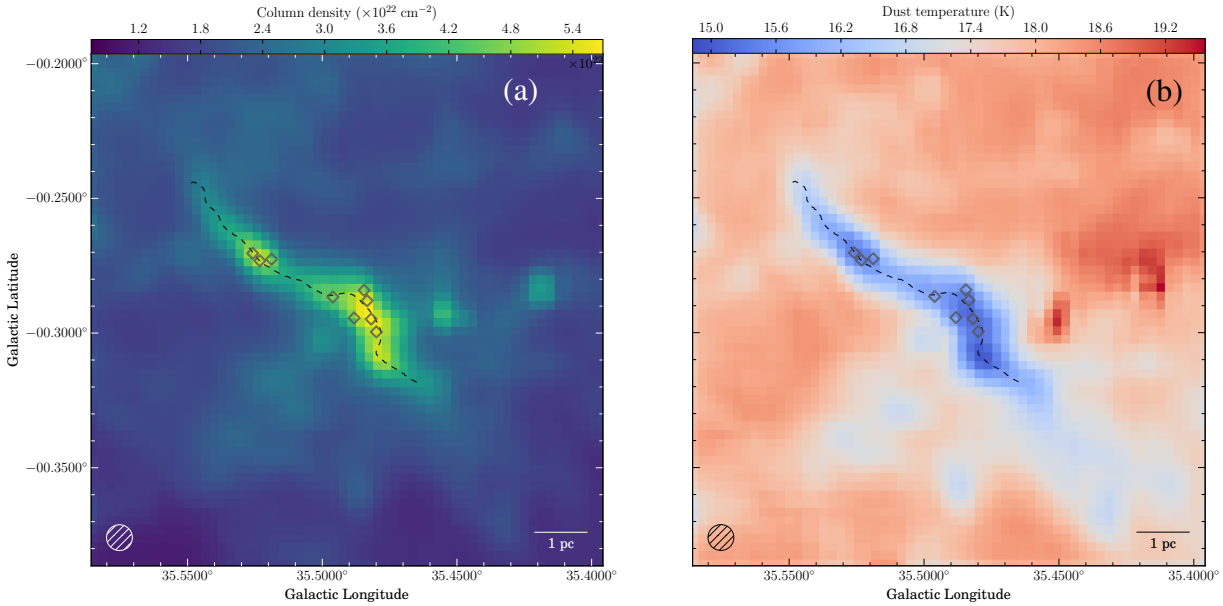

Figure 2.8 H_2 column density (a) and dust temperature (b) maps derived from *Herschel* data for G035.39. A 1 pc length scale and a combined *Herschel* beam size are shown for each map. The ammonia intensity ridge and the positions of *Herschel* MDCs are shown as a black dashed line and gray diamond markers, respectively.

hold for PACS bands at high column densities, we discuss its limitations for the PACS data. While the 160 μm PACS band is expected to be within the optically thin approximation well into the high density regime ($\tau_{160} = 0.16$ for $N_{H_2} = 10^{23}$ cm^{-2}), the 70 μm maps may trace extinction of dust rather than its emission (G035.39 appears as an extinction feature in 70 μm), rendering the optically thin dust emission assumption invalid (e.g., Battersby et al. 2011).

Hi-GAL PACS and SPIRE maps containing G035.39 were jointly convolved to a common resolution of 34.5″, corresponding to the beam size of the 500 μm SPIRE band. The maps were then regridded to 11.5″ pixel size to form spectral cubes. The resulting cube was fit pixel-by-pixel with a single temperature gray-body model described above, assuming a fixed value of $\beta = 2$ (e.g., Stutz et al. 2010; Nguyen Luong et al. 2011; Elia et al. 2013; Lombardi et al. 2014). Fixing the value of β reduces the number of free parameters for an otherwise degenerate model (e.g., Planck Collaboration et al. 2011; Kelly et al. 2012). While implicit assumptions on the spectral opacity index are made in such a way, it enables an estimation of the resulting parameter uncertainties by minimizing the errors stemming from the model degeneracy. In the above analysis, we have considered 30% uncertainty on the flux levels for consistency with Nguyen Luong et al. (2011).

Column density and effective dust temperature maps, derived for the *Herschel* regions from 160, 250, 350 and 500 μm *Herschel* bands, are presented in Figure 2.8. The column density and dust temperature values show anti-correlation, typical for externally irradiated clouds (Evans et al. 2001; see also Planck Collaboration et al. 2011), and IRDCs (e.g., Wang et al. 2015,

Appendix). The overall morphology of the density and temperature structure in the derived parameter maps is similar to that of Nguyen Luong et al. (2011).

2.4.6 Molecular abundances

The column densities from *Herschel* and those of ammonia correlate weakly ($r = 0.64$, Figure 2.9), and show no evidence for ammonia depletion, consistent with previous work toward nearby starless cores (Tafalla et al. 2002). By taking the ratio of the two we derive the ammonia abundance in G035.39, $X(NH_3) = [N(NH_3)/N(H_2)]$. The mean value of the total NH_3 abundance is $\sim 2.1 \times 10^{-8}$, corresponding to the para-NH_3 abundances of $\sim 1.0 \times 10^{-8}$ assuming the ortho- to para-NH_3 ratio of one. The range of abundances is comparable to that found towards the centers of low-mass cores (Tafalla et al. 2004; Crapsi et al. 2007; Friesen, Pineda et al. 2017), and is in good agreement with values measured towards the low-mass star-forming cluster Serpens South (Friesen et al. 2016). When compared to other IRDCs, our GBT data on G035.39 point to lower abundances - Ragan et al. (2011) derive NH_3 abundances of a few times 10^{-7}. However, Ragan et al. observe their IRDC sample with much smaller, VLA, and beam size, therefore allowing for a small beam filling factor of our observations may mitigate the discrepancy. Indeed, for an angular resolution of $40''$ and a median sample distance of 2.9 kpc, Pillai et al. (2006) report $X(NH_3)$ as being between 7×10^{-9} and 10^{-7}, consistent with our findings.

2.5 Discussion

2.5.1 A comparison of dust and gas temperatures

Current understanding of heating and cooling processes within dense molecular clouds requires close coupling between gas and dust at number densities above $\sim 10^5$ cm^{-3} (Goldsmith 2001). However, no correlation of dust and gas temperatures is found in G035.39 (Pearson's $r = -0.16$), despite the uncertainties on the temperatures being significantly smaller than the temperature dynamical range. Moreover, the dust temperatures derived from *Herschel* are consistently higher than the ammonia-based gas temperatures, suggesting that the two sets of observations are sensitive to different environments. Dust temperatures higher than the gas temperatures have previously been reported. Forbrich et al. (2014) find dust temperatures to be $2 - 3$ K warmer than the gas temperatures towards starless cores in the Pipe nebula. More recently, Friesen et al. (2016) report their ammonia-derived kinetic gas temperatures to be consistently lower than their *Herschel* counterparts. The difference in the two temperature tracers can be attributed to the line-of-sight mixing of warm foreground dust emission into the far-infrared SED, thus raising the effective line-of-sight average dust temperature. Ammonia gas temperature, on the other hand, is expected to trace the dense inner region of the filament only.

While the *Herschel* dust temperature map does not show any signs of local enhancements in the vicinity of dense cores, our NH_3 results point to local temperature increases of about 1 K toward the sites of active star formation. The magnitude of the effect is comparable to what Foster et al. (2009) find towards Perseus, where protostellar cores have been found to have

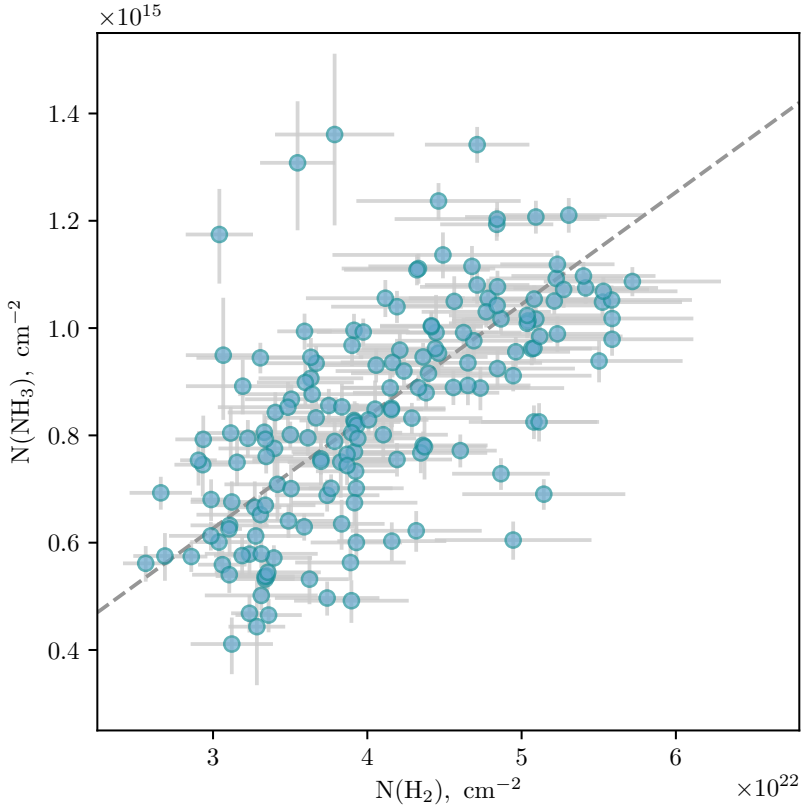

Figure 2.9 *Herschel*-derived H_2 gas column density plotted against fitted NH_3 column density. The dashed straight line passes through both the mean ammonia abundance in the IRDC and through the zero column density point.

ammonia-derived kinetic temperatures 1.3 K larger than the starless cores. To further investigate the possibility of dense gas heated by embedded protostars, we split the pixels into two groups: those within one GBT beam from the massive dense cores in Nguyen Luong et al. (2011) and those outside of it. A number of cores with masses lower than 20 $M_\odot$ were identified by Nguyen Luong et al. (2011) in addition to MDCs. As the total luminosity output of those cores is, on average, half of that of the MDCs, we restrict the spatial temperature distribution analysis to distance from the MDCs only. We find the median values of the gas kinetic temperatures to be 13.1 K inside the one beam radii, and 12.5 K outside of them. On the contrary, the median dust temperature increases from 15.9 to more than 18 K away from the massive dense cores (Figure 2.8). In order to visualize the opposite trends in gas and dust temperatures, we plot their kernel density estimations as a function of distance to the closest massive *Herschel* core (Figure 2.10a). The contours in Figure 2.10 represent the levels of the density function based on the scatter of the temperature points only, as the fitting uncertainties in both ammonia- and dust-based temperatures are much smaller than the dynamic range of the trends in the Figure.

The mean temperature errors and their standard deviations are $\sigma_{T_{kin}} = 0.38 \pm 0.15$ K and $\sigma_{T_{dust}} = 0.36 \pm 0.09$ K for gas and *Herschel* dust temperatures, respectively.

Systematically different values of dust and gas temperatures stress the importance of considering the line of sight mixing of the IRDC component with the warm dust emission. A number of methods for estimating the background component in *Herschel* photometric data are available (e.g., Wang et al. 2015)[4]. To address the line of sight contamination effects on the dust temperatures, we model the line of sight contamination of dust emission via two approaches:

- A Galactic Gaussian method (GG, Battersby et al. 2011), assuming that the Galactic contribution follows a Gaussian profile along the latitude direction within -1 deg $\leq b \leq +1$ deg latitude interval;

- A Small Median Filter method (SMF), which interpolates the background contribution from the region outside a predefined IRDC boundary (Simon et al. 2006b; Butler & Tan 2009) and estimates the 160 to 500 μm foreground by utilizing the SED model of diffuse ISM (Draine & Li 2007) normalized to the available 24 μm extinction data (Lim & Tan 2014; Lim et al. 2015).

A detailed description of each method is presented in Lim et al. (2016). The GG- and SMF-processed *Herschel* maps were used to derive the corrected column density and dust temperature maps following Section 2.4.5.

We find that both subtraction methods result in lower dust temperatures in G035.39, with the average values for the GG and SMF dust temperatures being 12.4 ± 1.0 and 13.8 ± 0.9 K, respectively. These values, compared to the mean gas kinetic temperature $T_{kin} = 12.9 \pm 0.8$ K, suggest that the corrections applied to the *Herschel* maps shifted the peak of the dust SEDs into the temperature regime that much better reflects the actual gas temperature. Figure 2.10b shows the same distance-temperature relation as Figure 2.10a, but for the GG method, a method that matches the ammonia temperature trend the closest. Despite the two trends showing some degree of agreement, no significant correlation is found between the two temperatures (Pearson's $r = 0.26$).

2.5.2 Stability of the filament

The support of a filament against the gravitational collapse is often discussed in terms of its mass to length ratio, or line mass (M/L). We estimate the line mass from the Hi-GAL H_2 column density map on the pixels that have ammonia detection. The total mass can be estimated as a sum over the column density pixels as follows:

$$M = \mu_{H_2} m_H D^2 \int N_{H_2} d\Omega,$$

where $D = 2.9$ kpc is a kinematic distance to G035.39.

[4] https://github.com/esoPanda/FTbg

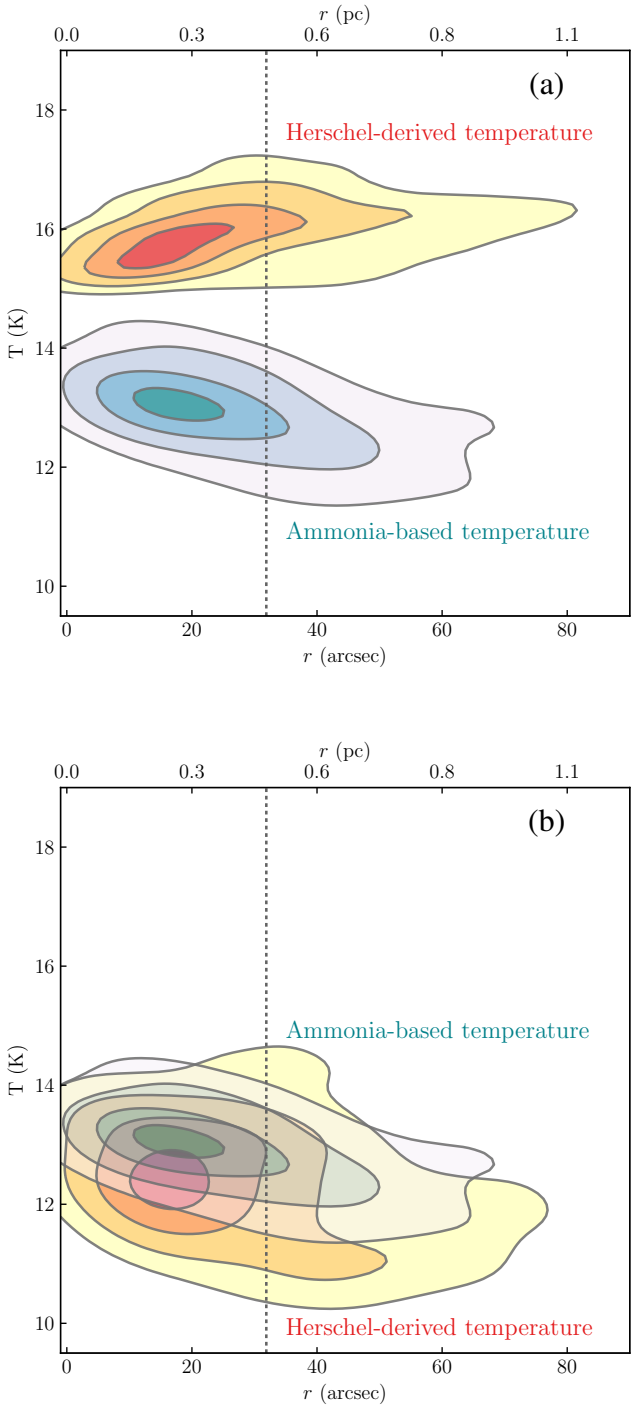

Figure 2.10 (a): Fitted temperatures as a function of distance from the closest massive dense core. The contour overlays show varying levels of kernel density estimation of dust (in red) and gas (in blue) temperatures. The contour σ-levels are equivalent to that of a bivariate normal distribution, starting at 0.5σ and progressing outwards in steps of 0.5σ. The vertical dashed line indicates the beam size of the GBT. (b): Same as panel (a), but for the dust temperatures derived via the Galactic Gaussian (GG) method.

The mass estimate above is representing a sum over all optically thin dust emission, including both the physical region traced by the GBT ammonia observations and a contribution along the line of sight. To subtract line of sight contamination, we we make a simplistic assumption that the total gas column of this extra LoS material is equal to a mean $N_{\mathrm{H_2}}$ value along the bounding contour around the NH_3 (2, 2) detection of the main velocity component. We apply a correction offset of 2.64×10^{22} cm^{-2} to the G035.39 gas column density map. By summing over the column densities within the bounding contour, we find the mass of G035.39 to be 1218 $M_\odot$, corresponding to $(M/L) \approx 223\ M_\odot$ pc^{-1}. We argue that this value, limited both by the sensitivity-limited (2, 2) detection and the column density correction above, should resemble a lower limit to the line mass of the filament. A similarly derived (M/L) value for the (1, 1) detection yields a line mass of 319 $M_\odot$ pc^{-1}, while the mass to length ratio of the filament without the envelope subtraction is 634 $M_\odot$ pc^{-1}. Similarly, if the GG and SMF-derived densities are used to calculate the line mass as above, we obtain (M/L) values of 635 and 494 $M_\odot$ pc^{-1}, respectively, for slightly different values of T_{dust}. The representative range of line mass values, $223 - 635\ M_\odot$ pc^{-1}, is an order of magnitude higher than the critical line mass of thermally supported filament at 15 K, highlighting the importance of other means of support, such as non-thermal motions or magnetic fields.

Given our ammonia fitting results, we can calculate what critical line mass would be needed for the filament to be in equilibrium. By adapting the conventional filamentary virial analysis (Chandrasekhar & Fermi 1953; Ostriker 1964) to include both thermal and non-thermal support (Fiege & Pudritz 2000) one can estimate the critical line mass to be

$$\left(\frac{M}{L}\right)_{crit} = \frac{2\sigma_{tot}^2}{G},$$

where $\sigma_{tot}^2 = \sigma_{nt}^2 + c_s^2$ is a quadrature sum of the non-thermal velocity dispersion σ_{nt} and the isothermal sound speed c_s. The range of non-thermal motions representative of the filament points to the critical line masses from 50 to 200 $M_\odot$ pc^{-1}, consistently lower than the *Herschel*-derived (M/L) range. Similarly, this critical line mass value regime is lower than the $(M/L)_{crit}$ values derived from the CO emission (470-1070 $M_\odot$ pc^{-1}, Hernandez & Tan 2011; Hernandez et al. 2012). This apparent disparity may result from the bulk of ammonia emission being more sensitive to the inner filament material of G035.39 than the CO data, as the former is known to be relatively enhanced in the denser regions of starless cores (Tafalla et al. 2002), where the CO is frozen-out onto dust grains. This proposition is supported by PdBI observations of continuum structures with much smaller spatial scales (0.03-0.07 pc), where Henshaw et al. (2016a) suggest that magnetic fields are playing an important role against gravitational collapse of compact continuum cores. We suggest that their conclusions on the dynamical state of compact dense cores may be extended to the larger-scale ammonia filament in this study.

2.6 Conclusions

IRDC G035.39–00.33 was studied in its entirety with the Green Bank Telescope. The morphology of the cloud at this resolution resembles that of a smooth filament, more than six parsec in

projected length. Multiple distinct components are present along the line of sight throughout the length of the cloud.

1. We derive a reliable map of the gas temperature for the entire G035.39 cloud. The extended gas reservoir in the IRDC is consistent with being of starless nature ($T_{\rm kin} \sim 11 - 15$ K). We find evidence of gas heating from the embedded protostars, manifested as slight temperature increase around the positions of 70 μm sources.

2. Despite having a similar angular resolution, the *Herschel* observations point to temperatures 2-3 K higher than that of the GBT observations, which can be attributed to the effects of line-of-sight contamination. We show that this offset can largely be mitigated by accounting for the background and foreground emission components. Reliance on the dust temperature maps derived from conventional FIR SED fitting with no accounting for the line of sight contributions may consistently overestimate the temperature of the dense gas.

3. We find the brightest velocity component of G035.39 to exhibit a smooth, consistent velocity gradient of ~0.2 km s^{-1} pc^{-1} magnitude. This velocity gradient is much lower than that found on smaller scales towards G035.39-N, but is consistent with the global gas motions on parsec and GMC scales.

4. Additionally to the large-scale gradient across the filament, local velocity field irregularities point to the presence of substructure and smaller-scale fragmentation at scales not traced by the GBT. We suggest that an intertwined network of compact filaments might exist in the southern part of the IRDC, possibly continuing from the one found in G035.39-N. Higher-angular-resolution observations are needed to fully resolve the sub-structured kinematics of the cloud.

Chapter 3

Subsonic islands in a high-mass star-forming infrared dark cloud

The contents of this chapter were published in *Astronomy & Astrophysics* Journal.
Credit: Sokolov et al., A&A, 611, L3, 2018, reproduced with permission © ESO.

3.1 Abstract

High-mass star forming regions are typically thought to be dominated by supersonic motions. We present combined Very Large Array and Green Bank Telescope (VLA+GBT) observations of NH_3 (1,1) and (2,2) in the infrared dark cloud (IRDC) G035.39-00.33, tracing cold and dense gas down to scales of 0.07 pc. We find that, in contrast to previous, similar studies of IRDCs, more than a third of the fitted ammonia spectra show subsonic non-thermal motions (mean line width of 0.71 km s^{-1}), and sonic Mach number distribution peaks around $\mathcal{M} = 1$. As possible observational and instrumental biases would only broaden the line profiles, our results provide strong upper limits to the actual value of $\mathcal{M}$, further strengthening our findings of narrow line widths. This finding calls for a reevaluation of the role of turbulent dissipation and subsonic regions in massive-star and cluster formation. Based on our findings in G035.39, we further speculate that the coarser spectral resolution used in the previous VLA NH_3 studies may have inhibited the detection of subsonic turbulence in IRDCs. The reduced turbulent support suggests that dynamically important magnetic fields of the 1 mG order would be required to support against possible gravitational collapse. Our results offer valuable input into the theories and simulations that aim to recreate the initial conditions of high-mass star and cluster formation.

3.2 Introduction

Supersonic turbulence has been found to dominate molecular cloud kinematics in star forming regions (Larson 1981). Towards the densest cores within these regions, however, the turbulence dissipates, allowing for the formation of stars (Benson & Myers 1989; Foster et al. 2009). Observationally, this decay of turbulence has been found to manifest itself as a difference in line widths

between the lower-density gas, where the turbulence is scale-dependent, and the higher-density gas tracers, sensitive to the star-forming cores with typical sizes of 0.1 pc (Goodman et al. 1998; Caselli et al. 2002a). This change in gas kinematics, or transition to coherence, has been observationally identified to be a sharp boundary between subsonic and transonic motion regimes in the Perseus B5 region (Pineda et al. 2010a).

While a number of studies have focused on identifying the subsonic motions in low-mass star-forming cores, massive star formation is typically thought to be accompanied by large non-thermal gas motions, as it usually proceeds in highly dynamical environments where the protostars, having shorter dynamical timescales, rapidly accrete material from their surroundings (e.g. Tan et al. 2014). Indeed, recent observations point to the existence of large, pc-scale gas flows towards the star-forming cores (Peretto et al. 2013; Liu et al. 2012b,a; Sánchez-Monge et al. 2013; Henshaw et al. 2014; Liu et al. 2015; Wyrowski et al. 2016). Moreover, non-thermal motions are an important element in the turbulent core model for massive star formation (McKee & Tan 2003), where turbulent motions provide extra support against the gravitational collapse, allowing for greater accretion rates and, ultimately, for a higher stellar mass.

A massive filamentary infrared dark cloud (IRDC) G035.39-00.33 (G035.39 henceforth) at a distance of 2.9 kpc (Simon et al. 2006b) has been extensively studied in the past with a variety of continuum and molecular tracers. The non-thermal velocity dispersions inferred in G035.39 from the single-dish CO observations have been found to be two to three times higher than the sound speed in the medium (Jiménez-Serra et al. 2014), and Henshaw et al. (2014) identified the filaments within the IRDC to be only mildly supersonic ($\mathcal{M} \sim 1.4 - 1.6$) with the 4″ Plateau de Bure Interferometer (PdBI) N_2H^+ (1-0) observations. Furthermore, on large, parsec scales, the molecular gas that forms the IRDC is not affected by the feedback from embedded protostars: widespread CO depletion (Hernandez et al. 2011, 2012; Jiménez-Serra et al. 2014), as high deuterium fractionation levels (Barnes et al. 2016) and low gas kinetic temperatures (Sokolov et al. 2017) were found across the cloud. Despite the cloud's starless appearance at parsec scales, some star formation in the cloud is already underway (Nguyen Luong et al. (2011) find a number of compact 70 μm sources in G035.39, some capable of forming intermediate- to high-mass stars).

By making use of the simultaneously derived temperature structure and the kinematics information obtained from the Very Large Array (VLA) on scales down to 0.07 pc, we are in a unique position to analyse dynamics of dense gas linking the cloud scales to those of the embedded protostars and protoclusters. In this letter, we report the presence of widespread subsonic gas motions throughout G035.39.

3.3 Data reduction

The VLA observations were conducted on May 8, 2010 (project AW776; PI: Ke Wang), in two consecutive sessions, mapping the NH_3 (1,1) and (2,2) inversion transitions in the compact D-configuration as a five-point mosaic covering the entire IRDC. The separate sessions allowed the spectral setup to achieve the complete hyperfine structure coverage of the NH_3 transitions with a resolution of 15.625 kHz. The data were calibrated on the quasars J1851+005 (gain),

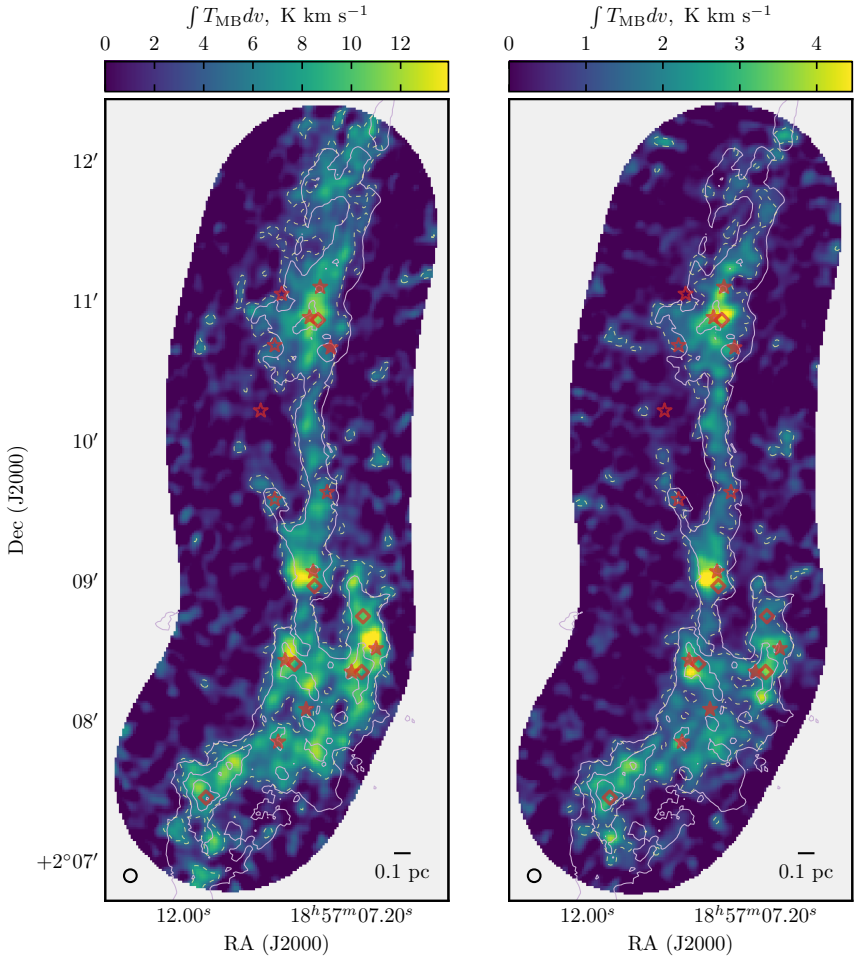

Figure 3.1 Left to right: combined VLA+GBT integrated intensities of the observed ammonia (1,1) and (2,2) lines, computed between 42 and 47 km s^{-1}. The white dotted contour marks the significance level of the integrated intensity of each line at the $3\sigma_I$ level, where σ_I is the integrated intensity uncertainty (Mangum & Shirley 2015). The white solid contours show the infrared extinction contours (Kainulainen & Tan 2013) starting from $A_{\rm V}$ = 30 mag and progressing inwards in steps of 30 mag. The open and filled red stars denote the positions of the Herschel sources from Nguyen Luong et al. (2011) below and above 20 $M_\odot$, respectively, while the open diamonds mark the location of cores from Butler & Tan (2009, 2012).

J2253+1608 (bandpass), and 3C48 (flux) within the CASA data reduction package.

The calibrated visibilities were deconvolved with CASA task TCLEAN using the multi-scale CLEAN algorithm (Cornwell 2008), with Briggs weighting and robust parameter set to 0.5. We taper the visibilities to achieve a similar synthesized beam between the two ammonia lines. To account for the missing flux, we fill in the zero spacing information from the ammonia data taken with the Green Bank Telescope (GBT). Detailed description of the GBT data reduction can be found in Sokolov et al. (2017). The GBT data were converted to spectral flux density units and smoothed to the VLA spectral resolution of 0.2 km s^{-1} with a Gaussian kernel. We then regrid both GBT (1,1) and (2,2) spectral cubes to the VLA spatial grid and apply the VLA mosaic primary beam response to the GBT images. The VLA spectral cubes for both inversion lines are then deconvolved again with TCLEAN, with the TCLEAN mask being determined by combining the VLA only and GBT datasets using the FEATHER task in CASA. By constructing the clean mask from independently feathered images, we ensure that unbiased knowledge of the extended emission is incorporated into the TCLEAN run. The resulting NH_3 (1,1) and (2,2) spectral cubes, gridded into 1″ pixels, have a common restoring beam of 5.44″. The typical rms value of the emission free spectra in the resultant cubes is 14 mJy/beam for NH_3 (1,1) and 5 mJy/beam for NH_3 (2,2) inversion lines in a 0.2 km s^{-1} channel.

3.4 Results

Figure 3.1 presents the integrated intensities of the NH_3 (1,1) and (2,2) lines overlaid with the mid-infrared extinction contours (Kainulainen & Tan 2013). The good correspondence between the two morphologies indicates that the dense gas, forming the bulk of the IRDC, is well traced with our combined ammonia observations. In addition, both inversion transitions have similar dynamic range (cf. $3\sigma_I$ detection contours on Fig. 3.1), allowing us to reliably constrain the gas temperature that depends on the ratio of the two metastable inversion level populations (Ho & Townes 1983).

The two ammonia spectral cubes were simultaneously forward-fitted pixel by pixel with the ammonia spectral profile model using the PYSPECKIT (Ginsburg & Mirocha 2011) Python package and the NH_3 formalism described in Friesen, Pineda et al. (2017). This produced a set of one-, two- and three-component fits to each position,[1] where every fit has optimised values of the excitation temperature, kinetic gas temperature, total ammonia column density, velocity dispersion, and the velocity centroid of the line. Subsequently we make a heuristical decision on the number of velocity components in each spectrum (Fig. 3.2 shows selected spectra) by using the same approach as in Sokolov et al. (2017), namely, by restricting the minimal velocity separation between the components (components' FWHM are not allowed to overlap), and imposing a minimal peak signal to noise ratio (S/N > 3) for each component.

[1] When inspected, no individual spectrum appeared to contain more that three distinct velocity components.

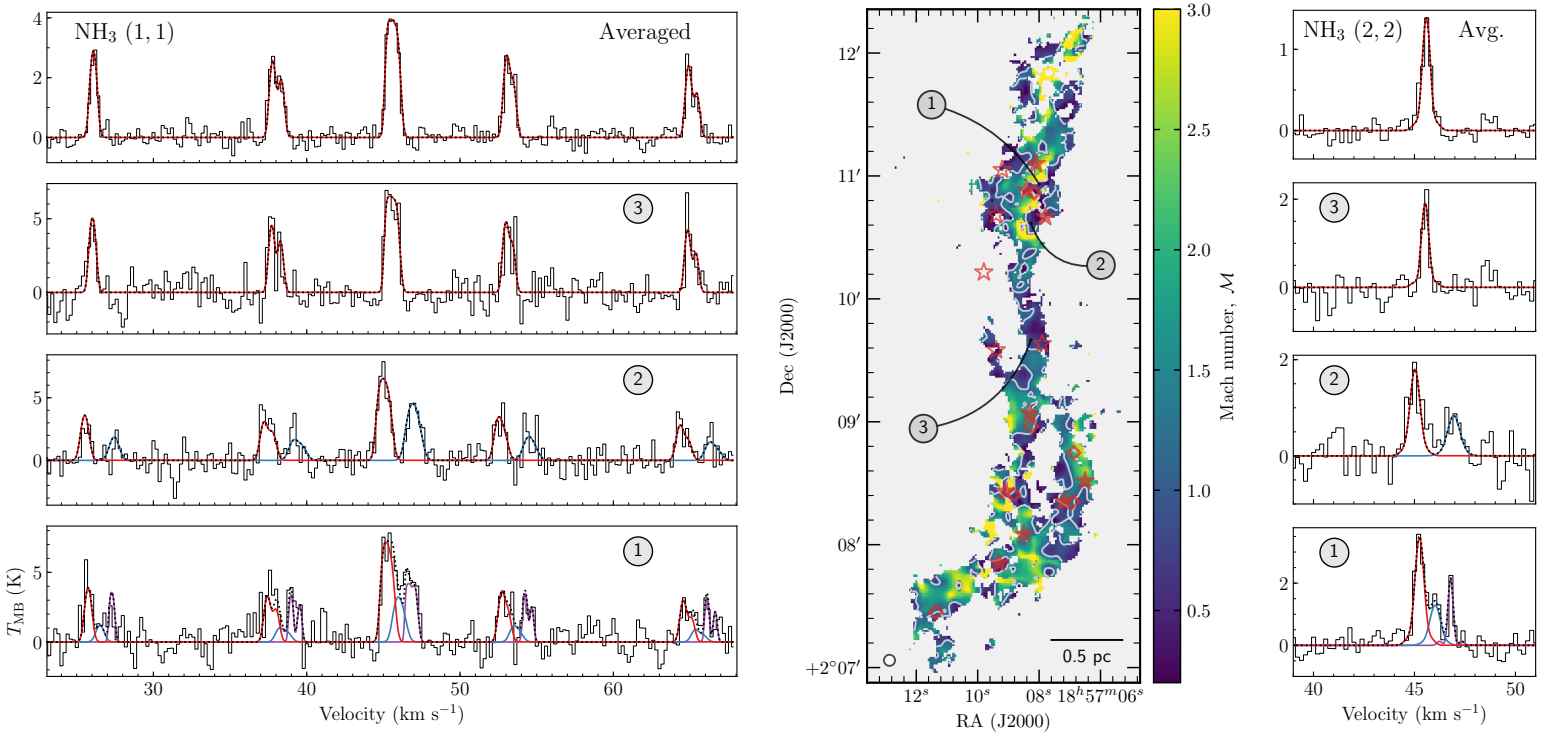

Figure 3.2 A map of the non-thermal velocity dispersion to the gas sound speed in G035.39. In pixels where multiple velocity components are discovered, the smallest value is shown on the image (the analyses throughout the rest of this work use all the values). The markers are the same as in Fig. 3.1, and the solid white line contours indicate the transition at $\sigma_{\rm nt}/c_{\rm s} = 1$. The side panels to the left and right of the map show (1,1) and (2,2) spectra towards the numbered positions. The spectra are overlaid with their best-fit model, with individual velocity components plotted in colour. The topmost spectra, unlike the others, show an averaged spectrum across the subsonic island at α(J2000) = 18h57m08s, δ(J2000) = +2°09′45″. An independently conducted fit, shown in red, yields $\mathcal{M} = 0.72 \pm 0.04$.

In order to quantify the degree of non-thermal motions in the cloud, we calculate the non-thermal line widths by subtracting in quadrature both the thermal line widths and the channel width from the observed line widths. The thermal line widths are determined for each component using the fitted kinetic temperatures, which have a mean of 12.0 K and a standard deviation of 2.2 K across the entire map. We then derive the ratio of the non-thermal velocity dispersion component to the sound speed in the medium, $\mathcal{M} \equiv \sigma_{\rm nt}/c_{\rm s}$ for all the fitted components. We propagate the uncertainties on the gas kinetic temperature and the line widths into the Mach number uncertainties. The 25th, 50th, and 75th percentiles for the uncertainty distributions are $\sigma_{T_{\rm d}} = 1.7$, 2.5, and 3.0 K, respectively, for the gas temperatures, and $\sigma_{\mathcal{M}} = 0.079$, 0.120, and 0.192, respectively, for the Mach number errors.

We present the spatial distribution of the Mach number, $\mathcal{M}$, in Fig. 3.2. In case of more than one velocity component determined along the line of sight (~7%), the one with the smallest $\mathcal{M}$ is shown. While this choice was made for visual clarity, we emphasise that in all other analyses in this paper the full range of the $\mathcal{M}$ values is used. The map shown in Fig. 3.2 reveals the presence of multiple regions of subsonic motions in the G035.39, hereafter referred to as islands of coherence.

More than a third (38.8% of 7680) of all the spectral components have non-thermal gas motions in the subsonic regime ($\mathcal{M} < 1$), while 42.0% are mildly supersonic ($1 < \mathcal{M} < 2$). The remaining data, ~19.2% of positions, show the non-thermal gas motions higher than the sound speed ($\mathcal{M} > 2$). In addition to their spatially clumped appearance, the subsonic islands exhibit a higher degree of coherence. The standard deviation of the transonic and supersonic line width population is 0.15 and 0.40 km s^{-1} respectively, consistently higher than the 0.08 km s^{-1} computed on the subsonic lines of ammonia.

3.5 Discussion

Regions of massive star formation are generally thought to harbour internal motions larger than those of their lower-mass counterparts. To illustrate the difference between the previously found degrees of non-thermal motions and the ones found in G035.39, we plot the Gaussian kernel density estimate (KDE) of the sonic Mach number distribution for all the fitted ammonia components in Fig. 3.3. In a VLA survey of 15 IRDCs, Sánchez-Monge et al. (2013) find that in 79 cores of differing evolutionary stages, the earliest "starless core" class has typical line widths and temperatures of 1.0 km s^{-1} and 16 K. While these values are considerably lower than the corresponding ones for the protostellar stages studied (cf. Fig. 3.3 for the average values of $\sigma_{\rm nt}$), they are still above the typical values found in G035.39 (Henshaw et al. 2014 find mean $\mathcal{M}$ of 1.4–1.6 for the three filaments towards the northern part of the IRDC, and a fraction, 21%, of their spectra is subsonic). A similar VLA survey of IRDC kinematics by Ragan et al. (2012) found no values of $\mathcal{M}$ below 2, favouring an even higher degree of non-thermal motions present inside the massive dense cores. Three other VLA surveys of ammonia (Lu et al. 2014; upper limit of 1.3 km s^{-1} on line widths in Bihr et al. 2015; typical $\mathcal{M}$ from 3 to 5 reported in Dirienzo et al. 2015) report highly supersonic gas motions within IRDCs. We suggest that the coarser spectral resolution of the previous VLA ammonia studies in similar IRDCs might have inhibited

the detection of the subsonic regime, as our spectral resolution of 0.2 km s^{-1} is higher than that of the previous studies (0.6 km s^{-1} in Ragan et al. 2012; Lu et al. 2014; Dirienzo et al. 2015; 0.6 km s^{-1} for most of the data used by Sánchez-Monge et al. 2013; 0.8 km s^{-1} in Bihr et al. 2015). Our results thus point to consistently lower line widths and temperatures than those found in other IRDCs, and closer to the typical values in nearby Gould Belt low-mass star-forming regions (e.g. Friesen, Pineda et al. 2017).

It is plausible to assume that the velocity dispersions we find might also be suffering from an instrumental bias due to insufficient spectral resolution. There are two reasons why this does not diminish our findings. Firstly, the mean observed line width of 0.71 km s^{-1} is well resolved with the channel width of 0.2 km s^{-1}, and the ammonia emission, split among many hyperfine transitions, has its spectral line profile described across a large number of channels. Therefore, constraining the velocity dispersions is typically not a problem (mean uncertainty on velocity dispersions: 0.015 km s^{-1}). Secondly, even if there is a spectral resolution bias present, it will bias the obtained velocity dispersions towards larger values (Friesen et al. 2009), thus only strengthening our claim of the subsonic motion regime detection. We note that even if our analyses are repeated without subtracting the channel width from the observed line width, we still recover a significant fraction of the subsonic spectra (0.36 of the all the fitted components vs. the original 0.39 fraction). Additionally, the distribution of the line widths we obtain might be biased due to misidentification of the number of velocity components along the line of sight. As our heuristics to choose the number of components depend on all components in both ammonia lines being significantly detected, we expect a fraction of the multiple-component spectra to be fitted with a broader component model when those conditions are not met. This misspecification would only produce broader, not narrower, line widths, and may explain some Mach numbers in the tail of the Fig. 3.3 distribution, as well as a sharp, border-like transition in the northern part of the IRDC (Fig. 3.2). Despite this bias, 87% of the subsonic components belong to spectra with single velocity component.

Figure 3.3 shows a subsample of values derived within one FWHM of the synthesized VLA beam around the protostellar 70 μm sources identified in Nguyen Luong et al. (2011) alongside the remaining data. As seen from the figure, the overall distribution of the non-thermal motions around the protostellar sources does not show a clear deviation away from that of the rest of the IRDC, indicating that the embedded sources do not yet exert enough feedback on the surrounding material to disturb the cores that harbour them (at least not on the 0.07 pc scales resolved with our VLA observations). On the other hand, neither do the star-forming cores appear to resemble the "coherent core" picture of low-mass star formation (no correlation of $\mathcal{M}$ with A_V; Pearson's r = 0.10). It is likely that to disentangle these effects, a higher-angular-resolution kinematics study is needed to resolve the densest gas structures, similar in size to the narrow (0.03 pc) filaments found in recent ALMA continuum image of G035.39 (Henshaw et al. 2017). The importance of high-angular-resolution observations is also shown by Hacar et al. (2018), who have recently resolved the Orion integral shaped filament into narrow 0.035 pc fibers of mostly subsonic nature, and a recent high-spectral-resolution study of SDC13 that shows localized traces of subsonic motions in the combined JVLA and GBT NH_3 observations (Williams et al. 2018). While future higher-angular-resolution studies dedicated to IRDC kinematics are needed in order to resolve the scales of the massive cores within the IRDCs, and probe the exact nature of transition into

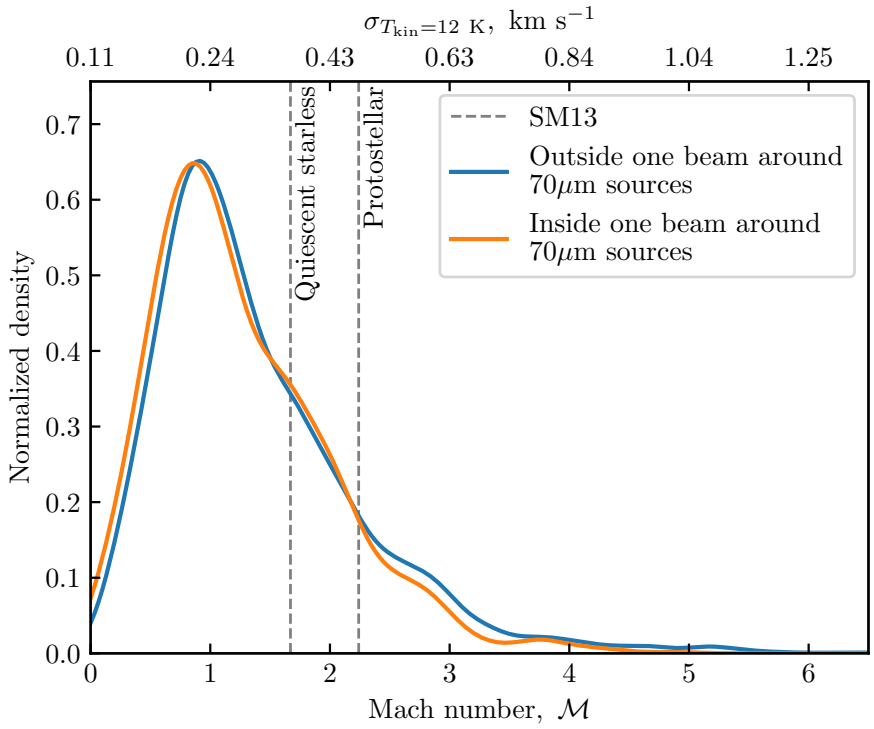

Figure 3.3 KDE distribution of the non-thermal line widths to sound speed ratios in G035.39, peaking at $\mathcal{M} = 0.91$. The upper axis shows equivalent velocity dispersions for $T_{\rm kin} = 12$ K, a mean temperature in our sample. A subsample extracted from pixels within one synthesized beam of the VLA around the 70 μm Herschel sources (Nguyen Luong et al. 2011) is shown in orange, alongside the remaining data plotted in blue. Overplotted for the reference are the mean values for starless and protostellar IRDC cores found in Sánchez-Monge et al. (2013).

subsonic regime, our results show that some of the star-forming cores are forming in a quiescent environment.

The narrow ammonia line widths found in G035.39 indicate that due to reduced turbulent support parts of the IRDC are prone to gravitational collapse, unless they are supported by magnetic fields. Henshaw et al. (2016a) find that magnetic field strengths of a few 100 μG are needed to virialize dense cores in the northern part of the IRDC, while Tan et al. (2013) have observed four massive clumps in a sample of ten well studied IRDCs from Butler & Tan (2009, 2012), finding that magnetic fields of up to 1 mG strength are needed to support the cores in virial equilibrium (cf. ~2 mG in a follow-up study of Kong et al. 2017b). Likewise, Zhang et al. (2015) analysed thermal dynamic properties of dense cores in IRDC G028.34, and found that a magnetic field strength of several milliGauss is required in order to virialize these cores. While the subsonic regions identified in our VLA observations do not always correspond to the density structure and therefore are not exclusively tracing the star-forming cores, we argue that by considering the largest bound $\mathcal{M} < 1$ contours to be magnetized cores in virial equilibrium we can arrive at an order of magnitude estimate of the magnetic field strength needed to support the enclosed region

against collapse. For the three largest continuous subsonic islands in G035.39, each spanning in excess of seven VLA beam areas, we estimate masses of 22–45 $M_\odot$ from the mass surface density map of Kainulainen & Tan (2013) (or 18–21 $M_\odot$ if the smallest value of mass surface density is representative of the line-of-sight contribution). For these values, assuming spherical core geometry, we follow the approach of Tan et al. (2013) to derive the magnetic field strengths of ~1.5–2 mG (~0.8–1.8 mG for the background subtraction case) needed to virialize the three regions.

Polarization studies of massive star-forming cores find that magnetic fields play an important role during their collapse and fragmentation (Zhang et al. 2014), and field strengths up to a few milliGauss are supporting active high-mass star-forming regions (Frau et al. 2014; Qiu et al. 2014; Li et al. 2015; Pillai et al. 2016). Recent polarization measurements towards early-stage IRDCs (Pillai et al. 2015; Santos et al. 2016; Beuther et al. 2018) find field strengths of a few hundred microGauss to a few milliGauss, that is, the same order as our estimates for G035.39. As G035.39 hosts a number of protostellar sources, it is clear that parts of the IRDC are already unstable or undergoing gravitational collapse. Dust polarization observations of G035.39, together with resolved kinematics tracing accreting and infalling motions of the dense gas, will reveal a comprehensive picture on the stability of this IRDC.

Our findings, enabled by high spectral resolution of the combined VLA and GBT observations, allow us to quantify the islands of subsonic turbulence within the IRDCs for the first time. The results of this work indicate that early stages of massive star and cluster formation can go through stages more similar to their low-mass counterparts than previously thought. We highlight the potential for high-angular- and spectral resolution ALMA observations of IRDC kinematics, needed to reevaluate the role of turbulent dissipation and investigate the exact nature of transition to coherence in early stages of massive star- and cluster-forming regions. If the subsonic regions found here are representative of the kinematics of the massive dense star-forming cores in other IRDCs, the reduced turbulent support and possible increased support from the magnetic fields put constraints on models and simulations aiming to reproduce the initial stages of massive star and cluster formation.

Chapter 4

Multicomponent kinematics in a massive filamentary IRDC

The contents of this chapter will be submitted to the *Astronomical Journal*.

4.1 Abstract

The initial conditions for high-mass star and cluster formation are not fully understood. We investigate the properties of dense filaments within an infrared dark cloud G035.39–00.33 (IRDC G035.39) with ammonia inversion transitions. We combine the Very Large Array (VLA) and the Green Bank Telescope (GBT) data to achieve a 5.44″ resolution mosaic of the whole cloud tracing material down to 0.07 pc scales. We present results of the multiple line-of-sight velocity component fitting to the ammonia spectral line data: centroid velocities, line widths, temperatures, and total ammonia column densities, across the G035.39 cloud. Using agglomerative hierarchical clustering, we identify seven large velocity-coherent components in our data, likely representing spatially coherent physical structures. The physical properties derived from our observations reveal complex gas motions present throughout the IRDC, sometimes converging onto the dense cores and protostellar sources within it. The typical magnitude of the velocity gradients peaks at its mode of 0.35 km s^{-1} pc^{-1} and has a long tail extending into higher values of $1.5 - 2$ km s^{-1} pc^{-1}, and is generally consistent with the values found towards nearby low-mass dense cloud cores at the same scales. Contrary to observational and theoretical expectations, we find the NH_3 (1,1) and (2,2) non-thermal line widths to be systematically narrower (by about 30%) than those of N_2H^+ $(1 - 0)$ line transition observed with similar resolution. If the observed ordered velocity gradients represent the core envelope solid-body rotation, we estimate the specific angular momentum to be about 2×10^{21} cm^2 s^{-1}, similar to the low-mass star-forming cores. Together with the previous finding of subsonic motions in G035.39, our results demonstrate an unprecedented level of similarity between kinematics of a high-mass star-forming IRDC and the low-mass star formation regime.

4.2 Introduction

The formation of stars from the diffuse ISM is a multi-stage process of gas channeling and mass assembly. In the well-established low mass star formation picture, individual stars are formed from dense cores, which become gravitationally unstable once enough mass has been accumulated from their surroundings. While this process is thought to be relatively well understood, the formation of high-mass stars and star clusters occurs more rapidly and is a more dynamic process, requiring efficient gas channeling onto the protostellar sources, and its initial conditions are still not very well understood (e.g., Tan et al. 2014).

Observations of the earliest stages of massive star and cluster formation are greatly hindered by the high extinction of, and large distances to, high-mass star-forming regions, and resolving the physical scales of the massive starless cores typically requires interferometric observations in radio or submillimeter wavelengths. The initial conditions of this process, such as density and temperature profiles on the core scales (∼0.1 pc), turbulence levels, accretion from the surrounding envelopes, magnetic field strengths, or the angular momentum of the core, are inherited from the more extended scales of clouds or protostellar clumps (∼1 pc), and are often poorly constrained by observations. As these conditions directly regulate the subsequent fragmentation and infall of the star-forming material (Tan 2017; Motte et al. 2017), high-angular resolution observations of the dense IR-dark gas with little evidence of disruptive feedback can provide improved constraints on the theoretical models and numerical simulations aiming to recreate the formation of high-mass stars and star clusters.

Large-scale infrared surveys of the Galactic plane (Perault et al. 1996; Egan et al. 1998) have revealed Infrared Dark Clouds, or IRDCs, which are the most promising candidates to host the earliest stages of massive star and cluster formation (Rathborne et al. 2006). Often appearing as dense extinction ridges, tracing higher-density spines of their parent GMCs (Hernandez & Tan 2015; Schneider et al. 2015), IRDCs appear as cold (10 − 15 K), filamentary, and high-column-density (10^{23} − 10^{25} cm^{-2}) and high-mass (10^{3-5} $M_\odot$, Kainulainen & Tan 2013) extinction features, typically hosting a number of high-mass cores (Rathborne et al. 2006). IRDCs vary greatly in their masses, densities, and star-forming activity (Kauffmann & Pillai 2010). Rathborne et al. (2006), to select the IRDCs that are representative of the earliest stages of massive star formation, have selected 38 darkest clouds with known kinematic distance from the Simon et al. (2006b) sample, which contains over 10,000 IRDCs, and have studied their continuum emission, showing that the clouds are further fragmented into high-mass cores with a median mass of 120 $M_\odot$. Butler & Tan (2009) studied mid-infrared extinction of 10 IRDCs from the Rathborne et al. (2006) sample, selecting the clouds that are nearby, massive, and show relatively simple diffuse emission. Butler & Tan (2012) identified a number of compact ($R \sim 0.1 - 0.2$ pc) dense cores embedded in these ten IRDCs and discussed their star-forming potential.

In this study, we investigate the physical properties of dense gas connecting the cloud to core scales (from the IRDC size of ∼6 pc down to 0.07 pc) for one of ten clouds in Butler & Tan (2009, 2012), IRDC G035.39–00.33. It is seen as a highly filamentary feature at mid-infrared wavelengths (e.g., Butler & Tan 2009) and belongs to a larger GMC complex (Hernandez & Tan 2015). By combining available NIR and MIR extinction measurements, Kainulainen & Tan (2013) have estimated the mass of G035.39 to be 16700 $M_\odot$. The cloud temperature is rela-

tively cold (~15 K from dust emission measurements, Nguyen Luong et al. 2011), with high CO depletion and large deuteration fractions from single dish observations indicating that the cloud is governed by cold chemistry with little evidence of stellar feedback (Hernandez et al. 2011; Jiménez-Serra et al. 2014; Barnes et al. 2016). Jiménez-Serra et al. (2010) have discovered extended SiO (2-1) emission throughout the northern part of the cloud, suggesting that its origin may arise from a slow shock from the formation the IRDC (a possibility later explored by Henshaw et al. 2013; Liu et al. 2018) or from the stellar feedback driven by embedded YSOs (suggested to be only partially responsible for the SiO emission Nguyen Luong et al. 2011). Despite its starless appearence on large, pc-scales, Nguyen Luong et al. (2011) find a population of protostellar cores within G035.39, nine of which are massive enough (> 20 $M_{\odot}$) to form intermediate to high-mass stars. On smaller scales, Henshaw et al. (2014) have studied the kinematics of the dense gas in the northern part of the IRDC, resolving narrow dense filaments in it with a velocity pattern suggesting a dynamical interaction between the filaments and the dense cores in the cloud.

In this paper, we present combined Very Large Array (VLA) and Green Bank Telescope (GBT) observations of the IRDC G035.39 the whole cloud. The paper is structured as follows. In §4.3 we summarize the data reduction, our strategy for VLA and GBT dataset combination, and present an overview of its outcome. In §4.4 we describe the separation of the data into individual components, and present the spectral line fitting results for the largest among them. In §4.5 a quantitative comparison with similar studies of G035.39 is made, the implications of cloud kinematics for velocity flows around the protostellar and continuum sources are made, and the stability of the individual components is being discussed. Finally, a summary of our main results comprise section §4.6.

4.3 Data Reduction

The Karl G. Jansky Very Large Array (VLA) observations (project AW776; PI: Ke Wang) in compact D-configuration were carried out on May 8, 2010, mapping the NH_3 (1,1) and (2,2) inversion lines in the K-band across the whole G035.39 cloud in a five-point mosaic. The two ammonia lines were mapped in two consecutive sessions, to cover the full hyperfine line structure of both transitions with the first generation VLA correlator at spectral resolution of 15.625 kHz. The data were calibrated on the quasars J1851+005 (gain), J2253+1608 (bandpass), and 3C48 (flux) within the CASA data reduction package. The data presented have been previously described in Sokolov et al. (2018).

We have deconvolved the calibrated visibilities in CASA, using the TCLEAN task, with the multi-scale CLEAN algorithm (Cornwell 2008), following the Briggs weighting with robust parameter set to 0.5. To achieve a similar synthesized beam for the two ammonia lines, we tapered the visibilities and applied a common restoring beam of 5.44″. To recover the extended ammonia emission, we fill in the missing flux from the Green Bank Telescope (GBT) data. A detailed description of the GBT data reduction can be found in Sokolov et al. (2017). Before merging the data, the GBT images were converted to spectral flux density units and convolved to the VLA spectral resolution of 0.2 km s^{-1}. After regridding both GBT spectral cubes to match the VLA

grid, we apply the VLA mosaic primary beam response to the GBT images. Subsequently, the VLA (1,1) and (2,2) images were deconvolved again with TCLEAN task, with the TCLEAN mask being determined by combining the VLA only and GBT datasets using the FEATHER task in CASA. Constructing the clean mask from independently feathered images ensures that unbiased knowledge of the extended emission is incorporated into the TCLEAN run. For specific details on the imaging strategy, we refer to Appendix 4.7, where a full description of the imaging and dataset combination is presented. The resulting NH_3 (1,1) and (2,2) spectral cubes, gridded into 1″ pixels, have a common restoring beam of 5.44″. The typical rms value of the emission free spectra in the resultant cubes is 14 mJy beam^{-1} for NH_3 (1,1) and 5 mJy beam^{-1} for NH_3 (2,2) inversion lines in a 0.2 km s^{-1} channel.

4.3.1 Overview of the data

Figure 4.1 presents the channel maps for NH_3 (1,1) line, showing both a presence of multiple components throughout the IRDC as well as a line centroid change towards blue-shifted regime as one follows the IRDC northwards. The equivalent figure presenting the channel maps for the NH_3 (2,2) line is shown in Appendix 4.8, showing similar morphology.

The parsec-scale ∼0.2 km s^{-1} pc^{-1} quasi-linear velocity gradient, found in the GBT-only data (Sokolov et al. 2017) is present in our combined data, gradually changing the velocity regime of the cloud into the blue-shifted regime as it extends southwards. Superimposed on this kinematics feature, additional velocity components are present. In the northern portion of the cloud, the western side of the IRDC splits off into a secondary, red-shifted, velocity component located around 47 km s^{-1}, in agreement with the previous studies of the cloud (labelled F3 in Henshaw et al. 2013, 2014; Jiménez-Serra et al. 2014). A filamentary-like feature connects the northern region of the IRDC with the southern one, where it appears to split into two individual filaments that then join together at the southern part of G035.39. Additionally, the velocity feature between 42–43 km s^{-1}, seen before as a clump-like structure in the ammonia maps of Sokolov et al. (2017), is now resolved into a distinct filament, orthogonally oriented to the rest of the IRDC.

4.3.2 Line fitting

Molecular line emission tracing the dense gas within G035.39 is known to exhibit multiple line-of-sight velocity components (e.g., Henshaw et al. 2013, 2014; Jiménez-Serra et al. 2014). However, with no clear prior knowledge of the kinematical structure exhibited in the high-resolution ammonia emission, standard algorithms commonly used to fit the line profile are prone to converge away from the global minima or, alternatively, to diverge in the absence of a proper starting point of the algorithm. As our goal is to distinguish the physical properties of velocity-coherent structures, it is crucial to conduct a simultaneous fitting of all line-of-sight components, constraining their line parameters whenever a significant additional feature is present in the spectral profile. At the same time, overfitting has to be ruled out - that is, only statistically significant components have to be taken into consideration for the subsequent scientific analyses.

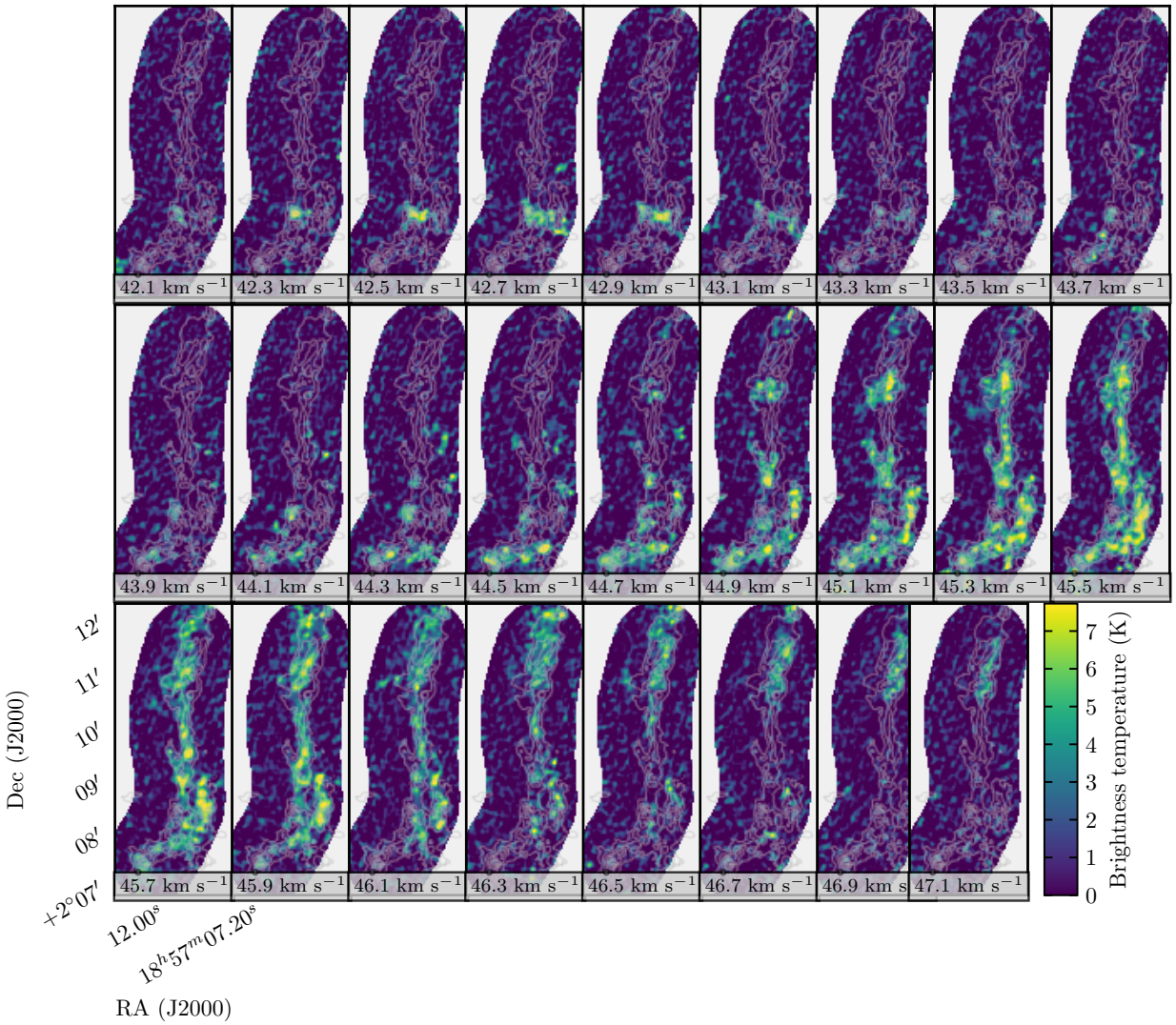

Figure 4.1 Channel maps of the ammonia (1,1) line for the IRDC G035.39. Each panel shows the brightness temperature of the NH_3 (1,1) spectral cube channel of 0.2 km s^{-1} width, with text boxes at their bottom indicating the velocity centroid of the channel. The velocity range of 42–47 km s^{-1} was chosen to capture the main hyperfine group of the inversion transition. The light gray contours show the infrared extinction contours (Kainulainen & Tan 2013) starting from A_V = 30 mag and progressing inwards in steps of 30 mag.

As the VLA spectral cubes consist of about a dozen thousand spectra with S/N ratio higher than three, the common practice of fitting multiple components by eye would require an excessive amount of human interaction resulting in low level of reproducibility, while methods for global non-linear regression are prohibitively computationally expensive for such a high volume of data. Therefore, to fit multiple line-of-sight line components, we employ the same fitting strategy as in Sokolov et al. (2017), where an open-source Python package[1] is used to assist the Levenberg-Marquardt fitter to find an optimal starting point for exploring the parameter space of the spectral model. The free parameters for the ammonia model (same formalism as in, e.g., Friesen et al. 2017), implemented within PYSPECKIT package (Ginsburg & Mirocha 2011), are split into a multi-dimensional parameter grid, and a synthetic ammonia model is then computed for each. Subsequently, every spectrum in our VLA data is then cross-checked with every model computed to calculate the corresponding residual. The model parameters for a given spectrum that yield the best residual (i.e., the least sum of squared residuals) are taken to be the starting value for the Levenberg-Marquardt fitting algorithm.

Three independently-derived sets of best fitting parameters are obtained in such a fashion, for one-, two-, and three-component models. The three fitting sets are then merged into one following a set of heuristical criteria that determines the number of line-of-sight components in a given pixel of the spectral cube. The heuristical procedure is described below:

1. First, the three component model is considered to be valid.

2. If any of the three components are below signal-to-noise of three — for both NH_3 (1,1) and (2,2) transitions — the model is marked as rejected. Similarly, should the half-sum of FWHM of any neighboring components be less than the separation between their velocity centroids (i.e., the FWHM are not allowed to overlap), the model is rejected. This restriction is imposed to avoid line blending.

3. A rejected model is replaced with a simpler one: the three-component model is replaced with the two-component one, and a rejected two-component model is replaced with a one-component model.

4. The replaced models are required to meed the same heuristical criteria as in step 2.

5. If none of the fitted models are valid, we consider the spectrum to be a non-detection.

6. The steps 1 – 5 are repeated for all the spectra in the combined spectral cube, until a collection of ammonia fitting parameters is assembled in a PPV space.

In the above procedure, the second step requires imposing constraints for both (1,1) and (2,2) lines. This is done to assure that the physical properties that depend on the population ratio of the two transitions (kinetic temperature and ammonia column density) are reliably constrained. Throughout this paper, this is the method we refer to as *strict censoring* criterion for arriving at the PPV structure in the IRDC. However, we note that in principle, should only the kinematic

[1] https://github.com/vlas-sokolov/multicube

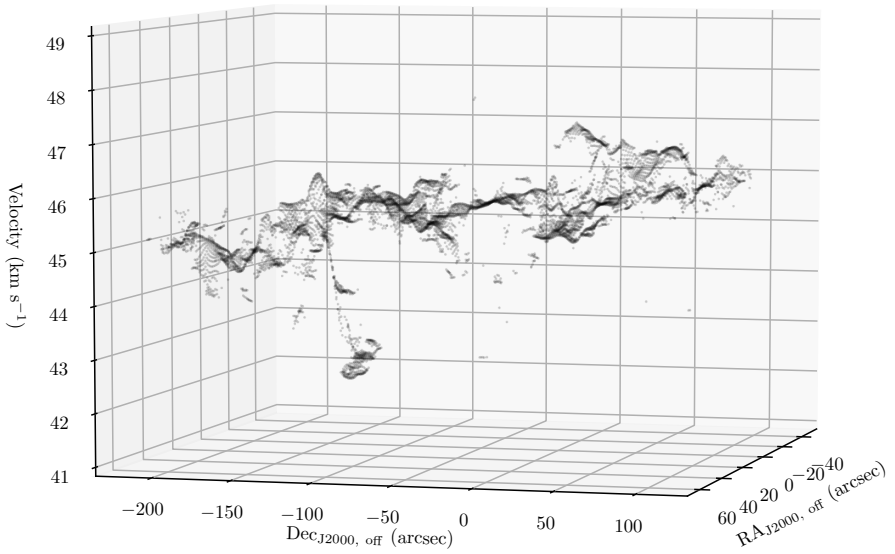

Figure 4.2 A PPV diagram of all fitted velocity components within IRDC G035.39. Every point in the diagram represents a best-fit velocity centroid for a single ammonia line component, and darker shade of black indicates greater density of points along the on-screen projection. When constructing this diagram, we required the signal-to-noise ratio of both (1,1) and (2,2) lines to be greater than three. The coordinates axes are specified relative to the offset at α(J2000) = 18h57m08s, δ(J2000) = +2°10′30″. An interactive version of the diagram will be maintained under https://vlas-sokolov.github.io/post/cloudH-ppv/.

information be needed from our ammonia data, either one of the inversion line detections would constrain it in our simultaneous line fitting. Therefore, we consider an additional method, which we call *relaxed censoring*, which naturally results in a PPV structure with larger average number of line-of-sight components. Despite the differences in these two approaches, the average kinematic properties we will derive later will not be significantly changed if a relaxed censoring method is used (Appendix 4.9 provides quantitative comparison between the two approaches), therefore we use the strict censoring approach because it allows us to discuss the temperature structure of the velocity components in addition to their kinematics.

4.4 Results

4.4.1 Velocity components

Figure 4.2 shows the position-position-velocity (PPV) space with the best fit line-of-sight components, which demonstrates the complex kinematics of the G035.39 cloud. As different parts of the cloud may represent unique, non-interacting physical structures, it is necessary to identify the components that are linked in both position and velocity. The inability to separate such unique

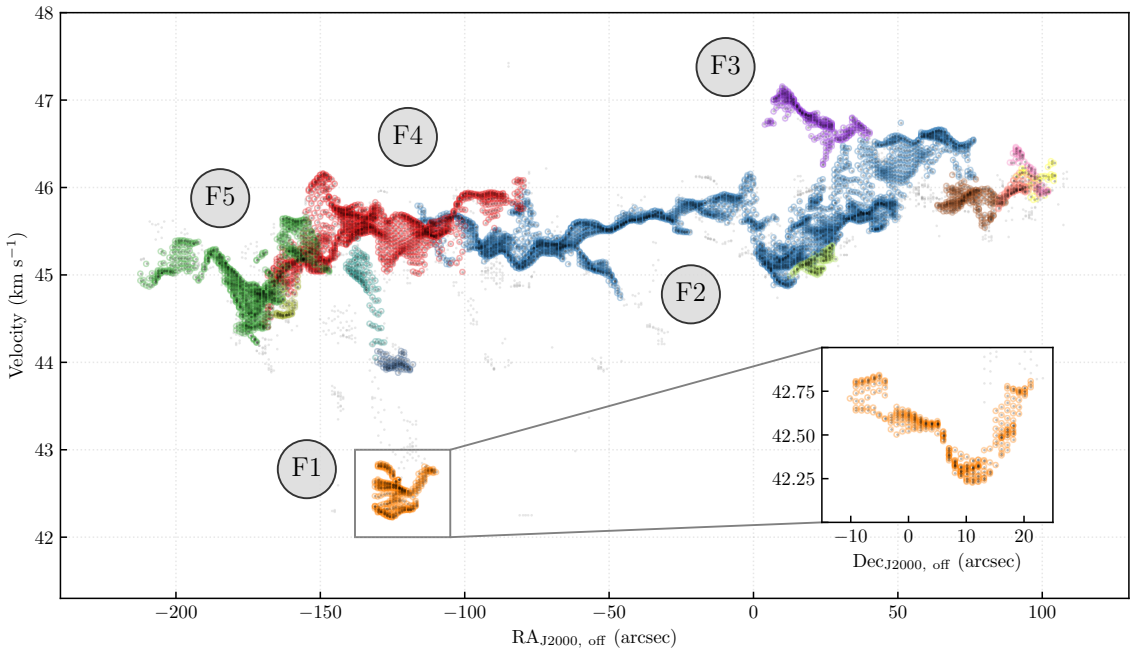

Figure 4.3 A PPV-diagram of the fitted velocity components within IRDC G035.39 along the Right Ascension projection. The coordinates are given in arcsecond offset relative to the α(J2000) = 18h57m08s, δ(J2000) = +2°10′30″ coordinate. All the data are plotted in black, similarly to Fig. 4.2, and individual velocity components are marked in different colors. The data not found to be associated with any clusters are plotted in gray. The figure shows the clustering obtained with the strict masking criteria (introduced in §4.3.2); the equivalent figure for relaxed censoring can be found in Appendix 4.9. In addition to the R.A. projection, a projection along Dec. is shown in the inset axis for the F1 filament.

structures would hinder quantitative analyses on the gas motions within the IRDC.

Since non-hierarchical algorithms have problems with extended emission (e.g., Pineda et al. 2009) we use a hierarchical clustering of discrete PPV data from the G035.39 dataset. For this task, we make use of the Agglomerative Clustering for ORganising Nested Structures (ACORNS), a clustering algorithm to be fully described in Henshaw et al. (in prep.) (cf. Barnes et al. 2018). In simple terms, ACORNS links together PPV points into clusters. The algorithm starts with the most significant data point, and proceeds to link it together with any nearby points that satisfy the linking criteria. After the first cluster has been assigned in such fashion, the most significant point amongst unassigned dataset is taken, and the linking is repeated. For our combined ammonia data, we set the "significance" of the datapoints in ACORNS to be the peak signal-to-noise ratio of the combined NH_3 (1,1) and (2,2) spectra. The procedure runs until no data points are left unassigned, and a dendrogram-like cluster hierarchy, assigning clusters to branches and trees (in a manner similar to Rosolowsky et al. 2008b) is established.

The parameters that defined the linking criteria of the ACORNS algorithm were the following. The clusters were restricted to be at least 9 pixels in size, and the link between neighboring datapoints was set to be smaller or equal to the velocity resolution of the data (0.2 km s^{-1}). Additionally, no links with line widths of twice the velocity resolution (0.4 km s^{-1}) were allowed to be established. In our ACORNS run, the PPV points below signal-to-noise significance of three were set to be excluded.

We obtain two sets of results from the ACORNS clustering for the two masking strategies introduced in §4.3.2. The strict censoring results in thirteen hierarchical clusters, seven of which cover an area in excess of five synthesized VLA beams (i.e. have physical properties constrained in more than 116 pixels). The overall view of the structures identified is shown on Fig. 4.3, while the separated maps of the seven largest components will be presented in the following sections. The relaxed masking results in twenty-four components, of which ten are spanning a significantly large area (a comparison with the adopted method is shown in Appendix 4.9).

Continuum sources within the velocity components

Throughout this study, we will relate the continuum sources discovered towards the IRDC, in particular the mass surface density cores of Butler & Tan (2012) and the 70 μm sources of Nguyen Luong et al. (2011), to the continuous ammonia-emitting regions identified as velocity-coherent structures in PPV-space. In order to establish whether a given continuum source is related to the ACORNS-identified components, we use the following heuristics. Firstly, we require at least 24 pixels with significant ammonia spectra detections (corresponding to an effective area larger than that of one VLA beam) to be enclosed in a three-beam diameter around the coordinate of interest. Secondly, to assert the direct proximity of the continuum source to the velocity component under consideration, we require at least one significant detection within one beam radius around the position of interest. These heuristics are computed on every continuum source of interest, and for every velocity component detected. Sources that match the criteria above will be referred to as sources related to the ACORNS component throughout this study.

Table 4.1 gives a summary of the velocity components we identify in this section, and lists their corresponding related sources along with the average properties of the components. The

component names follow their respective colors on Fig. 4.3, and only those spanning in excess of five beam sizes are listed. In case a source appears to be related to more than one component, it is listed several times in the table.

Table 4.1. The velocity components identified with ACORNS.

Component ID[a]	Size[b] (pixels)	V_{lsr} [b] (km s^{-1})	σ [b] (km s^{-1})	T_{kin} [b] (K)	Related sources (Butler & Tan 2012)	Related sources (Nguyen Luong et al. 2011)
F2 (Blue)	2981	45.62 ± 0.41	0.28 ± 0.14	12.29 ± 2.18	H5, H6	#12, #28, #6, #20, #5
F4 (Red)	1377	45.46 ± 0.30	0.31 ± 0.12	11.69 ± 1.70	H2, H4	#22, #10, #16
F5 (Green)	927	44.96 ± 0.32	0.32 ± 0.14	12.40 ± 2.03	H1	#7
F1 (Orange)	313	42.52 ± 0.17	0.17 ± 0.06	11.22 ± 1.29	H3	#11
F6 (Brown)	198	45.86 ± 0.10	0.33 ± 0.25	11.20 ± 1.76	-	-
F3 (Purple)	270	46.79 ± 0.18	0.24 ± 0.06	12.12 ± 1.90	-	#18
F7 (Olive)	124	45.14 ± 0.09	0.15 ± 0.05	13.47 ± 1.94	H6	#6

[a]The color labels directly correspond to the component colors on Fig. 4.3.

[b]The mean followed by the standard deviation of the values belonging to the given component.

4.4.2 Velocity structure across the IRDC

Various processes in star-forming clouds, such as, turbulence, gravitational acceleration of infalling material, feedback from the embedded sources, or solid-body rotation can create line-of-sight velocity gradients. In order to perform a qualitative analysis of the velocity gradients, we have to interpolate the slope of discrete $V_{\rm lsr}$ measurements on the plane of sky. To achieve this, we use a variation of the Moving Least Squares method (Lancaster & Salkauskas 1981) for constructing continuous surface from a sample of discrete data. The method, often used in computational geometry and computer vision (e.g., Levin 1998; Schaefer et al. 2006), was independently developed in astrophysics by Goodman et al. (1993) to find velocity gradients from line of sight velocity fields, and has seen considerable usage since (e.g., Barranco & Goodman 1998; Caselli et al. 2002b,a; Tafalla et al. 2004; Kirk et al. 2013; Henshaw et al. 2014, 2016b).

The local line-of-sight velocity gradient is fit to a 2D scalar field given by the nearby PPV points, approximated by a first-degree bivariate polynomial $f(\alpha,\delta) = v(\alpha,\delta) + a\Delta\alpha + b\Delta\delta$, where $\Delta\alpha^2 + \Delta\delta^2$ define a circle of radius R around a given R.A. and Dec. position $\mathbf{r} = (\alpha,\delta)$, and (v,a,b) are the free parameters of the least squares fit. For each velocity component identified and for every position $\mathbf{r}$, we construct a set of valid pixels as follows. First, only the pixels with a well defined $V_{\rm lsr}$ value (i.e. the relevant spectral component having a peak S/N > 3) are included in the velocity gradient analysis, and the rest are masked. Secondly, the moving least squares operates only on the values within three-beam diameter (i.e., $R = 1.5 \times 5.44''$) and only if more than 46 centroid velocity measurements (i.e. filling an effective area larger than two VLA beams) are defined within it. Finally, only spatially continuous regions are considered, and $V_{\rm lsr}$ regions within radius R that are not connected with position $\mathbf{r}$ with valid $V_{\rm lsr}$ pixels are masked as well. For every valid point with fitted $V_{\rm lsr}$ value, an optimal set of parameters $\mathbf{p}(\mathbf{r}) = a_{\mathbf{r}}, b_{\mathbf{r}}$ is obtained by a weighted least-squares fit to a collection of nearby pixels:

$$\mathbf{p}(\mathbf{r}) = \underset{a,b}{\operatorname{argmin}} \left\{ \sum_{\mathbf{r}':\|\mathbf{r}-\mathbf{r}'\|\leq R} \frac{(v_{\rm lsr}(\mathbf{r}') - f(\mathbf{r}',a,b))^2}{w(\mathbf{r}')^2} \right\},$$

where $\mathbf{r}' = (\alpha + \Delta\alpha, \delta + \Delta\delta)$ is a vector on the plane of sky, and $w(\mathbf{r}')$, the weights of the fit at a given position, were set to be the fitting uncertainties on the $V_{\rm lsr}$.

Following Goodman et al. (1993), we derive the velocity gradient magnitude $\|\nabla V_{\rm lsr}\|$ and orientation θ for all the velocity components. Additionally, we propagate each pair of best-fit (a,b) values into uncertainties on $\|\nabla V_{\rm lsr}\|$ and θ. The dominant majority (96%) of the values derived are statistically significant (S/N > 3), with mean value of uncertainties on $\|\nabla V_{\rm lsr}\|$ of 0.06 km s^{-1} pc^{-1}. Fig. 4.4 shows the $V_{\rm lsr}$ for the four largest velocity components (F2, F4, F5, and F1), overlaid with the velocity gradients derived for them.

The overall velocity gradient magnitude distribution peaks at 0.35 km s^{-1} pc^{-1} (Fig. 4.5, values with S/N < 3 are not shown) and shows an asymmetrical tail towards larger values. To study the potential effect of continuum cores dynamically impacting the magnitude of large-scale dense gas motions in the IRDC, we have selected a sub-sample of the velocity gradient magnitudes that we consider to be spatially relevant to the Butler & Tan (2009, 2012) cores. While the distribution of the core-adjacent $\|\nabla V_{\rm lsr}\|$ values appears to be narrower than the overall distribution,

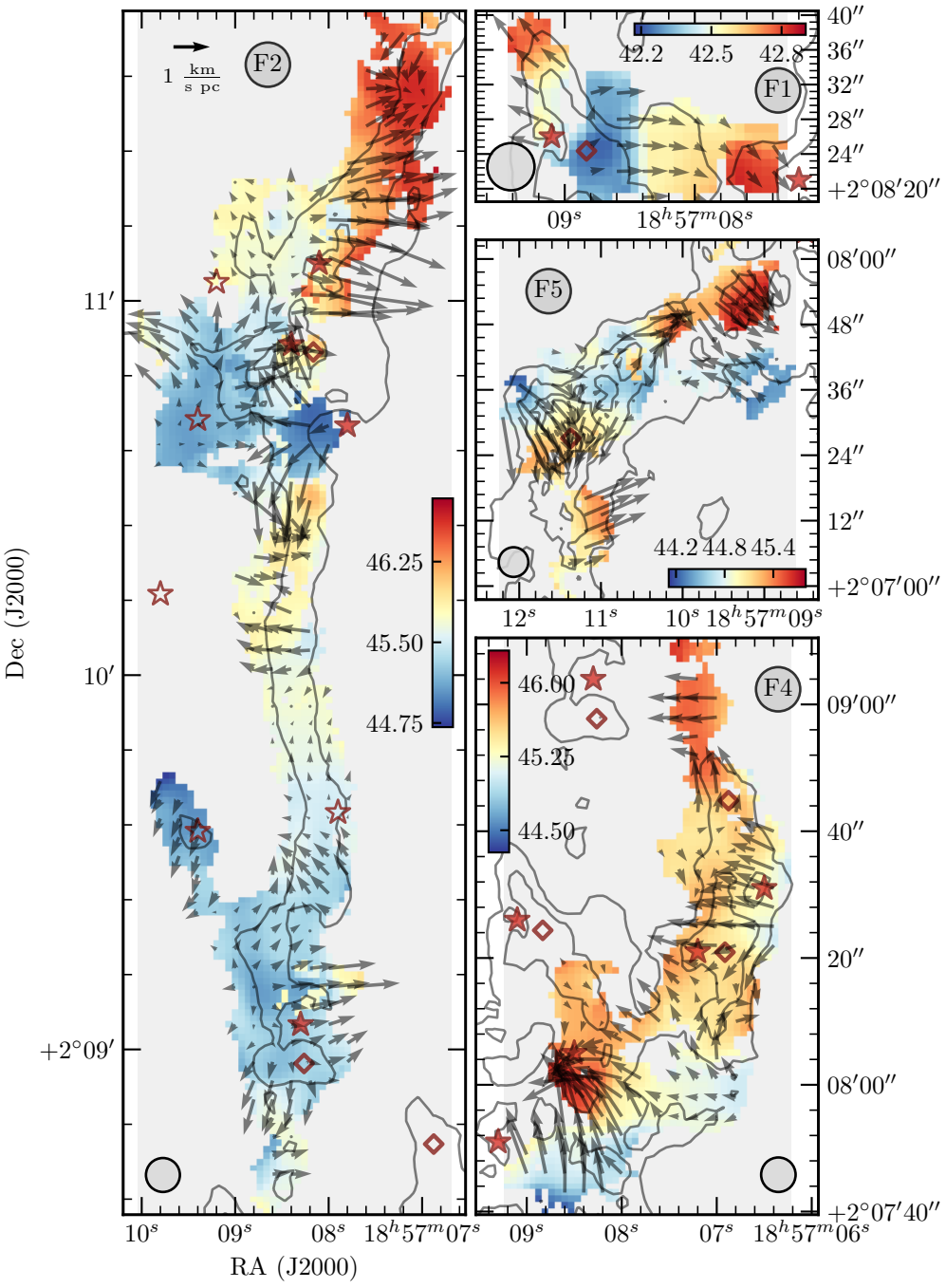

Figure 4.4 A map of derived $V_{\rm lsr}$ values for the biggest velocity components (left panel: F2; right panels, top to bottom: F1, F5, F4), overlaid with the velocity gradient arrows. The directions of the arrows points to the steepest velocity field change in the red-shifted direction, while the arrow lengths represent the relative vector magnitudes of the gradient. The open and filled red stars denote the positions of 70 μm Herschel sources from Nguyen Luong et al. (2011) below and above 20 $M_\odot$, respectively, and the red diamonds indicate the position of cores from Butler & Tan (2009, 2012). The overlaid contours indicate the highest extinction contours from Kainulainen & Tan (2013), ranging from A_V = 40 to 120 mag, progressing in steps of 20 mag.

possibly due to smaller dynamic ranges of density probed, the core-adjacent values are representative for the whole cloud with no statistically significant enhancements. When compared to studies of nearby low-mass dense cores, the values we find are consistently smaller than those of Caselli et al. (2002a), who have performed a similar velocity gradient analysis with N_2H^+, finding mean velocity gradients of $\sim$2 km s^{-1} pc^{-1}. The difference can be partially attributed to the different spatial resolution used in the study. Studying a large sample of NH_3 low-mass dense cores with spatial resolution roughly consistent with ours, Goodman et al. (1993) find typical velocity gradient magnitudes of 0.3 – 2.5 km s^{-1} pc^{-1}, which is broadly consistent with our findings in G035.39 (Fig. 4.5). The resolution difference is also apparent when we consider the previous results from Henshaw et al. (2014), who, mapping the N_2H^+ (1-0) transition northern part of the IRDC with 4″ resolution, find velocity gradient magnitudes reaching the values of 1.5 – 2.5 km s^{-1} pc^{-1}, in closer agreement with the values found in Caselli et al. (2002a) using the same molecular transition.

4.4.3 Temperature maps

Following the line fitting and component separation procedures outlined in §4.3.2 and §4.4.1, respectively, we arrive at the highest angular resolution temperature maps ever taken for G035.39. Furthermore, the sensitivity of our combined observations allows us to resolve the temperatures for the line-of-sight components in the IRDC. Fig. 4.6 shows a comparison between the $T_{\rm kin}$ distribution and the temperature values within one VLA beam around individual 70 μm sources. Compared to the overall distribution of the kinetic temperature, which peaks at 11.7 K and has typical values in the 9 – 15 K range, the $T_{\rm kin}$ values in the vicinity of the 70 μm sources show slight temperature enhancements.

In the GBT-only analysis, Sokolov et al. (2017) identified localized heating at the location of massive protostellar sources. This effect, however, was only seen as a collective contribution due to limited angular resolution of their temperature map. Here, the increased angular resolution and reliable detection of both ammonia inversion lines enables a discussion on the individual contribution of the 70 μm sources to the temperature enhancements seen in the IRDC. The spatial distribution of the ammonia-derived gas kinetic temperature values is presented in Figure 4.7 for the four largest IRDC components (F2, F4, F5, and F1). The mean of the overall temperatures for all the spectra analyzed in G035.39 is 11.8 K, with the standard deviation of 2.9 K, and the corresponding statistics for individual components are listed in Table 4.1. Temperatures consistently lower than the mean (by about 2 K) are found towards the neck-like structure connecting the north and the south parts of the IRDC (left subfigure on Fig. 4.7), which is largely devoid of protostellar sources, with the exception of one 70 μm source on the western edge of the filament, previously classified as low-mass dense core (source #12 in Nguyen Luong et al. 2011). The source shows moderate temperature enhancements around it, peaking at about 15 K relative to the overall mean of the filament of 10.5 K. The excellent correspondence of the position of the 70 μm source and the localized temperature enhancement in an otherwise cold filament shows that the protostellar source is indeed embedded in the filament, ruling out the possibility of the source being a line-of-sight projection on it.

The protostellar source in the north-eastern part of the IRDC (F2 component, left panel on

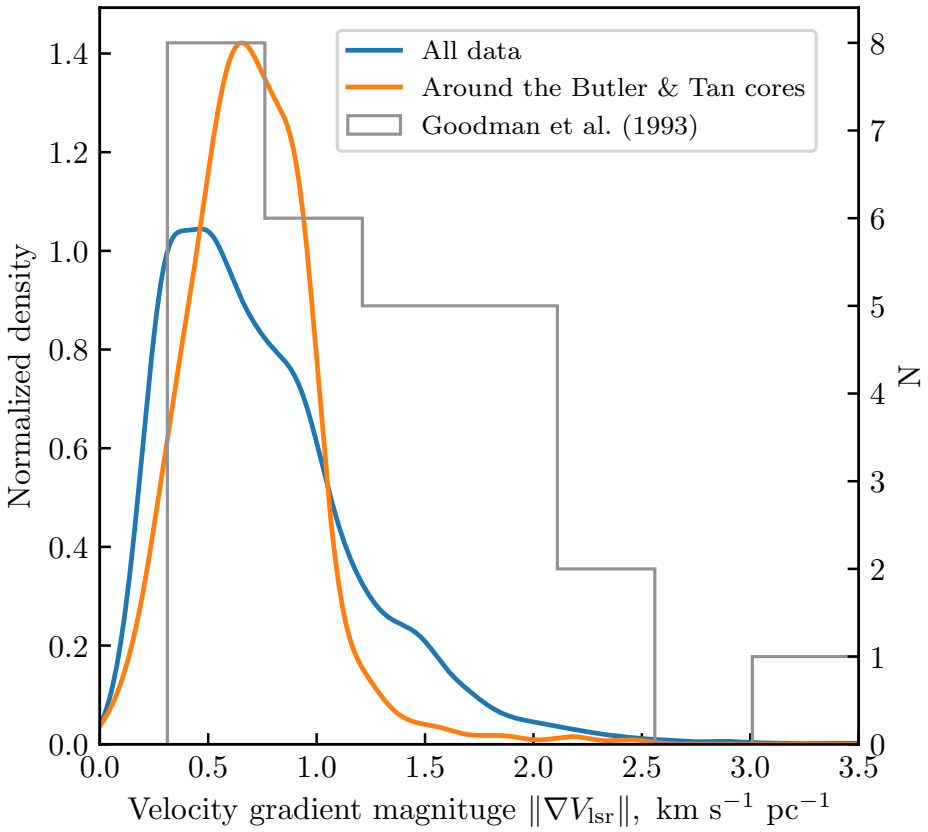

Figure 4.5 Kernel density estimate (KDE) of the velocity gradient magnitudes for all the velocity components derived. In addition to the total distribution of $\|\nabla V_{\rm lsr}\|$ shown in blue, values within three beam diameter separation from Butler & Tan (2009, 2012) cores (following the selection criteria outlined in Section 4.4.1) are shown in orange. The KDE bandwidth selection was performed following the Scott's Rule (Scott 1992). A histogram of statistically significant values (S/N $>$ 3) of velocity gradient magnitudes is shown for comparison (adapted from Goodman et al. 1993).

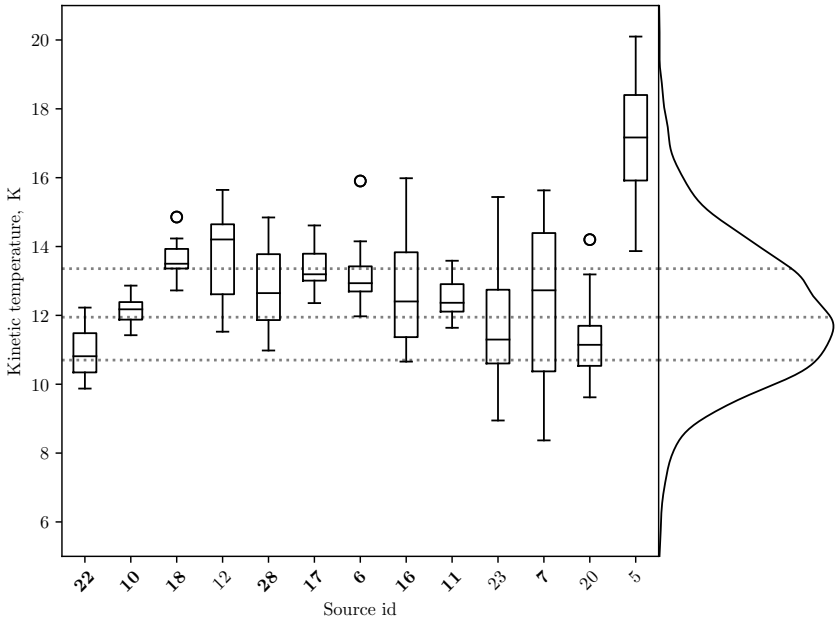

Figure 4.6 The box plots show the systematic temperature enhancements seen within one VLA beam around each of the 70 μm sources (following the selection criteria outlined in Section 4.4.1). The source number follows Nguyen Luong et al. (2011), with the low-mass dense cores labeled alongside the massive ($M > 20\ M_{\odot}$) dense cores in bold. The overall distribution (KDE, solid line) of the kinetic temperature values for all the velocity components derived, and its 25$^{\text{th}}$, 50$^{\text{th}}$, and 75$^{\text{th}}$ percentiles (dotted lines) are shown on the right-hand side of the Figure. The KDE bandwidth selection was performed following the Scott's Rule (Scott 1992).

Fig. 4.7), classified as a low-mass dense core ($9 \pm 1\ M_{\odot}$, Nguyen Luong et al. 2011), is one of the warmest regions traced with our temperature maps. It is one of the most active among the protostellar sources in the IRDC, manifesting 8-, 24-, and 70-μm point-source emission. The gas kinetic temperature increases by 8 K in its vicinity, with the peak of 20 K coinciding with the location of the 70 μm point source emission (Fig. 4.7). With the velocity centroid of the ammonia line of 45.1 km s^{-1} continuously morphing with the kinematics of the rest of the cloud (Fig. 4.4), the corresponding temperature enhancement is an argument in favor of the source being embedded in the dense filament traced with our ammonia observations. The puzzling nature of the source is emphasized by the ammonia line widths found towards it. As shown in Sokolov et al. (2018), it coincides spatially with an extended region of subsonic turbulence, and features some of the narrowest non-thermal velocity dispersions in the whole dataset.

The velocity feature at 42.5 km s^{-1}, labelled as F1 filament in our study (right panel on Fig. 4.3), forms a discontinuity in PPV space with respect to the rest of the IRDC kinematics. This blue-shifted component shows a velocity swing of about 0.5 km s^{-1} towards its center, where an extinction core (Butler & Tan 2009, 2012) is located, and a 70 μm source is found next to it (Nguyen Luong et al. 2011). The angular separation between the 70 μm source and

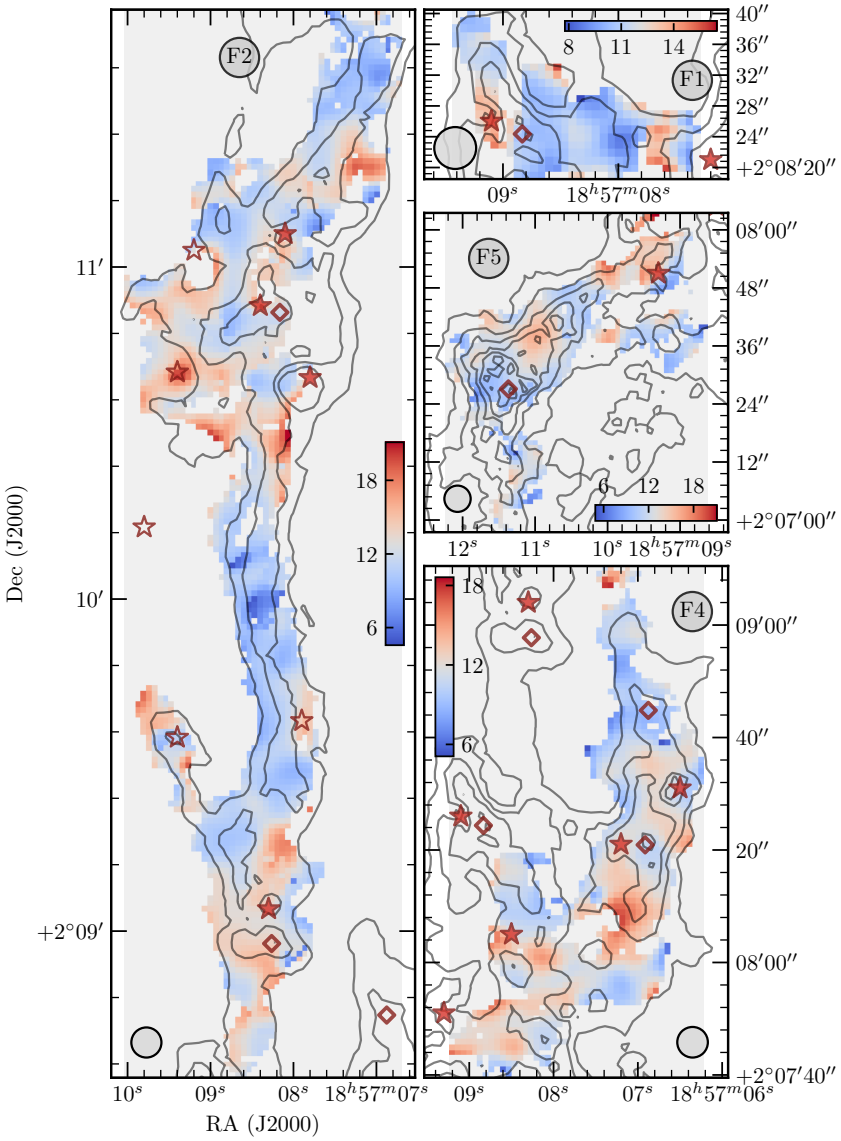

Figure 4.7 A map of derived kinetic temperature values for the biggest velocity components. The colorbar units for $T_{\rm kin}$ are in Kelvin. The layout and the source markings match those on Fig. 4.4. The overlaid contours show the extinction contours from Kainulainen & Tan (2013), ranging from A_V = 30 to 120 mag, progressing in steps of 15 mag.

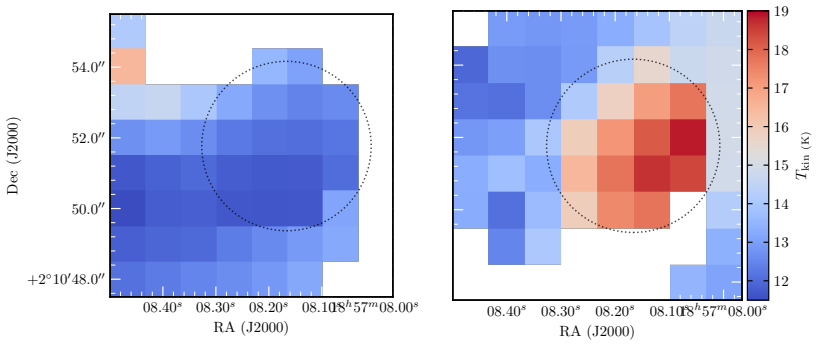

Figure 4.8 A zoom-in on the H6 core location for two overlapping line-of-sight velocity components, F2 (left panel) and F7 (right panel), showing derived kinetic temperatures. The black circle marks the fitted size of H6 core in (Butler & Tan 2012).

the Butler & Tan (2009, 2012) extinction core is 4.3″, which is smaller than both the beam of our ammonia observations as well as the 70 μm band of the SPIRE instrument. The two sources are thus likely to be related. The 70 μm source appears as a temperature enhancement in the temperature map, which suggests that star formation is ongoing in the F1 component.

We find the H6 core in the north of the cloud to be associated with two ACORNS components, F2 and F7, due to the VLA observations resolving two continuous overlapping line-of-sight regions. We report a 7 K increase in gas kinetic temperature in the F7 component, coinciding with the extinction peak of Butler & Tan (2012) and of similar size as the H6 core (Fig. 4.8). The excellent correspondence between the temperature enhancement in the F7 components and the location of the core allows us to pinpoint the H6 location in the PPV space. The exact physical nature of the temperature enhancement is less certain, and we suggest that heating from embedded protostars, either as direct radiation or in a form of unresolved outflows might stand behind the heating. Despite the temperature enhancement seen in the F7 component, we do not observe significant broadening of the line at the H6 position, and the line width, in fact, points to subsonic motions as will be seen in the next section.

Low-mass starless cores typically appear as regions of lower temperature within their parent clouds. In G035.39, the point-like 70 μm emission, signifying protostellar activity, is found in all but one among the Butler & Tan (2012) cores. Located at the peak of the extinction map in the south of the F5 filament, the H1 core appears as a cold feature in the VLA temperature map (Fig. 4.7), with a mean kinetic temperature of 10.7 K within the VLA beam, and has a complex kinematic morphology (Fig. 4.4). Recent observations by Liu et al. (2018) find evidence for a pinched magnetic field morphology towards the core, indicating that the line of sight velocity gradients on Fig. 4.4 could be an argument for accretion flows accretion flows along the filament. The mean kinetic temperature of the H1 core agrees well with that of the low-mass dense cores (e.g., 11 K for a sample of 193 cores in Rosolowsky et al. 2008a).

Table 4.2. Subsonic motions within the G035.39 velocity components.

Component ID[a]	$\mathcal{M}$[b]	$\mathcal{M} \leq 1$ fraction (%)
F2 (Blue)	1.24 ± 0.70	44
F4 (Red)	1.41 ± 0.62	32
F5 (Green)	1.42 ± 0.67	30
F1 (Orange)	0.74 ± 0.30	81
F6 (Brown)	1.54 ± 1.41	55
F3 (Purple)	1.00 ± 0.32	48
F7 (Olive)	0.54 ± 0.25	98

[a]The color labels directly correspond to the component colors on Fig. 4.3.

[b]The mean followed by the standard deviation of the values belonging to the given component.

4.5 Discussion

4.5.1 Subsonic line widths in G035.39

Turbulence, dominating molecular clouds on large scales (> 1 pc), is found to dissipate towards smaller scales (Larson 1981), allowing for bound prestellar core formation, and, ultimately, for the stellar outcome of star formation. Subsonic turbulence is observed throughout low-mass star-forming regions, and is a natural consequence of turbulent energy dissipating towards smaller scales (Kolmogorov 1941). Observationally, it is seen both as a transition to coherence on small scales (within 0.1 pc) as coherent cores (e.g., Pineda et al. 2010a, 2011a), as well as large, filament-scale subsonic regions in Taurus, Musca, Serpens South (Tafalla & Hacar 2015; Hacar et al. 2016; Friesen et al. 2016).

In massive star formation on the other hand, is thought to be governed by non-thermal motions. In IRDC G035.39 in particular, Sokolov et al. (2018) find that substantial regions of the cloud are predominantly subsonic (i.e. with sonic Mach number $\mathcal{M} \leq 1$). While the implications for the turbulence dissipation in other IRDCs are discussed in Sokolov et al. (2018), we cite the fraction of subsonic spectra identified in the ACORNS velocity components below. Table 4.2 lists the average Mach numbers, the spread of their distribution (one standard deviation), and the overall fraction of subsonic components relative to the total in each of the velocity components spanning in excess of five VLA beams. In addition, details of the Mach numbers derivation, as well as the propagation of uncertainty on $\mathcal{M}$ matching that of Sokolov et al. (2018) are included as an appendix item in Appendix 4.10.

We report no significant trends in the Mach numbers against temperature or density (either

either column density or the extinction-based mass surface density). However, we note that in two velocity components that are associated with star formation based on both the presence of 70 μm emission and kinetic temperature increase (F1 and F7; Figures 4.7, 4.8) we observe a larger fraction of subsonic motions than in any other component (Table 4.2). We suggest that future JVLA observations are needed to fully resolve the boundary over which transition to coherence in the IRDC occurs, its relation to star formation, and the degree of similarity to the transition to coherence in low-mass star-forming clouds (e.g., Goodman et al. 1998; Pineda et al. 2010a), and which could further probe smaller scale fragmentation (Pineda et al. 2015).

4.5.2 Comparison with N_2H^+

As the region mapped by Henshaw et al. (2013) with their Plateau de Bure Interferometer (PdBI) observations of N_2H^+ (1-0) line transition is fully covered in our VLA mosaic, we are well-positioned to perform a quantitative comparison of the two tracers of dense gas kinematics. Assuming that the NH_3 and N_2H^+ molecules are tracing similar gas, the turbulent (or non-thermal) components of their line widths should be equal. Figure 4.9 shows a direct comparison between the two non-thermal line widths. As the N_2H^+ molecule is heavier than NH_3, we have subtracted the thermal component from both transitions in making the figure for a more direct comparison, taking $T_{\rm kin}$ from the mean ammonia kinetic temperature for both molecules to assure the uniform comparison between the two datasets. Only the data from the commonly mapped region are shown on Fig. 4.9.

Surprisingly, we find the non-thermal line widths derived from our VLA observations to be about 30% narrower than those of the PdBI N_2H^+ (1-0) from Henshaw et al. (2014). The discrepancy would be expected if the angular resolution of the N_2H^+ map would be significantly lower than that of the VLA data, tracing more the extended, turbulent, gas. However, the spectral cube of Henshaw et al. (2014) has the effective resolution of 4″, even higher than that of our NH_3 observations (5.44″). We also note that both datasets have also had the missing flux filled in from complementary single-dish observations. In addition, the critical densities of the NH_3 (1,1) and (2,2) transitions are an order of magnitude lower than that of N_2H^+ (1-0) (Shirley 2015), so if the higher-density gas is less turbulent, a broader line width should be seen in the ammonia spectra, contrary to our results. However, ammonia can selectively trace high-density regions, as it was found to be more centrally abundant in dense cores than the chemical models predict (Caselli et al. 2017), and therefore preferentially follow material traced by N_2H^+ (1-0). Finally, the presence of magnetic fields is expected to affect the line widths of the ion species, trapping the ion molecules and narrowing their line profiles (Houde et al. 2000a), a trend opposite to what we find here. However, the phenomenon requires large turbulent flows to occur in directions misaligned with respect to the magnetic field lines, and it was not found to come into play in dark clouds primarily supported by thermal motions (Houde et al. 2000b).

Two possible explanations of the line width discrepancy are differences in hyperfine structure modelling and varying chemical differentiation. In low-mass starless cores, Tafalla et al. (2004) have found a similar discrepancy in the line widths of NH_3 and N_2H^+, and have attributed the differences in non-thermal line widths to non-LTE effects of the N_2H^+ lines (cf. Caselli et al. 1995). Because the PdBI data from Henshaw et al. (2014) were fit with an isolated hyperfine

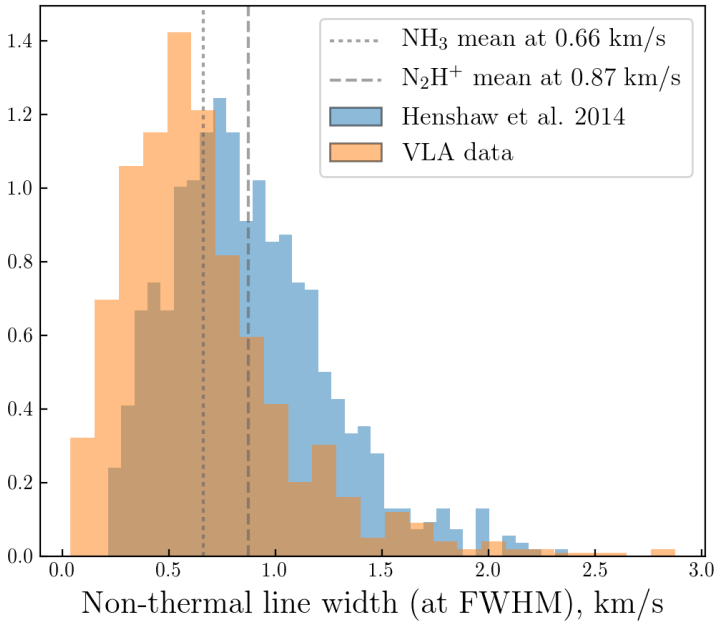

Figure 4.9 A comparison between the FWHM line widths derived in Henshaw et al. (2014) and those derived in our work. As the VLA observation mosaic covers a larger area, only the values overlapping with Henshaw et al. (2014) coverage are included.

component only, modelling it as a simple Gaussian component with $\tau \ll 1$, the relative broadening of N_2H^+ line with respect to ammonia could be an optical depth effect. However, Henshaw et al. (2014) discuss this scenario and make several arguments in favor of the isolated hyperfine transition being optically thin. Another scenario is a potential chemical differentiation between N_2H^+ and NH_3 across the IRDC, preferentially tracing regions of lower turbulence in ammonia emission. Large differences in abundance profiles of different molecules are commonly found towards low-mass starless cores (e.g., Tafalla et al. 2002; Spezzano et al. 2017) and infrared dark clouds (Feng et al. 2016). Chemical differentiation can then play a dominant role in setting the line width differences, outweighing the other arguments listed above that would favor a broader ammonia line width. This would require a significant difference in the abundance profiles for the two molecules, a difference that can be quantified by comparing the spatial distribution in the integrated intensities of NH_3 and N_2H^+. However, both tracers appear to follow the dense gas closely, showing strong linear correlations with mass surface density from Kainulainen & Tan (2013): for NH_3 (1,1) (Pearson's $r = 0.73$), NH_3 (2,2) ($r = 0.71$), and N_2H^+ (1-0) ($r \sim 0.7$, Henshaw et al. 2014). Therefore, the origin for the discrepancy remains unclear, and it is likely that higher angular resolution observations are needed to understand it.

4.5.3 Complex gas motions in G035.39

What physics processes drive the observed velocity gradients in G035.39? The multicomponent velocity field we derive in this study has a complex structure, and is likely to be driven by a combination of turbulence, cloud rotation, global gas motions, and / or gravitational influence of material condensations. To test whether the gravitational influence is the driving factor for the velocity gradients, we perform a simple analysis, taking the mass surface density of Kainulainen & Tan (2013) as a proxy for gravitational potential. In a simple picture of gas infalling into a gravitational well, one would expect an acceleration of the infalling gas towards the mass condensations forming the well, and, therefore, the observed line-of-sight velocity gradient magnitudes would be enhanced towards such clumps. However, we find no correlation between the local velocity gradient magnitude and the mass surface density from Kainulainen & Tan (2013) and, furthermore, we find no significant enhancement in the velocity gradient magnitudes towards the locations of mass surface density peaks (Fig. 4.5), indicating that the velocity field we observe has a more complex origin. In light of this, the discussion of the nature of the velocity gradients is limited to regions of IRDC with continuum sources where we see ordered velocity gradients.

In the vicinity of two massive dense cores (MDC 7 and 22) from Nguyen Luong et al. (2011), a smooth velocity gradient pattern is seen across the cores. Observationally, a pattern like this can be modelled as a solid-body rotation (Goodman et al. 1993). Assuming that the linear velocity gradient represents such a rotation, we can take its magnitude as the angular velocity of the rotating core. Both sources show similar velocity field patterns, with typical velocity gradient magnitudes of $\sim$1 km s^{-1} pc^{-1} within three VLA beams diameter: the mean value of $\|\nabla V_{\rm lsr}\|$ is 1.05 km s^{-1} pc^{-1} for MDC 22 (1.01 km s^{-1} pc^{-1} for MDC 7), while the 1-sigma spread in the $\|\nabla V_{\rm lsr}\|$ values is 0.15 km s^{-1} pc^{-1} (0.14 for MDC 7). The uncertainties on the velocity gradient magnitudes are typical of the rest of the IRDC, with mean errors of 0.03 and 0.05 km s^{-1} pc^{-1} within three VLA beam diameters of MDCs 22 and 5, respectively. Taking the deconvolved FWHM sizes of the 70 μm sources from Nguyen Luong et al. (2011) for both sources (0.12 ad 0.13 pc for MDC 7 and 22, respectively), as values for R, we arrive at the specific angular momenta of $J/M \sim 2 \times 10^{21}$ cm^2 s^{-1}, where we consider the individual differences between the two sources to be lost in the uncertainties of the calculation. The latter consideration stems from a large number of assumptions taken prior to calculation of the specific angular momentum, such as implicitly assuming a spherical radius for the cores. Furthermore, we have assumed the dimensionless parameter $p = 0.4$ for uniform density and solid-body rotation (Goodman et al. 1993) in our J/M calculation, although significant (factor of $2-3$) deviations are expected for turbulent, centrally concentrated, cores (Burkert & Bodenheimer 2000). Finally, our implicit interpretation of the physical nature of the velocity gradients can be biased as well. The observed ammonia kinematics trace the entire IRDC, not just its cores, and the velocity gradient vector field we recover with the moving least squares is sensitive not only to $\sim$0.1 pc core motions but also to gas motions on larger scales. The seemingly ordered velocity field around MDC 7 and 22 does not necessarily represent rotation of the cores. It could be a manifestation of the larger, filamentary, rotation, an effect of ordered gas flows on larger scales, or turbulent component at larger scale. As low-mass dense cores have been found to have gradient directions that differ

from the gradients at larger, cloud, scales (Barranco & Goodman 1998; Punanova et al. 2018), the motions we see could be dominated by these large scales. Whether this is indeed the case would have to be verified with higher-angular resolution observations of dense gas tracers.

Despite the uncertainties discussed above, it is interesting to see how the specific angular momentum compares to the low-mass star formation. In low-mass star forming cores, rotational motions have been shown to be insufficiently strong to provide significant stabilizing support (Caselli et al. 2002a). Compared to their lower-mass counterparts, cores in massive IRDCs are denser and are born in a relatively more pressurised and turbulent environment. If the origin of angular momentum of the star-forming material is related to the degree of non-thermal motions, the specific angular momentum inherited by the IRDC cores could be boosted (cf. Tatematsu et al. 2016, who find systematically larger J/M values in Orion A cores). Despite this line of reasoning, in IRDC G035.39 we arrive at values of J/M that are fairly typical of the low-mass dense cores (e.g., Crapsi et al. 2007), and align well with the specific angular momentum-size relation in (Goodman et al. 1993). The agreement with the low-mass core J/M is consistent with our previous results, where we have shown that G035.39 has smaller degree of non-thermal motions (Sokolov et al. 2018) than other IRDCs, and implies that, given the larger mass of the IRDC cores, the rational support is even less dynamically important than for the low-mass dense cores.

4.6 Conclusions

Our main results can be summarized as follows.

1. In the first interferometric mapping of the entire IRDC G035.39, we have mapped the NH_3 (1,1) and (2,2) inversion transitions the cloud, combining the VLA and GBT observations.

2. Our data reveal the convoluted kinematics in the cloud, bridging the cloud and core scales. We identify seven principal structures in position-position-velocity space, and find velocity gradients within them that are comparable to the dynamics of the low-mass star-forming cores imaged with similar resolution.

3. Contrary to expectations from theoretical observational perspectives, we find a systematic line width difference between NH_3 and N_2H^+, with ammonia line width being about 30% smaller, a discrepancy also found towards low-mass dense cores.

4. We construct a gas temperature map for the IRDC, with the highest angular resolution available to date for this source and, wherever deemed significant, for separate line of sight velocity components. We report significant heating from the embedded protostellar sources that has not been seen individually from previous studies of gas and dust temperature in G035.39. The temperature of the seemingly starless core in the IRDC is typical for low-mass dense core regime.

5. We have identified a number of sources, of both protostellar and starless nature, that exhibit complex gas motions around them. A few of these sources show ordered velocity field in

their vicinity, and appear to influence the dynamics of the gas around them. For the selected sources, we calculate the corresponding specific angular momentum, assuming solid-body rotation of a uniform-density core, to be about 2×10^{21} cm^2 s^{-1}, similar to that of the low-mass dense cores.

VS, JEP, and PC acknowledge the support from the European Research Council (ERC; project PALs 320620). KW is supported by grant WA3628-1/1 of the German Research Foundation (DFG) through the priority program 1573 (”Physics of the Interstellar Medium”). JCT acknowledges NASA grant 14-ADAP14-0135. IJ-S acknowledges the financial support received from the STFC through an Ernest Rutherford Fellowship (proposal number ST/L004801/2). This publication made use of ACORNS, a Python package used to link PPV data.

4.7 VLA and GBT data combination strategies

This section expands on the subtleties of the deconvolution process we use to arrive at the final combined VLA+GBT spectral cubes. The CLEAN algorithm (Högbom 1974) deconvolves images by representing them as a number of point sources, iteratively subtracting fractions of dirty beam from the peak intensity regions, until the stopping threshold has been reached. While the method is best-suited for collections of bright point sources, imaging fainter and more extended emission is not a trivial task. Using CLEAN to recover extended emission with surface brightness comparable to that of noise artifacts would often lead only to an amplification of the noise level in the resultant image, hence a careful approach to the problem is needed in such cases. A common strategy to recover dim extended emission involves restricting the CLEAN algorithm by a spatial mask where significant level of emission is known to exist, thus preventing iterations of CLEAN to run on noise features. The overall logic behind the procedure we use to image ammonia data in G035.39 is similar, but occurs in few steps - we rely on the knowledge of the small-scale emission first to set up initial CLEAN mask, subsequently gradually extending emission-based CLEAN masks into the deconvolution process as it progresses. This approach assures the certainty of the extended emission cleaning and will be shown to be more reliable than a simpler version of it. A summarized description of this procedure was presented in Sokolov et al. (2018) as well as in Section §4.3.

As a first step in the imaging process we deconvolve the VLA-only visibilities on their own, reliably targeting the spatial distribution compact emission. To do this, we use the multi-scale generalization of the CLEAN algorithm (Cornwell 2008) implemented within CASA (McMullin et al. 2007) as TCLEAN task, using Briggs weighting and the robust parameter of 0.5. In three consequent runs of TCLEAN, we progressively clean the emission down to multiples of the noise level (5σ, 3σ, and, finally, down to 1σ) for both NH_3 (1,1) and (2,2) spectral cubes. For the first run of the algorithm, the CLEAN mask is calculated[2] for each spectral channel based on a dirty

[2]The CLEAN mask is calculated as follows. For every channel of the spectral cube, we select an intensity threshold, and create a mask based on it. The mask then undergoes a binary closing operation with a structural element that resembles a circularized VLA beam. Additionally, all the elements of the mask that have fewer than three beams worth of pixels are flagged out to disallow noise features from propagating into the CLEAN mask.

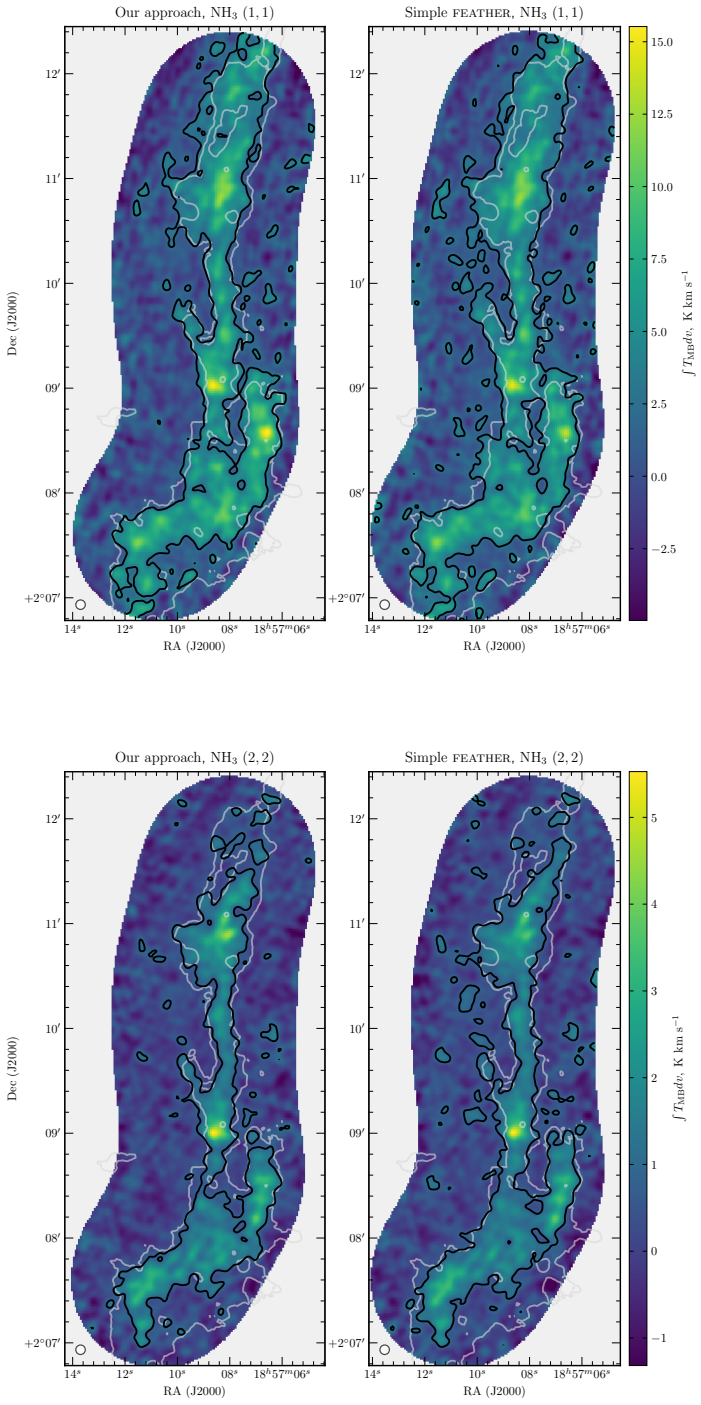

Figure 4.10 Integrated intensities of the NH_3 (1,1) and (2,2) lines for the two imaging setups we consider: the chosen method is shown on the left, while a simpler feathered CLEAN run results on on the right. Solid black contours mark SNR= 3 detection in the integrated intensity. Overlaid in white is the mid-infrared extinction contour at $A_V = 25$ mag, arbitrarily chosen to represent the cloud border (Kainulainen & Tan 2013).

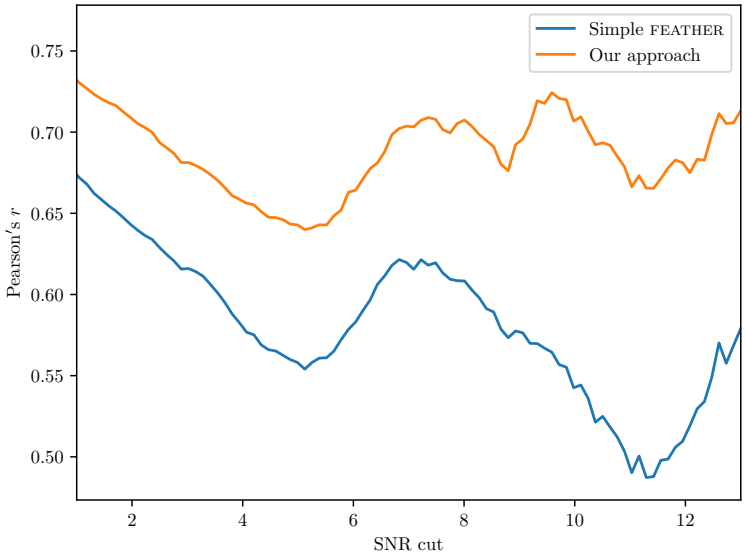

Figure 4.11 Pearson's r correlation coefficient between the integrated intensities of the (1,1) and (2,2) lines. The deconvolution setup we use in this work (in orange) results in a higher correlation between independent data cubes than a more simple approach (in blue), indicating that our approach is more reliable.

image (with a 3σ noise level threshold). For the subsequent TCLEAN runs, we expand the clean mask by using the output image from the previous run at the 2σ noise level threshold.

Secondly, we feather the cleaned VLA images with the GBT data, using FEATHER task within the CASA package. We found the default settings for the dish diameter (~100 m) and the default low resolution scale factor of unity to produce reasonable results. Prior to feathering, all the GBT spectra are smoothed with a Gaussian kernel to 0.2 km s^{-1} spectral resolution of the VLA data, and interpolated onto the spatial map used in the VLA imaging ($1''$ pixels in 240 by 384 grid). Cubic interpolation was used, as the nearest neighbor interpolation was found to produce artifacts resulting from a large relative size of the GBT pixels (~$10''$).While these data are already sufficient for conducting scientific analyses, we found that they can be significantly improved through a procedure outlined below. In order to demonstrate the improvement, the feathered data will be compared with the final imaging results in the text concluding this section.

Finally, armed with the reliable information about the extended emission spatial distribution in the feathered spectral cubes, we perform a final deconvolution of the VLA visibilities. For this final imaging step, we use the rescaled GBT images as a starting model. The multi-scale CLEAN proceeds in the same fashion as in the previous runs, with the exception of the initial clean mask, which is now being calculated on the feathered cube from step two.

Given the inherently uncertain nature of the VLA imaging process, it is anything but trivial to judge the degree of improvement in final image quality. While overall the results are similar to a simpler feathering approach, there are important differences that make us prefer the new method. A comparison of the integrated intensities between the new and old imaging results, overlaid with significantly detected signal-to-noise ratio (SNR = 3) contours, is shown on Figure 4.10. While the overall morphology of the two approaches is similar, the method we use results in fewer spurious noise-driven features. The latter claim is justified through both fewer isolated SNR > 3 closed contours off the main filament of G035.39 as well as the signal detection having a closer alignment to the mid-infrared extinction contours, shown for comparison on Fig. 4.10.

To quantify the degree of improvement, we use the fact the (1,1) and (2,2) lines of NH_3 were imaged independently in separate sessions. Therefore, if we assume that the integrated emission of the two lines originates from the same physical region, tracing the dense cold gas making up the IRDC, we can use the correlation between the two as a proxy for testing how well the deconvolution has reconstructed the ammonia emission. Note that while due to the temperature differences across G035.39 will reduce the overall correlation, such a bias is expected to come into play for both the imaging setups. Figure 4.11 shows a comparison of how the correlation in integrated intensities varies for the different SNR cuts (i.e. on the y-axis we check for correlation of all pixels with SNR > x). While significant ($r > 0.5$) linear correlation is present between (1,1) and (2,2) integrated intensities for all the SNR ranges, the correlation is consistently higher for the imaging setup we use in this work.

For the final, TCLEAN run, the binary closing operation uses a three-channels-wide structural element. This helps to extend the mask from neighboring channels, making it more reliable and continuous - e.g., the emission not deemed significant enough would still be included in the CLEAN mask if its neighboring channels have emission above the threshold level.

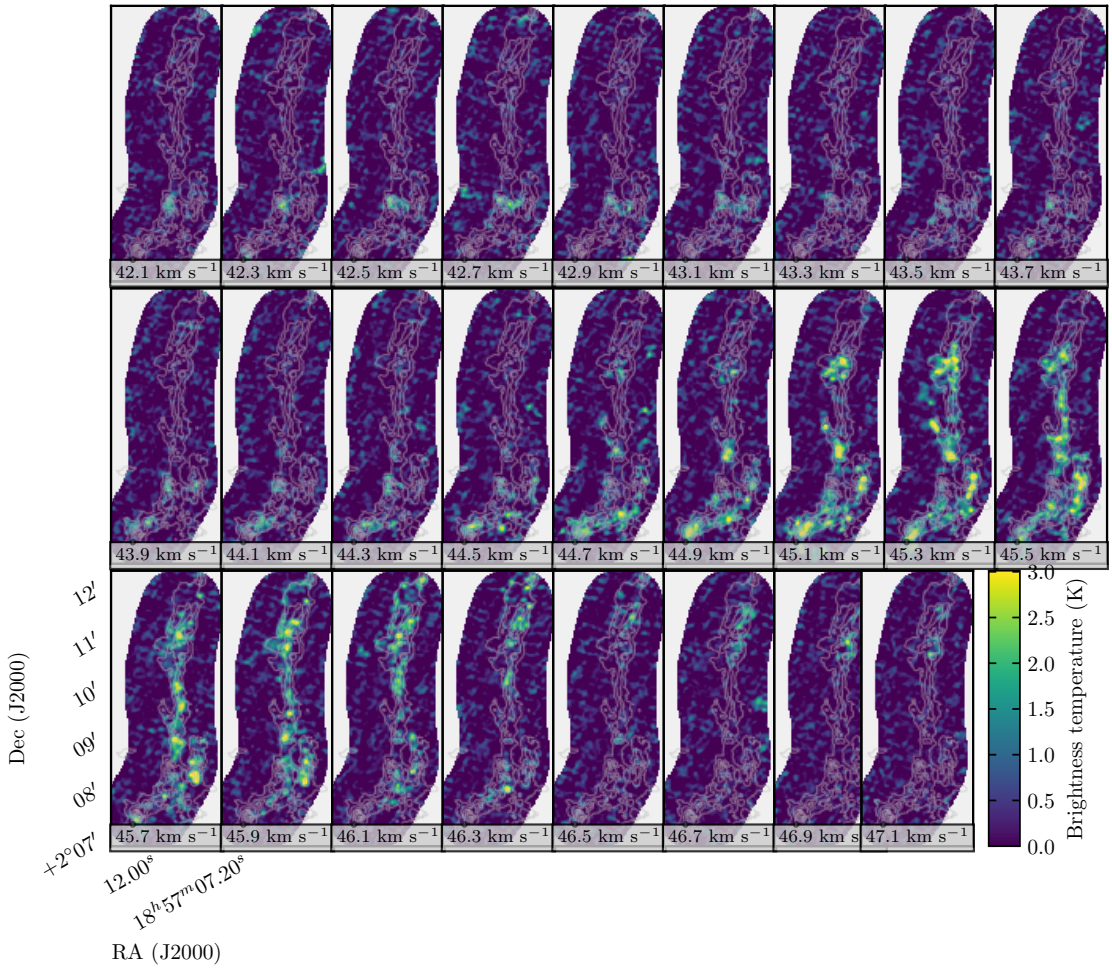

Figure 4.12 Channel maps of the NH_3 (2,2) line for the IRDC G035.39. The spatial coordinate grid, overlapped contours, and the velocity ranges for each channel are identical to those of Figure 4.1.

4.8 Channel maps of the NH_3 (2,2) line

Channel maps for the NH_3 (2,2) line, presented in the same manner as the NH_3 (1,1) channel maps in the main text (Fig. 4.1), are presented in Figure 4.12. Overall both the integrated intensity structure and the signal to noise levels agree with that of the NH_3 (1,1) channel maps.

4.9 Relaxed censoring PPV-structures

The strict censoring approach (§4.3.2) we take when deriving the PPV structure of the cloud could selectively filter out weaker secondary line of sight components. If a relaxed censoring strategy is used instead, the PPV structure would naturally result in more line-of-sight com-

ponents. Because we require both NH_3 lines to be significantly detected to derive the kinetic temperature and constrain the column density, the relaxed censoring is not considered as a reliable approach throughout this paper. Nonetheless, if only the kinematic structure of the IRDC is to be discussed, the relaxed censoring could better capture the velocity patterns in its filaments. In this context, if we consider either (1,1) or (2,2) line detection to constrain the gas kinematics, how would this change the basic kinematic properties we derive throughout this work?

For the same ACORNS clustering criteria used, the hierarchical procedure outlined in §4.4.1 results in more distinct velocity structures: twenty four components, of which ten exceed the collective area of five synthesized VLA beams. Figure 4.13 shows the ACORNS components identified in a manner similar to Fig. 4.3. The velocity gradient magnitude distribution, if derived in the same manner as in §4.4.2, has a mean value of 0.72 km s^{-1} pc^{-1}, close to 0.75 obtained in §4.4.2. The spread in the distributions of velocity gradient magnitudes is similar as well: with standard deviations of 0.42 and 0.45 km s^{-1} pc^{-1} for relaxed and strict censoring strategies, respectively.

Given the similarity of the derived kinematic properties, we argue that the subsequent discussion on IRDC kinematics in §4.5.3, namely, on the specific angular momenta, is unaffected by the method chosen to arrive at the full PPV structure of G035.39.

4.10 Non-thermal line widths and propagation of uncertainties in Mach numbers

To derive the degree of non-thermal gas motions and gas turbulence in G035.39 from the ammonia data, we use the following relations. Firstly, accounting for the channel width broadening effects, we subtract the channel width from the observed full width at half-max maximum of the line:

$$\Delta V_{FWHM} = \sqrt{{\Delta V_{\rm obs}}^2 - {\Delta V_{\rm chan}}^2},$$

where $\Delta V_{\rm obs}$ is the fitted line width from the observed line profile and $\Delta V_{\rm chan}$ is taken to be the spectral resolution of VLA at 0.2 km s^{-1}. To find the degree of non-thermal gas motions, we then remove the component caused by the thermal broadening of the line, obtaining the non-thermal velocity dispersion from the line width:

$$\sigma_{\rm nt} = \sqrt{\frac{{\Delta V_{\rm obs}}^2}{8 \ln 2} - \frac{k_{\rm B} T_{\rm kin}}{m_{\rm NH_3}}},$$

where $m_{\rm NH_3} = 17\ m_{\rm H}$ is the molecular weight of the ammonia molecule.

A useful way to quantify the degree of the non-thermal motions in the gas is to compare those against the local sonic gas speed $c_{\rm s} \equiv \sqrt{\frac{k_{\rm B} T_{\rm kin}}{m_{\rm gas}}}$, where $m_{\rm gas}$, the average mass of the particle in the gas medium, is taken to be 2.33 a.m.u. Following this, a sonic Mach number is computed as the ratio of the two quantities: $\mathcal{M} \equiv \sigma_{\rm nt}/c_{\rm s}$.

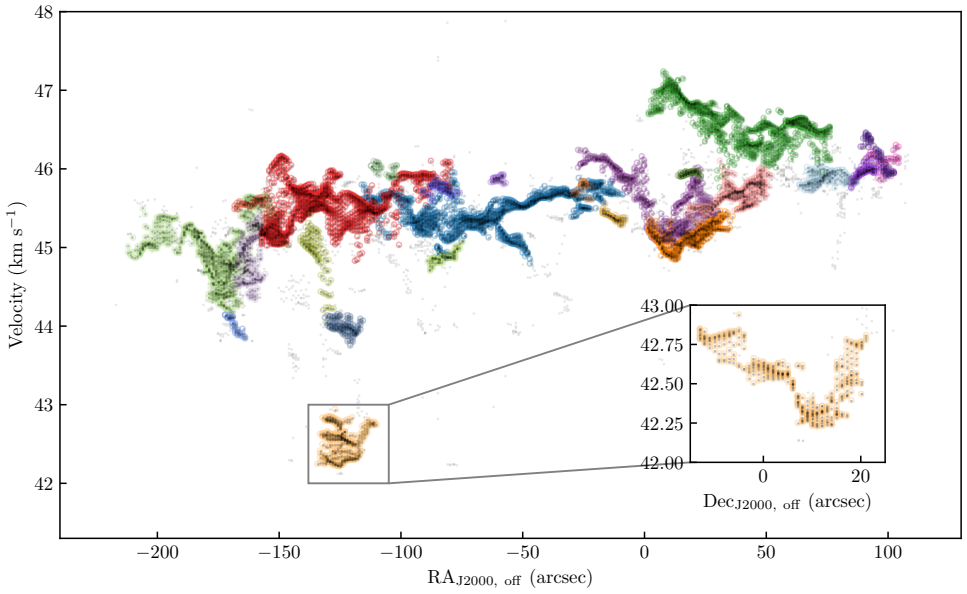

Figure 4.13 A PPV-diagram of the fitted velocity components within IRDC G035.39 along the Right Ascension projection. The coordinates are given in arcsecond offset relative to the α(J2000) = 18h57m08s, δ(J2000) = +2°10′30″ coordinate. All the data are plotted in black, similarly to Fig. 4.2, and individual velocity components are marked in different colors. The data not found to be associated with any clusters are plotted in gray. The figure shows the clustering obtained with the relxed masking criteria (introduced in §4.3.2). In addition to the R.A. projection, a projeciton along Dec. is shown in the inset axis for the F1 filament.

In order to enable a statistically sound discussion on the Mach numbers, one needs to first estimate the uncertainty on their values. In our analyses, we assume the uncertainty to come from two factors: the temperature of the gas, used to calculate the thermal contribution to line width and the sonic sound speed in the medium, and the error on the line width itself. Both errors are estimated within PYSPECKIT package, which provides one-sigma uncertainties on $T_{\rm kin}$ and σ. Assuming these uncertainties to be uncorrelated, we propagate the errors as follows:

$$\sigma_{\mathcal{M}} = \sqrt{{\sigma_{\sigma_{\rm obs}}}^2 \left[\frac{\partial \mathcal{M}}{\partial \sigma_{\rm obs}}\right]^2 + {\sigma_{T_{\rm kin}}}^2 \left[\frac{\partial \mathcal{M}}{\partial T_{\rm kin}}\right]^2}, \tag{4.1}$$

where the notations $\sigma_{T_{\rm kin}}$ and $\sigma_{\sigma_{\rm obs}}$ are the uncertainties on the gas kinetic temperatures and observed velocity dispersion, respectively.

Substituting appropriate terms into Equation 4.1, we arrive at the following expression:

$$\sigma_{\mathcal{M}} = \frac{\sqrt{m_{\rm gas} m_{\rm NH_3}}}{2} \sqrt{\frac{{\sigma_{T_{\rm kin}}}^2 ({\sigma_{\rm obs}}^2 - {\sigma_{\rm chan}}^2)^2 + 4 {\sigma_{\sigma_{\rm obs}}}^2 {\sigma_{\rm obs}}^2 {T_{\rm kin}}^2}{k_{\rm B} {T_{\rm kin}}^3 (m_{\rm NH_3} ({\sigma_{\rm obs}}^2 - {\sigma_{\rm chan}}^2) - k_{\rm B} T_{\rm kin})}}, \tag{4.2}$$

where the terms $\sigma_{\rm chan} = \Delta V_{\rm chan} / \sqrt{8 \ln 2}$ and $\sigma_{\rm obs} = \Delta V_{\rm obs} / \sqrt{8 \ln 2}$ are introduced for clarity.

The expression above is used to quantify the uncertainties on the $\mathcal{M}$ values throughout this work (where applicable), as well as in Sokolov et al. (2018).

Chapter 5

Future Work and Outlook

5.1 Summary and Future Work

This work presented analyses of observations towards IRDC G035.39–00.33, previously found to be an excellent target to probe the initial conditions for high-mass star formation. Below the summary of preceding chapters is given, and interesting future prospects for IRDC and high-mass star formation are outlined. With the large-scale GBT observations of ammonia inversion transitions and the complementary archival *Herschel* photometric data, a quantitative comparison between the two temperature estimating methods is made. Without careful modelling of the background and foreground emission, the conventional method of deriving dust temperature is shown not only to systematically overestimate the IRDC temperatures by $2 - 3$ K, but also conceals signs of protostellar heating of the core envelopes. What does this entail for the future studies of IRDCs? Because the spectral line surveys that can reliably measure the gas temperature are time-consuming, far-infrared surveys are commonly used in their place for large-scale temperature measurements of cold clouds. Given the richness of the available *Herschel* Galactic plane surveys, any systematic search for starless core candidates through far-infrared emission would benefit from tighter constraints of the spatial temperature distribution, which should take the line-of-sight contamination into account. Additionally, any chemical modelling of the infrared dark clouds has to take the systematics above into account, because the chemical reaction rates are highly dependant on the temperature, making the $2 - 3$ K bias found significant enough to account for.

On smaller scales, the combined single-dish and interferometric observations reveal a surprising insight. Compared to other surveys of IRDCs conducted at the same facilities, G035.39 exhibits levels of turbulence lower than other infrared dark clouds. Is G035.39 an oddball in an otherwise established and unshaken picture of massive star formation that always occurs in a highly turbulent medium, or is it one of the first pieces of evidence signalling that massive star formation undergoes through a quiescent stage, more similar to the low-mass star forming clouds than previously thought? The follow-up surveys of IRDCs, conducted with high frequency resolution and sensitivity, should be able to give an answer to that question. However, an argument for the lower non-thermal motions prevailing in IRDCs can be found in other recent studies as

well as recent ALMA observations towards the Orion Integral Filament, which resolve it into collections of subsonic fiber-like structures. Within G035.39 itself, more observations are needed to investigate the boundary over which the gas kinematics becomes subsonic, and to determine if a phenomenon similar to transition to coherence, found in low-mass dense cores, plays a role in the IRDC cores.

Finally, the similarity of IRDC G035.39–00.33 to the low-mass star forming regimes does not apply only to the non-thermal motion magnitude. Although most of the dense extinction cores can be associated with the mid-infrared emission (likely of protostellar origin), the temperature of the core with the highest extinction and no mid-infrared emission closely resembles that of the low-mass starless cores. Similarly, the kinematics of the IRDC resembles the low-mass dense cores closely, with similar velocity gradient magnitudes and specific angular momenta of the cores if solid-body core rotation is assumed. Observations of high-mass protostellar objects which aim to probe the initial conditions of massive star formation are naturally biased by energetic feedback processes from the embedded massive YSOs. Dedicated future surveys of dense gas kinematics of sources not yet exhibiting signs of disruptive feedback, conducted with high spectral and angular resolution, are needed to further evaluate the extent to which degree the low- and high-mass star-forming conditions are similar.

5.2 Outlook

The ongoing studies with the ALMA interferometer are beginning to reveal the complexity of high-mass star formation. However, there is still much to be learned with both state-of-the-art facilities like ALMA and future missions such as Square Kilometer Array (SKA) and James Webb Space Telescope (JWST). The Turbulent Core model predicts that massive stars form from short-lived massive starless cores, supported by turbulence and magnetic field and confined by external pressures, yet there is currently no conclusive evidence as to whether this class of objects exists. The ongoing search for massive prestellar cores through appropriate chemical tracers, currently actively underway (Kong et al. 2017a), will eventually help to ascertain the degree to which turbulent core accretion model comes into play when forming high-mass stars. As massive starless cores are challenging to detect with common chemical tracers due to the depletion chemistry, the development of the chemical models of IRDCs must go hand in hand with the observational search for the elusive massive starless cores. In addition to the ALMA results of the high density molecular tracers, there is some prospect in developing high-resolution extinction mapping techniques which do not suffer from saturation effects (currently at $\sim$100 A_V for mid-infrared methods).

Currently there is a lack of systematic large-scale ALMA programs aiming to establish a large statistical sample of massive protostellar objects and trace their evolution. The extraordinary sensitivity of ALMA allows to trace the continuum emission from cold dust in IRDCs with unprecedented precision (e.g., Kong et al. 2018), and high-resolution studies of populations of dense cores, complete down to the thermal Jeans mass, would help to constrain the relation between the IMF and the core mass function (CMF). As the competing camps of high-mass star formation theories have different predictions as to the origin of the IMF, such surveys could prove

to be decisive in explaining the long-standing problem of how massive star birth is tied to cluster formation.

The smaller-scale structure of high-mass star formation is also beginning to emerge driven by ALMA observations. Despite the potential importance accretion disks play in channelling the material onto massive stars, the observational evidence for their existence is scarce. High-resolution ALMA observations allow to probe the structure and fragmentation of disk-like structure around high-mass stars, and to directly compare their rotation and accretion rates with the theoretical models, simulations, and the well-studied low-mass protostars. In addition to disks, dedicated dense gas kinematic ALMA studies will reveal the role in filamentary accretion in high-mass star formation.

The current high-resolution studies with ALMA trace the low-energy tail of the SED, focusing on continuum emission from dust contained in cold molecular cores. Up to date, there were no matching observations of complementary warm dust components. Although the two largest mid- and far-infrared space telescopes ever flown, Spitzer and Herschel Space Observatories, have pushed the boundaries of our understanding of how stars and molecular clouds form, they did not have the angular resolution and sensitivity to directly complement the capabilities of ALMA in conducting protostellar observations. The upcoming JWST space mission, currently scheduled to launch in 2021 after several delays, will revolutionize the fields of star and planet formation, providing sensitivity enough to image young protostars and protoplanetary systems with an angular resolution comparable to that of ALMA. In massive star formation, the sensitivity of JWST would allow to detect the existence of massive prestellar cores, helping to distinguish between the two major competing theories of massive star formation, competitive accretion and turbulent core models. Furthermore, establishing the density profiles of massive cores would further improve our understanding of how high-mass star cores form and evolve. The measurements of energetic phenomena driven by young massive protostars, like outflows, jets, and accretion disks, will constrain the accretion rates on the growing massive stars, providing crucial insight to simulations and theoretical models, which currently have a large spread in predicted accretion rates. In addition, large statistical studies of massive protostellar objects with JWST will further help to distinguish between the theoretical models, which predict different levels of relative outflow alignment in protoclusters. In addition, its spectroscopic capabilities would allow the direct detection of H_2 emission from the cooling gas heated by outflows and shocks. This could potentially help probe the scenarios of star formation triggered by nearby supernova remnants.

5.3 The Challenges of 21st Century Radio Astronomy

Modern astronomy is increasingly tied to ever larger data volumes. Modern interferometers like ALMA can send up to 512 MB/s per baseline from the correlators, and future observatories like the SKA will have a stunning total data rate of ~20 Tb/s (Norris 2011). This rapid increase in data volumes delivered not only requires the use of state-of-the-art data transfer and storage technology on par with large IT companies (e.g., SKA Pathfinder mission would need petabytes of storage space per year), but also highlights the increasing complexity of the data astronomers

end up with, and the need for developing tools for their automatic processing. Larger observational bandwidths allow to obtain simultaneous mapping of various molecular lines, and the sheer wealth of the information in ALMA line surveys is often overwhelming. Furthermore, more and more archival data are being put in the public domain, and the fraction of archival publications is steadily rising (White et al. 2009).

The increasing data volumes will find modern astronomers unprepared and swept away by the data flood unless a considerable effort is spent into developing modern analysis tools that take full advantage of the exponential growth of computational power available. As an example relevant to the topic of this thesis, let's consider the kinematics of filamentary IRDCs and one specific numerical challenge relevant to it. The geometry of filamentary molecular clouds is likely to result in a spectral identification from several individual spectral components, each with individual radial velocity yet projected together on the same patch of the sky. Historically, these secondary velocity components were often fit "by eye", yet not only this practice is outdated due to the sheer number of spectra in modern datasets but it is also not statistically sound in cases where the components partially overlap or one of the components is comparable to the noise level. This creates a problem, as the traditionally used gradient-descent-like methods break down in presence of multiple local maxima of the spectral likelihood functions. While providing a well-informed initial starting point on the likelihood surface mitigates this problem, it typically requires some form of increased human interaction what would ultimately slow down the scientific inference into the dataset in question. To overcome this issue, novel methods that improve the initial values of gradient descent methods, or alternative, global estimators like genetic or differential evolution algorithms, or, alternatively, Bayesian inference, coupled with statistically justified insight into the model selection between different number of components, is needed. As of this date, a simple-sounding question of how to reliably fit multiple velocity components remains an open one in star formation community.

5.4 Final Remarks

In this work, an in-depth analysis of one of the best candidates for the earliest stages of massive star formation, IRDC G035.39, is presented. The research presented here improves on the state-of-the-art knowledge of IRDCs and provides useful insights into theories and simulations of high-mass star formation. Nonetheless, there is still much to be learned about the infrared dark clouds and their relation to high-mass and cluster formation. Recent and future facilities, together with modern computational data analysis methods, will help to provide further insight into the early stages of massive star formation.

Bibliography

Alexander, S. 1852, AJ, 2, 95, doi: 10.1086/100227

Andrae, R., Fouesneau, M., Creevey, O., et al. 2018, ArXiv e-prints, arXiv:1804.09374. https://arxiv.org/abs/1804.09374

André, P. 1995, Ap&SS, 224, 29, doi: 10.1007/BF00667817

André, P., Di Francesco, J., Ward-Thompson, D., et al. 2014, in Protostars and Planets VI, 27

Andre, P., Ward-Thompson, D., & Barsony, M. 1993, ApJ, 406, 122, doi: 10.1086/172425

André, P., Men'shchikov, A., Bontemps, S., et al. 2010, A&A, 518, L102, doi: 10.1051/0004-6361/201014666

Barnard, E. E. 1919, ApJ, 49, 1, doi: 10.1086/142439

Barnes, A. T., Henshaw, J. D., Caselli, P., et al. 2018, MNRAS, 475, 5268, doi: 10.1093/mnras/sty173

Barnes, A. T., Kong, S., Tan, J. C., et al. 2016, MNRAS, 458, 1990, doi: 10.1093/mnras/stw403

Barranco, J. A., & Goodman, A. A. 1998, ApJ, 504, 207, doi: 10.1086/306044

Battersby, C., Bally, J., Ginsburg, A., et al. 2011, A&A, 535, A128, doi: 10.1051/0004-6361/201116559

Benson, P. J., & Myers, P. C. 1989, ApJS, 71, 89, doi: 10.1086/191365

Beuther, H., Churchwell, E. B., McKee, C. F., & Tan, J. C. 2007, Protostars and Planets V, 165

Beuther, H., Schilke, P., Menten, K. M., et al. 2002a, ApJ, 566, 945, doi: 10.1086/338334

Beuther, H., Schilke, P., Sridharan, T. K., et al. 2002b, A&A, 383, 892, doi: 10.1051/0004-6361:20011808

Beuther, H., Sridharan, T. K., & Saito, M. 2005, ApJ, 634, L185, doi: 10.1086/498867

Beuther, H., Soler, J., Vlemmings, W., et al. 2018, ArXiv e-prints. https://arxiv.org/abs/1802.00005

Bigiel, F., Leroy, A., Walter, F., et al. 2008, AJ, 136, 2846, doi: 10.1088/0004-6256/136/6/2846

Bihr, S., Beuther, H., Linz, H., et al. 2015, A&A, 579, A51, doi: 10.1051/0004-6361/201321269

Blitz, L., & Shu, F. H. 1980, ApJ, 238, 148, doi: 10.1086/157968

Bonnell, I. A., & Bate, M. R. 2005, MNRAS, 362, 915, doi: 10.1111/j.1365-2966.2005.09360.x

Bonnell, I. A., Bate, M. R., & Zinnecker, H. 1998, MNRAS, 298, 93, doi: 10.1046/j.1365-8711.1998.01590.x

Bonnell, I. A., Larson, R. B., & Zinnecker, H. 2007, in Protostars and Planets V, 149

Bonnell, I. A., Vine, S. G., & Bate, M. R. 2004, MNRAS, 349, 735, doi: 10.1111/j.1365-2966.2004.07543.x

Boulares, A., & Cox, D. P. 1990, ApJ, 365, 544, doi: 10.1086/169509

Burkert, A., & Bodenheimer, P. 2000, ApJ, 543, 822, doi: 10.1086/317122

Butler, M. J., & Tan, J. C. 2009, ApJ, 696, 484, doi: 10.1088/0004-637X/696/1/484

—. 2012, ApJ, 754, 5, doi: 10.1088/0004-637X/754/1/5

Carey, S. J., Clark, F. O., Egan, M. P., et al. 1998, ApJ, 508, 721, doi: 10.1086/306438

Carey, S. J., Feldman, P. A., Redman, R. O., et al. 2000, ApJ, 543, L157, doi: 10.1086/317270

Caselli, P., Benson, P. J., Myers, P. C., & Tafalla, M. 2002a, ApJ, 572, 238, doi: 10.1086/340195

Caselli, P., & Myers, P. C. 1995, ApJ, 446, 665, doi: 10.1086/175825

Caselli, P., Myers, P. C., & Thaddeus, P. 1995, ApJ, 455, L77, doi: 10.1086/309805

Caselli, P., Walmsley, C. M., Zucconi, A., et al. 2002b, ApJ, 565, 331, doi: 10.1086/324301

Caselli, P., Bizzocchi, L., Keto, E., et al. 2017, A&A, 603, L1, doi: 10.1051/0004-6361/201731121

Chabrier, G. 2003, Publications of the Astronomical Society of the Pacific, 115, 763, doi: 10.1086/376392

Chambers, E. T., Jackson, J. M., Rathborne, J. M., & Simon, R. 2009, ApJS, 181, 360, doi: 10.1088/0067-0049/181/2/360

Chandrasekhar, S., & Fermi, E. 1953, ApJ, 118, 116, doi: 10.1086/145732

Cheung, A. C., Rank, D. M., Townes, C. H., Thornton, D. D., & Welch, W. J. 1968, Physical Review Letters, 21, 1701, doi: 10.1103/PhysRevLett.21.1701

Chira, R.-A., Beuther, H., Linz, H., et al. 2013, A&A, 552, A40, doi: 10.1051/0004-6361/201219567

Churchwell, E., Babler, B. L., Meade, M. R., et al. 2009, Publications of the Astronomical Society of the Pacific, 121, 213, doi: 10.1086/597811

Cornwell, T. J. 2008, IEEE Journal of Selected Topics in Signal Processing, 2, 793, doi: 10.1109/JSTSP.2008.2006388

Crapsi, A., Caselli, P., Walmsley, M. C., & Tafalla, M. 2007, A&A, 470, 221, doi: 10.1051/0004-6361:20077613

Crapsi, A., van Dishoeck, E. F., Hogerheijde, M. R., Pontoppidan, K. M., & Dullemond, C. P. 2008, A&A, 486, 245, doi: 10.1051/0004-6361:20078589

Dame, T. M., Ungerechts, H., Cohen, R. S., et al. 1987, ApJ, 322, 706, doi: 10.1086/165766

Dirienzo, W. J., Brogan, C., Indebetouw, R., et al. 2015, AJ, 150, 159, doi: 10.1088/0004-6256/150/5/159

Dobbs, C. L., Krumholz, M. R., Ballesteros-Paredes, J., et al. 2014, in Protostars and Planets VI, Henrik Beuther, Ralf S. Klessen, Cornelis P. Dullemond, and Thomas Henning (eds.), University of Arizona Press, Tucson, 914 pp., p.3-26, 3

Draine, B. T. 2011, Physics of the Interstellar and Intergalactic Medium

Draine, B. T., & Li, A. 2007, ApJ, 657, 810, doi: 10.1086/511055

Dunham, M. M., Chen, X., Arce, H. G., et al. 2011, ApJ, 742, 1, doi: 10.1088/0004-637X/742/1/1

Egan, M. P., Shipman, R. F., Price, S. D., et al. 1998, ApJ, 494, L199, doi: 10.1086/311198

Elia, D., Molinari, S., Fukui, Y., et al. 2013, ApJ, 772, 45, doi: 10.1088/0004-637X/772/1/45

Elmegreen, B. G. 2012, in The Spectral Energy Distribution of Galaxies, Proceedings of the International Astronomical Union, IAU Symposium, Volume 284, p. 317-329, Vol. 284, 317–329

Evans, Neal J., I., Heiderman, A., & Vutisalchavakul, N. 2014, ApJ, 782, 114, doi: 10.1088/0004-637X/782/2/114

Evans, Neal J., I., Dunham, M. M., Jørgensen, J. K., et al. 2009, The Astrophysical Journal Supplement Series, 181, 321, doi: 10.1088/0067-0049/181/2/321

Evans, II, N. J., Rawlings, J. M. C., Shirley, Y. L., & Mundy, L. G. 2001, ApJ, 557, 193, doi: 10.1086/321639

Feng, S., Beuther, H., Zhang, Q., et al. 2016, A&A, 592, A21, doi: 10.1051/0004-6361/201526864

Fiege, J. D., & Pudritz, R. E. 2000, MNRAS, 311, 85, doi: 10.1046/j.1365-8711.2000.03066.x

Field, G. B., Goldsmith, D. W., & Habing, H. J. 1969, ApJ, 155, L149, doi: 10.1086/180324

Forbrich, J., Öberg, K., Lada, C. J., et al. 2014, ArXiv e-prints. https://arxiv.org/abs/1406.0540

Foster, J. B., Rosolowsky, E. W., Kauffmann, J., et al. 2009, ApJ, 696, 298, doi: 10.1088/0004-637X/696/1/298

Frau, P., Girart, J. M., Zhang, Q., & Rao, R. 2014, A&A, 567, A116, doi: 10.1051/0004-6361/201423917

Friesen, R. K., Bourke, T. L., Di Francesco, J., Gutermuth, R., & Myers, P. C. 2016, ArXiv e-prints. https://arxiv.org/abs/1610.10066

Friesen, R. K., Di Francesco, J., Shirley, Y. L., & Myers, P. C. 2009, ApJ, 697, 1457, doi: 10.1088/0004-637X/697/2/1457

Friesen, R. K., Pineda, J. E., co-PIs, et al. 2017, ApJ, 843, 63, doi: 10.3847/1538-4357/aa6d58

Gaia Collaboration, Brown, A. G. A., Vallenari, A., et al. 2018a, ArXiv e-prints, arXiv:1804.09365. https://arxiv.org/abs/1804.09365

Gaia Collaboration, Prusti, T., de Bruijne, J. H. J., et al. 2016, A&A, 595, A1, doi: 10.1051/0004-6361/201629272

Gaia Collaboration, Babusiaux, C., van Leeuwen, F., et al. 2018b, ArXiv e-prints, arXiv:1804.09378. https://arxiv.org/abs/1804.09378

Galli, P. A. B., Loinard, L., Ortiz-Léon, G. N., et al. 2018, ApJ, 859, 33, doi: 10.3847/1538-4357/aabf91

Garmany, C. D., Conti, P. S., & Chiosi, C. 1982, ApJ, 263, 777, doi: 10.1086/160548

Ginsburg, A., & Mirocha, J. 2011, PySpecKit: Python Spectroscopic Toolkit, Astrophysics Source Code Library. http://ascl.net/1109.001

Glover, S. C. O., & Clark, P. C. 2012, MNRAS, 421, 9, doi: 10.1111/j.1365-2966.2011.19648.x

Goldsmith, P. F. 2001, ApJ, 557, 736, doi: 10.1086/322255

Goodman, A. A., Barranco, J. A., Wilner, D. J., & Heyer, M. H. 1998, ApJ, 504, 223, doi: 10.1086/306045

Goodman, A. A., Benson, P. J., Fuller, G. A., & Myers, P. C. 1993, ApJ, 406, 528, doi: 10.1086/172465

Griffin, M. J., Abergel, A., Abreu, A., et al. 2010, A&A, 518, L3, doi: 10.1051/0004-6361/201014519

Gritschneder, M., Heigl, S., & Burkert, A. 2017, ApJ, 834, 202, doi: 10.3847/1538-4357/834/2/202

Hacar, A., Alves, J., Burkert, A., & Goldsmith, P. 2016, A&A, 591, A104, doi: 10.1051/0004-6361/201527319

Hacar, A., & Tafalla, M. 2011, A&A, 533, A34, doi: 10.1051/0004-6361/201117039

Hacar, A., Tafalla, M., Forbrich, J., et al. 2018, ArXiv e-prints. https://arxiv.org/abs/1801.01500

Hacar, A., Tafalla, M., Kauffmann, J., & Kovács, A. 2013, A&A, 554, A55, doi: 10.1051/0004-6361/201220090

Haffner, L. M., Reynolds, R. J., Tufte, S. L., et al. 2003, The Astrophysical Journal Supplement Series, 149, 405, doi: 10.1086/378850

Hatchell, J., Fuller, G. A., Richer, J. S., Harries, T. J., & Ladd, E. F. 2007, A&A, 468, 1009, doi: 10.1051/0004-6361:20066466

Henshaw, J. D., Caselli, P., Fontani, F., Jiménez-Serra, I., & Tan, J. C. 2014, MNRAS, 440, 2860, doi: 10.1093/mnras/stu446

Henshaw, J. D., Caselli, P., Fontani, F., et al. 2013, MNRAS, 428, 3425, doi: 10.1093/mnras/sts282

—. 2016a, MNRAS, 463, 146, doi: 10.1093/mnras/stw1794

Henshaw, J. D., Longmore, S. N., Kruijssen, J. M. D., et al. 2016b, MNRAS, 457, 2675, doi: 10.1093/mnras/stw121

Henshaw, J. D., Jiménez-Serra, I., Longmore, S. N., et al. 2017, MNRAS, 464, L31, doi: 10.1093/mnrasl/slw154

Herbst, E., & Klemperer, W. 1973, ApJ, 185, 505, doi: 10.1086/152436

Hernandez, A. K., & Tan, J. C. 2011, ApJ, 730, 44, doi: 10.1088/0004-637X/730/1/44

—. 2015, ApJ, 809, 154, doi: 10.1088/0004-637X/809/2/154

Hernandez, A. K., Tan, J. C., Caselli, P., et al. 2011, ApJ, 738, 11, doi: 10.1088/0004-637X/738/1/11

Hernandez, A. K., Tan, J. C., Kainulainen, J., et al. 2012, ApJ, 756, L13, doi: 10.1088/2041-8205/756/1/L13

Hildebrand, R. H. 1983, QJRAS, 24, 267

Ho, P. T. P., & Townes, C. H. 1983, ARA&A, 21, 239, doi: 10.1146/annurev.aa.21.090183.001323

Hoare, M. G., Kurtz, S. E., Lizano, S., Keto, E., & Hofner, P. 2007, in Protostars and Planets V, 181

Högbom, J. A. 1974, Astronomy and Astrophysics Supplement Series, 15, 417

Houde, M., Bastien, P., Peng, R., Phillips, T. G., & Yoshida, H. 2000a, ApJ, 536, 857, doi: 10.1086/308980

Houde, M., Peng, R., Phillips, T. G., Bastien, P., & Yoshida, H. 2000b, ApJ, 537, 245, doi: 10.1086/309035

Jackson, J. M., Rathborne, J. M., Shah, R. Y., et al. 2006, The Astrophysical Journal Supplement Series, 163, 145, doi: 10.1086/500091

Jijina, J., & Adams, F. C. 1996, ApJ, 462, 874, doi: 10.1086/177201

Jiménez-Serra, I., Caselli, P., Fontani, F., et al. 2014, MNRAS, 439, 1996, doi: 10.1093/mnras/stu078

Jiménez-Serra, I., Caselli, P., Tan, J. C., et al. 2010, MNRAS, 406, 187, doi: 10.1111/j.1365-2966.2010.16698.x

Jordi, C., Gebran, M., Carrasco, J. M., et al. 2010, A&A, 523, A48, doi: 10.1051/0004-6361/201015441

Kahn, F. D. 1974, A&A, 37, 149

Kainulainen, J., Alves, J., Beuther, H., Henning, T., & Schuller, F. 2011, A&A, 536, A48, doi: 10.1051/0004-6361/201117757

Kainulainen, J., & Tan, J. C. 2013, A&A, 549, A53, doi: 10.1051/0004-6361/201219526

Kauffmann, J., Bertoldi, F., Bourke, T. L., Evans, II, N. J., & Lee, C. W. 2008, A&A, 487, 993, doi: 10.1051/0004-6361:200809481

Kauffmann, J., & Pillai, T. 2010, ApJ, 723, L7, doi: 10.1088/2041-8205/723/1/L7

Kelly, B. C., Shetty, R., Stutz, A. M., et al. 2012, ApJ, 752, 55, doi: 10.1088/0004-637X/752/1/55

Kennicutt, Robert C., J. 1989, ApJ, 344, 685, doi: 10.1086/167834

—. 1998, ApJ, 498, 541, doi: 10.1086/305588

Kennicutt, Robert C., J., Calzetti, D., Walter, F., et al. 2007, ApJ, 671, 333, doi: 10.1086/522300

Keto, E. 2003, ApJ, 599, 1196, doi: 10.1086/379545

Kirk, H., Myers, P. C., Bourke, T. L., et al. 2013, ApJ, 766, doi: 10.1088/0004-637X/766/2/115

Kolmogorov, A. 1941, Akademiia Nauk SSSR Doklady, 30, 301

Kong, S., Tan, J. C., Arce, H. G., et al. 2018, ApJ, 855, L25, doi: 10.3847/2041-8213/aab151

Kong, S., Tan, J. C., Caselli, P., et al. 2017a, ApJ, 834, 193, doi: 10.3847/1538-4357/834/2/193

—. 2017b, ArXiv e-prints. https://arxiv.org/abs/1701.05953

Kounkel, M., Covey, K., Suarez, G., et al. 2018, ArXiv e-prints, arXiv:1805.04649. https://arxiv.org/abs/1805.04649

Kroupa, P. 2001, MNRAS, 322, 231, doi: 10.1046/j.1365-8711.2001.04022.x

Krumholz, M. R. 2012, ApJ, 759, 9, doi: 10.1088/0004-637X/759/1/9

Krumholz, M. R., Klein, R. I., & McKee, C. F. 2005, in Massive Star Birth: A Crossroads of Astrophysics, Vol. 227, 231–236

Kurtz, S., Cesaroni, R., Churchwell, E., Hofner, P., & Walmsley, C. M. 2000, in Protostars and Planets IV, 299–326

Lada, C. J. 1987, in IAU Symposium, Vol. 115, Star Forming Regions, ed. M. Peimbert & J. Jugaku, 1–17

Lada, C. J., Forbrich, J., Lombardi, M., & Alves, J. F. 2012, ApJ, 745, 190, doi: 10.1088/0004-637X/745/2/190

Lada, C. J., Lombardi, M., & Alves, J. F. 2010, ApJ, 724, 687, doi: 10.1088/0004-637X/724/1/687

Lancaster, P., & Salkauskas, K. 1981, Mathematics of Computation, 37, 141, doi: 10.2307/2007507

Larson, R. B. 1969, MNRAS, 145, 271, doi: 10.1093/mnras/145.3.271

—. 1981, MNRAS, 194, 809, doi: 10.1093/mnras/194.4.809

Leroy, A. K., Walter, F., Brinks, E., et al. 2008, AJ, 136, 2782, doi: 10.1088/0004-6256/136/6/2782

Levenberg, K. 1944, Quarterly Journal of Applied Mathmatics, II, 164

Levin, D. 1998, Math. Comput., 67, 1517, doi: 10.1090/S0025-5718-98-00974-0

Li, H.-B., Yuen, K. H., Otto, F., et al. 2015, Nature, 520, 518, doi: 10.1038/nature14291

Lim, W., Carey, S. J., & Tan, J. C. 2015, ApJ, 814, 28, doi: 10.1088/0004-637X/814/1/28

Lim, W., & Tan, J. C. 2014, ApJ, 780, L29, doi: 10.1088/2041-8205/780/2/L29

Lim, W., Tan, J. C., Kainulainen, J., Ma, B., & Butler, M. J. 2016, ApJ, 829, L19, doi: 10.3847/2041-8205/829/1/L19

Liu, H. B., Galván-Madrid, R., Jiménez-Serra, I., et al. 2015, ApJ, 804, 37, doi: 10.1088/0004-637X/804/1/37

Liu, H. B., Jiménez-Serra, I., Ho, P. T. P., et al. 2012a, ApJ, 756, 10, doi: 10.1088/0004-637X/756/1/10

Liu, H. B., Quintana-Lacaci, G., Wang, K., et al. 2012b, ApJ, 745, 61, doi: 10.1088/0004-637X/745/1/61

Liu, T., Li, P. S., Juvela, M., et al. 2018, ArXiv e-prints. https://arxiv.org/abs/1803.09457

Lombardi, M., Bouy, H., Alves, J., & Lada, C. J. 2014, A&A, 566, A45, doi: 10.1051/0004-6361/201323293

Longmore, S. N., Bally, J., Testi, L., et al. 2013, MNRAS, 429, 987, doi: 10.1093/mnras/sts376

Lu, X., Zhang, Q., Liu, H. B., Wang, J., & Gu, Q. 2014, ApJ, 790, 84, doi: 10.1088/0004-637X/790/2/84

Mac Low, M.-M., Klessen, R. S., Burkert, A., & Smith, M. D. 1998, Phys. Rev. Lett., 80, 2754, doi: 10.1103/PhysRevLett.80.2754

Mangum, J. G., & Shirley, Y. L. 2015, PASP, 127, 266, doi: 10.1086/680323

Marquardt, D. W. 1963, Journal of the Society for Industrial and Applied Mathematics, 11, 431, doi: 10.1137/0111030

Masters, J., Garwood, B., Langston, G., & Shelton, A. 2011, in Astronomical Society of the Pacific Conference Series, Vol. 442, Astronomical Data Analysis Software and Systems XX, ed. I. N. Evans, A. Accomazzi, D. J. Mink, & A. H. Rots, 127

Masunaga, H., & Inutsuka, S.-i. 2000, ApJ, 531, 350, doi: 10.1086/308439

Mathis, J. S., Rumpl, W., & Nordsieck, K. H. 1977, ApJ, 217, 425, doi: 10.1086/155591

McKee, C. F., & Ostriker, E. C. 2007, ARA&A, 45, 565, doi: 10.1146/annurev.astro.45.051806.110602

McKee, C. F., & Ostriker, J. P. 1977, ApJ, 218, 148, doi: 10.1086/155667

McKee, C. F., & Tan, J. C. 2002, Nature, 416, 59, doi: 10.1038/416059a

—. 2003, ApJ, 585, 850, doi: 10.1086/346149

McMullin, J. P., Waters, B., Schiebel, D., Young, W., & Golap, K. 2007, in Astronomical Society of the Pacific Conference Series, Vol. 376, Astronomical Data Analysis Software and Systems XVI, ed. R. A. Shaw, F. Hill, & D. J. Bell, 127

Menten, K. M., Reid, M. J., Forbrich, J., & Brunthaler, A. 2007, A&A, 474, 515, doi: 10.1051/0004-6361:20078247

Moeckel, N., & Clarke, C. J. 2011, MNRAS, 410, 2799, doi: 10.1111/j.1365-2966.2010.17659.x

Molinari, S., Swinyard, B., Bally, J., et al. 2010, PASP, 122, 314, doi: 10.1086/651314

Molinari, S., Schisano, E., Elia, D., et al. 2016, A&A, 591, A149, doi: 10.1051/0004-6361/201526380

Motte, F., Bontemps, S., & Louvet, F. 2017, ArXiv e-prints. https://arxiv.org/abs/1706.00118

Myers, P. C. 1983, ApJ, 270, 105, doi: 10.1086/161101

Myers, P. C., & Benson, P. J. 1983, ApJ, 266, 309, doi: 10.1086/160780

Nakano, T., Hasegawa, T., & Norman, C. 1995, ApJ, 450, 183, doi: 10.1086/176130

Nguyen Luong, Q., Motte, F., Hennemann, M., et al. 2011, A&A, 535, A76, doi: 10.1051/0004-6361/201117831

Norris, R. P. 2011, in Sixth IEEE International Conference on eScience, 21–24

Oort, J. H., Kerr, F. J., & Westerhout, G. 1958, MNRAS, 118, 379, doi: 10.1093/mnras/118.4.379

Ortiz-León, G. N., Loinard, L., Kounkel, M. A., et al. 2017, ApJ, 834, 141, doi: 10.3847/1538-4357/834/2/141

Ostriker, J. 1964, ApJ, 140, 1056, doi: 10.1086/148005

Ott, M., Witzel, A., Quirrenbach, A., et al. 1994, A&A, 284, 331

Palla, F., & Stahler, S. W. 2002, The Astrophysical Journal, 581, 1194

Perault, M., Omont, A., Simon, G., et al. 1996, A&A, 315, L165

Peretto, N., & Fuller, G. A. 2009, A&A, 505, 405, doi: 10.1051/0004-6361/200912127

Peretto, N., Fuller, G. A., Duarte-Cabral, A., et al. 2013, A&A, 555, A112, doi: 10.1051/0004-6361/201321318

Pilbratt, G. L., Riedinger, J. R., Passvogel, T., et al. 2010, A&A, 518, L1, doi: 10.1051/0004-6361/201014759

Pillai, T., Kauffmann, J., Tan, J. C., et al. 2015, ApJ, 799, 74, doi: 10.1088/0004-637X/799/1/74

Pillai, T., Kauffmann, J., Wiesemeyer, H., & Menten, K. M. 2016, A&A, 591, A19, doi: 10.1051/0004-6361/201527803

Pillai, T., Wyrowski, F., Carey, S. J., & Menten, K. M. 2006, A&A, 450, 569, doi: 10.1051/0004-6361:20054128

Pineda, J. E., Goodman, A. A., Arce, H. G., et al. 2010a, ApJ, 712, L116, doi: 10.1088/2041-8205/712/1/L116

—. 2011a, ApJ, 739, L2, doi: 10.1088/2041-8205/739/1/L2

Pineda, J. E., Rosolowsky, E. W., & Goodman, A. A. 2009, ApJ, 699, L134, doi: 10.1088/0004-637X/699/2/L134

Pineda, J. E., Arce, H. G., Schnee, S., et al. 2011b, ApJ, 743, 201, doi: 10.1088/0004-637X/743/2/201

Pineda, J. E., Offner, S. S. R., Parker, R. J., et al. 2015, Nature, 518, 213, doi: 10.1038/nature14166

Pineda, J. L., Goldsmith, P. F., Chapman, N., et al. 2010b, ApJ, 721, 686, doi: 10.1088/0004-637X/721/1/686

Planck Collaboration, Abergel, A., Ade, P. A. R., et al. 2011, A&A, 536, A25, doi: 10.1051/0004-6361/201116483

Poglitsch, A., Waelkens, C., Geis, N., et al. 2010, A&A, 518, L2, doi: 10.1051/0004-6361/201014535

Punanova, A., Caselli, P., Pineda, J. E., et al. 2018, ArXiv e-prints, arXiv:1806.03354. https://arxiv.org/abs/1806.03354

Qiu, K., Zhang, Q., Menten, K. M., et al. 2014, ApJ, 794, L18, doi: 10.1088/2041-8205/794/1/L18

Ragan, S. E., Bergin, E. A., & Wilner, D. 2011, ApJ, 736, 163, doi: 10.1088/0004-637X/736/2/163

Ragan, S. E., Heitsch, F., Bergin, E. A., & Wilner, D. 2012, ApJ, 746, 174, doi: 10.1088/0004-637X/746/2/174

Rathborne, J. M., Jackson, J. M., & Simon, R. 2006, ApJ, 641, 389, doi: 10.1086/500423

Rathborne, J. M., Lada, C. J., Muench, A. A., Alves, J. F., & Lombardi, M. 2008, The Astrophysical Journal Supplement Series, 174, 396, doi: 10.1086/522889

Roberts, M. S. 1957, Publications of the Astronomical Society of the Pacific, 69, 59, doi: 10.1086/127013

Robitaille, T. P., & Whitney, B. A. 2010, ApJ, 710, L11, doi: 10.1088/2041-8205/710/1/L11

Rosolowsky, E. W., Pineda, J. E., Foster, J. B., et al. 2008a, ApJS, 175, 509, doi: 10.1086/524299

Rosolowsky, E. W., Pineda, J. E., Kauffmann, J., & Goodman, A. A. 2008b, ApJ, 679, 1338, doi: 10.1086/587685

Rybicki, G. B., & Lightman, A. P. 1979, Radiative processes in astrophysics

Sánchez-Monge, Á., Palau, A., Fontani, F., et al. 2013, MNRAS, 432, 3288, doi: 10.1093/mnras/stt679

Sanhueza, P., Jackson, J. M., Foster, J. B., et al. 2012, ApJ, 756, 60, doi: 10.1088/0004-637X/756/1/60

Santos, F. P., Busquet, G., Franco, G. A. P., Girart, J. M., & Zhang, Q. 2016, ApJ, 832, 186, doi: 10.3847/0004-637X/832/2/186

Schaefer, S., McPhail, T., & Warren, J. 2006, ACM Trans. Graph., 25, 533, doi: 10.1145/1141911.1141920

Schmidt, M. 1959, ApJ, 129, 243, doi: 10.1086/146614

Schneider, N., Csengeri, T., Klessen, R. S., et al. 2015, A&A, 578, A29, doi: 10.1051/0004-6361/201424375

Scott, D. W. 1992, Multivariate density estimation: theory, practice, and visualization (New York; Chichester: John Wiley & Sons)

Shepherd, D. S., & Churchwell, E. 1996, ApJ, 472, 225, doi: 10.1086/178057

Shirley, Y. L. 2015, PASP, 127, 299, doi: 10.1086/680342

Shu, F. H., Adams, F. C., & Lizano, S. 1987, Annual Review of Astronomy and Astrophysics, 25, 23, doi: 10.1146/annurev.aa.25.090187.000323

Simon, R., Jackson, J. M., Rathborne, J. M., & Chambers, E. T. 2006a, ApJ, 639, 227, doi: 10.1086/499342

Simon, R., Rathborne, J. M., Shah, R. Y., Jackson, J. M., & Chambers, E. T. 2006b, ApJ, 653, 1325, doi: 10.1086/508915

Sokolov, V., Wang, K., Pineda, J. E., et al. 2017, A&A, 606, A133, doi: 10.1051/0004-6361/201630350

—. 2018, A&A, 611, L3, doi: 10.1051/0004-6361/201832746

Solomon, P. M., Rivolo, A. R., Barrett, J., & Yahil, A. 1987, ApJ, 319, 730, doi: 10.1086/165493

Spezzano, S., Caselli, P., Bizzocchi, L., Giuliano, B. M., & Lattanzi, V. 2017, A&A, 606, A82, doi: 10.1051/0004-6361/201731262

Spitzer, Lyman, J. 1968, Dynamics of Interstellar Matter and the Formation of Stars, 1

Stahler, S. W., & Palla, F. 2005, The Formation of Stars, 865

Stutz, A., Launhardt, R., Linz, H., et al. 2010, A&A, 518, L87, doi: 10.1051/0004-6361/201014537

Suzuki, H., Yamamoto, S., Ohishi, M., et al. 1992, ApJ, 392, 551, doi: 10.1086/171456

Swift, J. J., Welch, W. J., & Di Francesco, J. 2005, ApJ, 620, 823, doi: 10.1086/427257

Tafalla, M., & Hacar, A. 2015, A&A, 574, A104, doi: 10.1051/0004-6361/201424576

Tafalla, M., Myers, P. C., Caselli, P., & Walmsley, C. M. 2004, A&A, 416, 191, doi: 10.1051/0004-6361:20031704

Tafalla, M., Myers, P. C., Caselli, P., Walmsley, C. M., & Comito, C. 2002, ApJ, 569, 815, doi: 10.1086/339321

Tan, J. C. 2017, ArXiv e-prints. https://arxiv.org/abs/1710.11607

Tan, J. C., Beltrán, M. T., Caselli, P., et al. 2014, Protostars and Planets VI, 149, doi: 10.2458/azu_uapress_9780816531240-ch007

Tan, J. C., Kong, S., Butler, M. J., Caselli, P., & Fontani, F. 2013, ApJ, 779, 96, doi: 10.1088/0004-637X/779/2/96

Tatematsu, K., Ohashi, S., Sanhueza, P., et al. 2016, Publications of the Astronomical Society of Japan, 68, doi: 10.1093/pasj/psw002

Traficante, A., Calzoletti, L., Veneziani, M., et al. 2011, MNRAS, 416, 2932, doi: 10.1111/j.1365-2966.2011.19244.x

van Dishoeck, E. F., & Black, J. H. 1986, The Astrophysical Journal Supplement Series, 62, 109, doi: 10.1086/191135

Walmsley, C. M., & Ungerechts, H. 1983, A&A, 122, 164

Wang, K., Testi, L., Burkert, A., et al. 2016, ApJS, 226, 9, doi: 10.3847/0067-0049/226/1/9

Wang, K., Testi, L., Ginsburg, A., et al. 2015, MNRAS, 450, 4043, doi: 10.1093/mnras/stv735

Wang, K., Zhang, Q., Wu, Y., Li, H.-b., & Zhang, H. 2012, ApJ, 745, L30, doi: 10.1088/2041-8205/745/2/L30

Wang, K., Zhang, Q., Wu, Y., & Zhang, H. 2011, ApJ, 735, 64, doi: 10.1088/0004-637X/735/1/64

Wang, K., Zhang, Q., Testi, L., et al. 2014, MNRAS, 439, 3275, doi: 10.1093/mnras/stu127

White, R. L., Accomazzi, A., Berriman, G. B., et al. 2009, in astro2010: The Astronomy and Astrophysics Decadal Survey, Vol. 2010, P64

Williams, G. M., Peretto, N., Avison, A., Duarte-Cabral, A., & Fuller, G. A. 2018, ArXiv e-prints. https://arxiv.org/abs/1801.07253

Williams, J. P., Blitz, L., & McKee, C. F. 2000, in Protostars and Planets IV, 97

Wolfire, M. G., & Cassinelli, J. P. 1987, ApJ, 319, 850, doi: 10.1086/165503

Wood, D. O. S., & Churchwell, E. 1989, ApJ, 340, 265, doi: 10.1086/167390

Wyrowski, F., Güsten, R., Menten, K. M., et al. 2016, A&A, 585, A149, doi: 10.1051/0004-6361/201526361

Yorke, H. W., & Sonnhalter, C. 2002, ApJ, 569, 846, doi: 10.1086/339264

Zhang, Q., Wang, K., Lu, X., & Jiménez-Serra, I. 2015, ApJ, 804, 141, doi: 10.1088/0004-637X/804/2/141

Zhang, Q., Qiu, K., Girart, J. M., et al. 2014, ApJ, 792, 116, doi: 10.1088/0004-637X/792/2/116

Acknowledgements

First and foremost, I can't thank enough my supervisors, Paola Caselli, Jaime Pineda, and Ke Wang, for excellent supervision, giving me plenty of freedom to explore the topics I was interested in yet still reining me in in time to catch up with the project management timescales. My colleagues in the CAS group have also helped me be a great deal with all those friendly yet not necessarily work-related discussions, ping-pong matches, and bar outings that served as a constant reminder that there is indeed life after PhD. I would also like to take a moment to proudly confer a joint Outstanding Officemate award onto Ana, Anna, and Birgitta — you've managed to make office life fun! To this date my biggest relief of grad school is still finding out that I haven't flooded the institute over a particularly rainy weekend after all (well pranked!).

To my family, who, despite jokingly implying that I was destined for humanities, have exerted a gentle influence over me that formed my inquisitive view of the world, and can be ultimately held responsible me trying out science for real. I am also extremely grateful to all my friends and teachers in Natural Science Lyceum No. 145 in Kyiv, a place that somehow managed to preserve and cultivate an idea that science is fun. I would not be here if not for the curiosity that was sparked and, subsequently, firmly lodged in my brain over many stimulating lectures, competitions, and conversations held in those high-school years. I also want to give a shout-out to all the friends I've made in Taiwan, the six years spent there sharpened my curiosity about the world fueled many trips elsewhere.

Some of the best times I've had in Munich were with the student community in Garching and the USM. Thanks for all the parties, board game and role-playing nights, trips, BBQs, and shindigs you relentlessly invited me to! Another great escape from work was provided weekly by Hiking Buddies Munich, although I still found myself explaining the topic of this thesis to many a curious hiker.

A special thank you goes to Graham Chapman, John Cleese, Terry Gilliam, Eric Idle, Terry Jones, and Michael Palin, who never failed to remind me to keep looking on the bright side of life.

I am heavily indebted to the whole astronomy open-source community for putting a titanic amount of work into making my favorite tools available. This work would not have been possible without an army of unpaid volunteers driven by passion for open-source development. I can only help that my own small contribution matters in the long run.

Last and unquestionably not least, I am immensely grateful to Linda, for the uninterrupted stream of cheerful optimism during the writing of this thesis.